

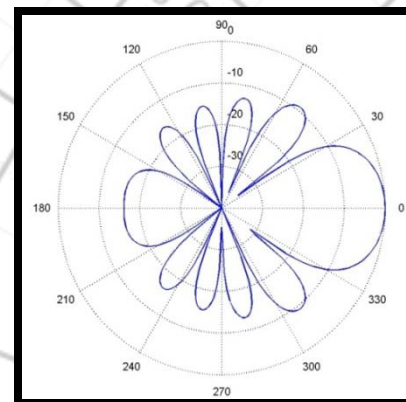
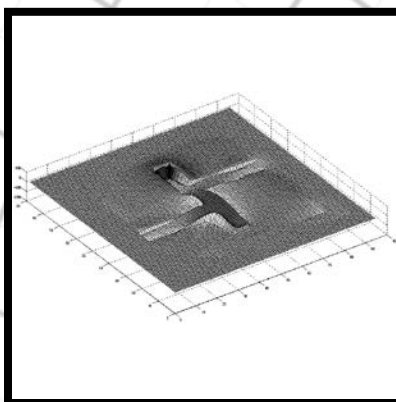
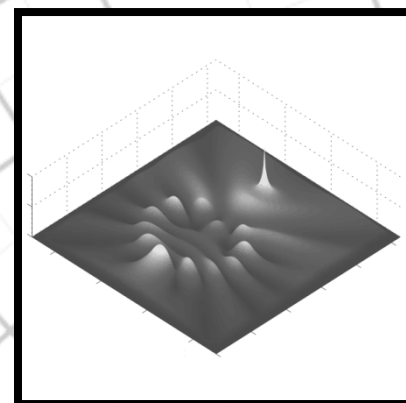
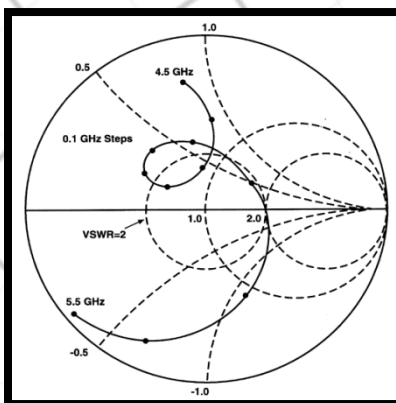
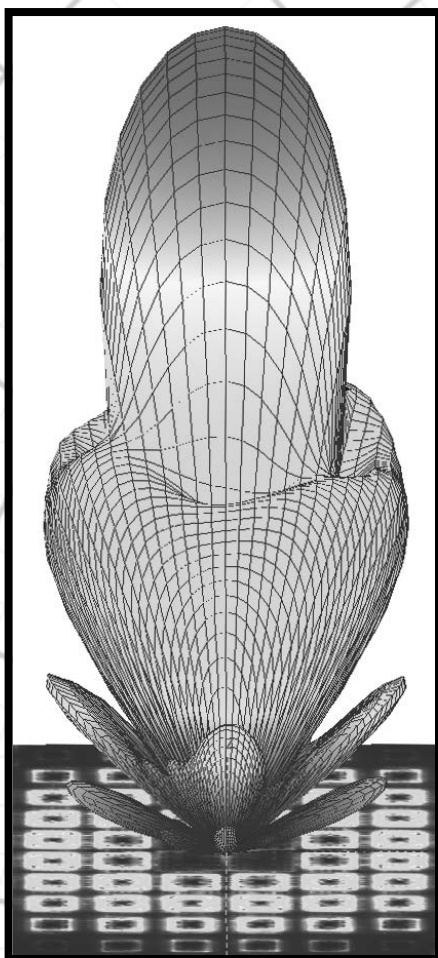
Applied Computational Electromagnetics Society

Journal



Cr t k n 2014

Vol. 29 No. 6



ISSN 1054-4887

GENERAL PURPOSE AND SCOPE: The Applied Computational Electromagnetics Society (*ACES*) Journal hereinafter known as the *ACES Journal* is devoted to the exchange of information in computational electromagnetics, to the advancement of the state-of-the art, and the promotion of related technical activities. The primary objective of the information exchange is to inform the scientific community on the developments of new computational electromagnetics tools and their use in electrical engineering, physics, or related areas. The technical activities promoted by this publication include code validation, performance analysis, and input/output standardization; code or technique optimization and error minimization; innovations in solution technique or in data input/output; identification of new applications for electromagnetics modeling codes and techniques; integration of computational electromagnetics techniques with new computer architectures; and correlation of computational parameters with physical mechanisms.

SUBMISSIONS: The *ACES Journal* welcomes original, previously unpublished papers, relating to applied computational electromagnetics. Typical papers will represent the computational electromagnetics aspects of research in electrical engineering, physics, or related disciplines. However, papers which represent research in applied computational electromagnetics itself are equally acceptable.

Manuscripts are to be submitted through the upload system of *ACES* web site <http://aces.ee.olemiss.edu> See "Information for Authors" on inside of back cover and at *ACES* web site. For additional information contact the Editor-in-Chief:

Dr. Atef Elsherbeni
Department of Electrical Engineering
The University of Mississippi
University, MS 386377 USA
Phone: 662-915-5382
Email: atef@olemiss.edu

SUBSCRIPTIONS: All members of the Applied Computational Electromagnetics Society are entitled to access and download the *ACES Journal* any published journal article available at <http://aces.ee.olemiss.edu>. Printed issues of the *ACES Journal* are delivered to institutional members. Each author of published papers receives a printed issue of the *ACES Journal* in which the paper is published.

Back issues, when available, are \$50 each. Subscription to *ACES* is through the web site. Orders for back issues of the *ACES Journal* and change of address requests should be sent directly to *ACES* office at:

Department of Electrical Engineering
The University of Mississippi
University, MS 386377 USA
Phone: 662-915-7231
Email: aglisson@olemiss.edu

Allow four weeks advance notice for change of address. Claims for missing issues will not be honored because of insufficient notice, or address change, or loss in the mail unless the *ACES* office is notified within 60 days for USA and Canadian subscribers, or 90 days for subscribers in other countries, from the last day of the month of publication. For information regarding reprints of individual papers or other materials, see "Information for Authors".

LIABILITY. Neither *ACES*, nor the *ACES Journal* editors, are responsible for any consequence of misinformation or claims, express or implied, in any published material in an *ACES Journal* issue. This also applies to advertising, for which only camera-ready copies are accepted. Authors are responsible for information contained in their papers. If any material submitted for publication includes material which has already been published elsewhere, it is the author's responsibility to obtain written permission to reproduce such material.

APPLIED COMPUTATIONAL ELECTROMAGNETICS SOCIETY JOURNAL

Crtkn2012
Vol. 27 No. 6
ISSN 1054-4887

The ACES Journal is abstracted in INSPEC, in Engineering Index, DTIC, Science Citation Index Expanded, the Research Alert, and to Current Contents/Engineering, Computing & Technology.

The illustrations on the front cover have been obtained from the research groups at the Department of Electrical Engineering, The University of Mississippi.

THE APPLIED COMPUTATIONAL ELECTROMAGNETICS SOCIETY

<http://aces.ee.olemiss.edu>

EDITOR-IN-CHIEF

Atef Elsherbeni

University of Mississippi, EE Dept.
University, MS 38677, USA

ASSOCIATE EDITORS-IN-CHIEF

Sami Barmada

University of Pisa, EE Dept.
Pisa, Italy, 56126

Fan Yang

University of Mississippi, EE Dept.
University, MS 38677, USA

Mohamed Bakr

McMaster University, ECE Dept.
Hamilton, ON, L8S 4K1, Canada

Yasushi Kanai

Niigata Inst. of Technology
Kashiwazaki, Japan

Mohammed Hadi

Kuwait University, EE Dept.
Safat, Kuwait

Mohamed Abouzahra

MIT Lincoln Laboratory
Lexington, MA, USA

EDITORIAL ASSISTANTS

Matthew J. Inman

University of Mississippi, EE Dept.
University, MS 38677, USA

Anne Graham

University of Mississippi, EE Dept.
University, MS 38677, USA

EMERITUS EDITORS-IN-CHIEF

Duncan C. Baker

EE Dept. U. of Pretoria
0002 Pretoria, South Africa

Allen Glisson

University of Mississippi, EE Dept.
University, MS 38677, USA

David E. Stein

USAF Scientific Advisory Board
Washington, DC 20330, USA

Robert M. Bevensee

Box 812
Alamo, CA 94507-0516, USA

Ahmed Kishk

University of Mississippi, EE Dept.
University, MS 38677, USA

EMERITUS ASSOCIATE EDITORS-IN-CHIEF

Alexander Yakovlev

University of Mississippi, EE Dept.
University, MS 38677, USA

Erdem Topsakal

Mississippi State University, EE Dept.
Mississippi State, MS 39762, USA

EMERITUS EDITORIAL ASSISTANTS

Khaled ElMaghoub

University of Mississippi, EE Dept.
University, MS 38677, USA

Mohamed Al Sharkawy

Arab Academy for Science and
Technology, ECE Dept.
Alexandria, Egypt

Christina Bonnington

University of Mississippi, EE Dept.
University, MS 38677, USA

APRIL 2012 REVIEWERS

**Ahmed Abdelrahman
Licenciado Ruth Alvarez
Marco Arjona
Abdul Ali Babar
Mohamed Bakr
Sami Barmada
Robert Burkholder
Deb Chatterjee
Jorge Costa
Satya Dubey
Jieran Fang
Teixeira Fernando
Fernando Las-Heras
Naftali Herscovici
Park Hyun Ho
Yasushi Kanai
Nikolaos Kantartzis
Haider Khaleel
Said El-Khamy
Ashraf Islam
Ricardo Matias
Zahera Mekkioui**

**B. Moore
Ivor Morrow
Antonino Musolino
Arash Nejadpak
William Palmer
Tao Peng
Qinjiang Rao
Harvey Schuman
Apirat Siritaratiwat
Hossein Torkaman
Christopher Trueman
Yasuhiro Tsunemitsu
Chao-Fu Wang
Rui Wang
Xiaobo Wang
Wei-Chung Weng
Alexander Yakovlev
Su Yan
Fan Yang
Wenjian Yu
Amir Zaghloul**

THE APPLIED COMPUTATIONAL ELECTROMAGNETICS SOCIETY
JOURNAL

Vol. 27 No. 4

April 2012

TABLE OF CONTENTS

“Breast Cancer Detection Using Support Vector Machine Technique Applied on Extracted Electromagnetic Waves” M. A. Sharkawy, M. Sharkas, and D. Ragab.....	292
“A Dynamic Measurement Method for Determining the Output Impedance of an RF Power Amplifier” V. P. McGinn and V. Demir.....	302
“Optimization of Reception Antenna Composed with Unbalanced Fed Inverted L Element for Digital Terrestrial Television” D. Yagyu and M. Taguchi.....	311
“Optimum Design of SIW Longitudinal Slot Array Antennas with Specified Radiation Patterns” S. E. Hosseininejad, N. Komjani, H. Oraizim, and M. T. Noghani.....	320
“Application of ANNs in Evaluation of Microwave Pyramidal Absorber Performance” M. Agatonovic, Z. Marinkovic, and V. Markovic.....	326
“Design of High Performance Dual Frequency Concentric Split Ring Square Element for Broadband Reflectarray Antenna” S. H. Yusop, N. Misran, M. T. Islam, and M. Y. Ismail.....	334
“A Switchable UWB Slot Antenna using SIS-HSIR and SIS-SIR for Multi-Mode Wireless Communications Applications” Y. Li, W. Li, and W. Yu.....	340
“A CPW Dual Band Notched UWB Antenna” M. Mighani, M. Akbari, and N. Felegari.....	352
“Scattering from Large-Scale Stratified Rough Surfaces using Improved BMIA/CAG” L. He, L. Lang, Q. Li, and W. Zheng.....	360
“Impact of Composite Materials on the Shielding Effectiveness of Enclosures” W. Abdelli, X. Mininger, L. Pichon, and H. Trabelsi.....	369

Breast Cancer Detection Using Support Vector Machine Technique Applied on Extracted Electromagnetic Waves

M. Al Sharkawy, M. Sharkas, and D. Ragab

Department of Electronics and Communications Engineering
Arab Academy for Science, Technology, and Maritime Transport (AASTMT), Alexandria, Egypt
msharkawy@aast.edu, msharkas@aast.edu, and dina.ragab@gmail.com

Abstract— Breast cancer is one of the most common kinds of cancer, as well as the leading cause of decease among women. Early detection and diagnosis of breast cancer increases the chances for successful treatment and complete recovery for the patient. Mammography is currently the most sensitive method to detect early breast cancer; however, the magnetic resonance imaging (MRI) is the most attractive alternative to mammogram. Manual readings of mammograms may result in misdiagnosis due to human errors caused by visual fatigue. Computer aided detection systems (CAD) serve as a second opinion for radiologists. A new CAD system for the detection of breast cancer in mammograms is proposed. The discrete wavelet transform (DWT), the contourlet transform, and the principal component analysis (PCA) are all used for feature extraction; while the support vector machine (SVM) is used for classification. The system classifies normal and abnormal tissues in addition to benign and malignant tumors. A further investigation was implemented using electromagnetic waves instead of the classical MRI approach. A breast model was generated and near field data of electromagnetic waves were extracted to detect the abnormalities in the breast, especially the masses.

Index Terms— Contourlet transform, discrete wavelet transform, electromagnetic waves, principal component analysis, and support vector machine.

I. INTRODUCTION

For years, cancer has been one of the biggest threats to human life; it is expected to become the leading cause of death over the next few decades. Breast cancer is one of the most common kinds of cancer, as well as the leading cause of decease among women. In Egypt, breast cancer is the most common cancer among women, representing 18.9% of total cancer cases (35.1% in women and 2.2% in men) [1].

Mammography is currently the most sensitive method to detect early breast cancer; however, the magnetic resonance imaging (MRI) is the most attractive alternative to mammogram. Moreover, electromagnetic radiation attracted many researches as a viable alternative to both mammography and MRI.

Micro-calcifications (MCs) and masses are two important early signs of the disease as shown in Fig. 1. There are other less important signs such as architectural distortion [2]. Manual readings of mammograms may result in misdiagnosis due to human errors caused by visual fatigue. Computer aided detection systems (CAD) serve as a second opinion for radiologists. The main goal of the CAD system is to indicate the abnormalities with great accuracy and reliability.

A number of techniques for detection of the abnormalities have been developed in the past decades. Bhangale et al. [3] used the Gabor filters. Strickland et al. [4] introduced the undecimated wavelet transform by combining sub-bands from multiple transforms.

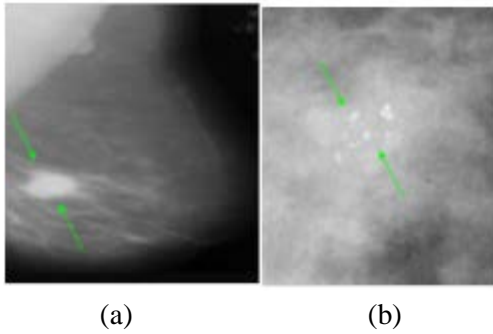


Fig. 1. Examples of mammograms (a) mass area and (b) MCs area [2].

Wang and Karayiannis [5] used the wavelet based sub-band image decomposition. Bruce and Adhami [6] used the DWT modulus maxima method to extract multi-resolutional features that quantify the mass shapes. Yoshida et al. [7] combined a decimated wavelet transform and supervised learning. El-Toukhy et al. [8] introduced the curvelet transform. Gunawan [9] presented a new method for the detection of abnormalities using wavelet transform based on statistical methods; the detection rate was 96%. Juarez et al. [10] applied the functions db2, db4, db8, and db16 of the Daubechies wavelets family, the abnormalities were detected up to 80% accuracy. Balakumaran et al. [11] used the dyadic wavelet transform, and introduced the fuzzy shell clustering algorithm in order to mark the MCs region. Lizcano et al. [12] used the contourlet transform for feature extraction and the support vector machine (SVM) for classification. Addison et al. [13] used the principal component analysis (PCA) as a feature extraction technique to determine the breast cancer. Rejani and Selvi [14] used the SVM for classification; the sensitivity achieved was 88.75%. Sharkas et al. [15] used the proposed CAD system to detect the MCs and to classify between normal, abnormal tissues in addition to benign and malignant MC tumors and the achieved rate was almost 98 %.

The aim of this paper is to detect the abnormalities in the breast using CAD systems. A new CAD system is proposed in which the discrete wavelet transforms (DWT), the contourlet transform, and the PCA are used for feature extraction. Moreover, classifying between normal and abnormal tissues, in addition to benign and malignant lesions is presented using the SVM

technique. Furthermore, a breast model is generated using electromagnetic waves and near field data are extracted to detect the abnormalities, especially the masses. The proposed CAD system is applied on all the investigated samples.

The paper is organized as follows: Section II describes the CAD system and discusses the used system; Section III discusses the electromagnetic model; Section IV shows the computed results of the proposed technique; Section V discusses the results; and finally, Section VI concludes the presented work.

II. THE CAD SYSTEM

The steps of the proposed CAD system are illustrated in Fig. 2, which is described in details in the following sub-sections.

A. Image enhancement

In this step, the adaptive histogram equalization (AHE) is used, which is an image processing technique used to improve the contrast in images [16]. A generalization of AHE called contrast limited adaptive histogram equalization (CLAHE) was developed, where the histogram is calculated for the contextual region of the pixel [17].

B. Image segmentation

The region of interest (ROI) is extracted from the original mammogram image shown in Fig. 3.

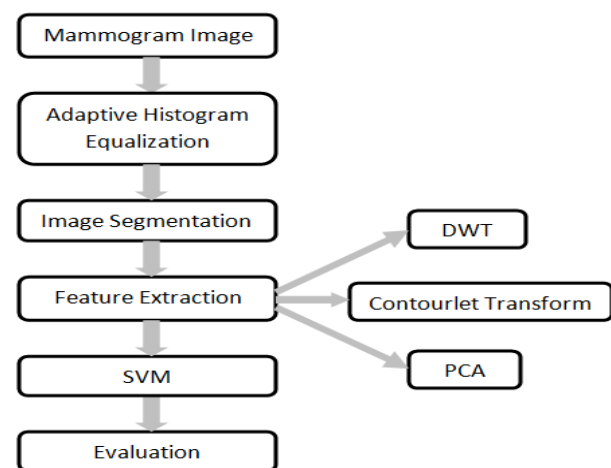


Fig. 2. Block diagram of the proposed CAD system.

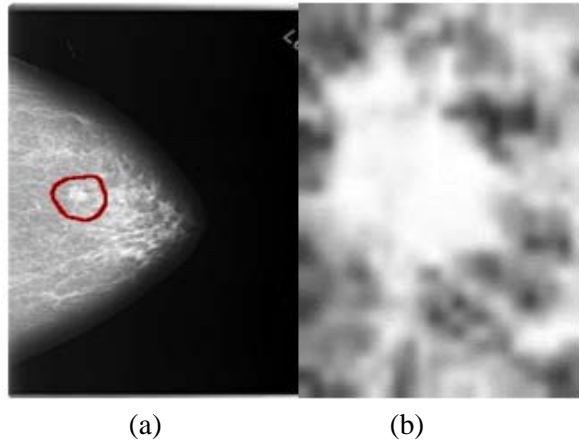


Fig. 3. Original mammogram image. (a) The red region is the mass area and (b) is the extracted enhanced ROI [18].

C. Feature extraction

There are many techniques for the feature extraction step; in this paper, the DWT, the contourlet transform, and the PCA are introduced to detect the masses.

1. The discrete wavelet transform

DWT technique is discussed by many researchers in [2,10,19,20].

2. The contourlet transform

The contourlet transform or pyramidal directional filter bank (PDFB) is a combination of a Laplacian pyramidal and a directional filter bank (DFB) [21]. Band pass images from the Laplacian pyramid [22] are fed into a DFB so that directional information can be captured. The low frequency component is separated from the directional components. After decimation, the decomposition can be iterated with the same DFB in the low pass band to form a pyramid structure. The contourlet transform provides a multi-scale directional decomposition [23].

Do and Vetterli [24] proposed a PDFB in order to implement the contourlet transform, which is a discrete version of the curvelet transform. The proposed structure is a combination of the Laplacian pyramid and the DFB. Their pyramidal DFB has united two advantages of the two structures, which are multi-resolution and multi-direction. It attempts to separate the low frequency component from the

rest directional components and reiterates with the same DFB in the low pass band, forming a pyramid structure. On the other hand, the decomposition solves the problem at low frequency; however, it is still not maximally decimated.

3. Principal component analysis

Principal component analysis (PCA) is a method that reduces data dimensionality by performing a covariance analysis between factors; it reduces the number of observed variables to a smaller number of principal components, which account for most of the variance of the observed variables. It is used when variables are highly correlated, and it is suitable for data sets in multiple dimensions [25].

PCA belongs to linear transforms based on the statistical techniques. It provides a powerful tool for data analysis and pattern recognition, which is often used in signal and image processing [25].

PCA technique can be summarized in the following steps:

1. Generate the data.
2. Subtract the mean from each of the data dimensions.
3. Calculate the covariance matrix.
4. Calculate the eigenvectors and the eigenvalues of the covariance matrix.
5. Choose the components and form a feature vector.
6. Generate the new data set.

D. Classification

In this step, the ROI is classified as either malignant or benign. There are lots of classifiers techniques; among them linear discriminant analysis (LDA), artificial neural network (ANN), binary decision tree, and support vector machine (SVM) [2].

In this paper, SVM is used; this is due to the fact that it achieved higher classification rates. SVM is a learning tool originated in modern statistical learning theory [26].

The aim of SVM is to devise a computationally efficient way of learning, separating hyper planes in a high dimensional feature space [26]. There are two cases for SVM; linear SVM and non-linear SVM [27]. The linear

SVM is only used here. This is due to the fact that the investigated data presented in this work is based on a two-dimensional feature space. Thus accepted results were achieved using a non-complex linear SVM technique. For future investigation, a non-linear SVM will be considered.

1. Linear SVM

There are many hyper planes that could classify two sets of data as shown in Fig. 4. The optimum hyper plane that one should choose is the one with the maximum margin. The margin is defined as the width by which the boundary could increase before hitting a data point. The support vectors as shown in Fig. 4 are considered the data points that the margin pushes up (i.e., borderline training sets). Thus, the goal of the SVM is to find the optimum hyper plane that separates clusters of target vectors on the opposing sides of the plane.

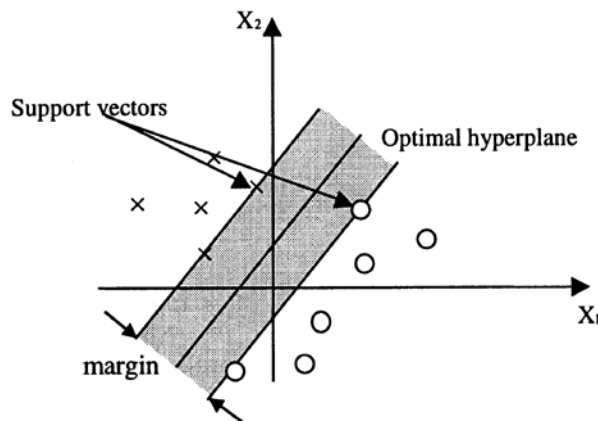


Fig. 4. SVM classification including a hyper plane that maximizes the separating margin between two classes [27].

The SVM formulation is based on the principle of structural risk minimization. It attempts to minimize a bound on the generalization error. Such error is generated from the learning machine on the test data not during the training process. This is instead of minimizing an objective function based on the training samples, such as the mean square error. The SVM is considered robust to work with when dealing with data outside the training set.

III. THE ELECTROMAGNETIC MODEL

The most common instruments used to detect the breast cancer are mammography and MRI. There are many differences between the two instruments. A MRI uses magnets that emit radio waves to produce a three-dimensional view of the breast and the underlying structures and vessels. Mammography uses low doses of radiation (x-rays) to produce a one-dimensional image of the breast. The breast MRI is a more sensitive test than mammography, especially when given with a contrast medium (i.e., a special dye). The dye makes the cancerous area of the breast appear much brighter, but it may cause many areas of the breast that do not have cancer to appear abnormal, causing an increased number of false positive test results. The breast MRI cannot visualize calcifications. On the other hand, mammography can visualize calcium deposits accurately. The breast MRI may be able to visualize dense breast tissues compared with mammography.

Meanwhile, mammograms and MRI systems do not use ionizing radiation. This leads electromagnetic radiation to become a viable alternative to both mammography and MRI. The microwave (MW) imaging systems offer a promising result in the biomedical applications [28, 29].

The goal of MW imaging is to detect, localize, and characterize the hidden tumors in the breast using electromagnetic waves at microwave frequencies [30, 31]. The MW has low power emission, thus it is harmless. It provides high contrast; this is due to its electrical properties. It also produces a three-dimensional view of the breast. The generated model shown in Fig. 5 is similar to an MRI scan shown in Fig. 6. For implementing the idea and testing the concept an incident plane wave is used to excite the model.

IV. RESULTS

To verify the proposed method, experiments were performed on the digital database for screening mammography (DDSM) mammogram database [18] using MATLAB. The DDSM database consists of 2620 cases available in 43 volumes. The volumes could be normal, benign, or malignant samples. In this database, the resolution of a mammogram is $50\mu\text{m}/\text{pixel}$ and the gray level depths are 12 bits and 16 bits.

Two hundred and sixty cases were extracted (100 normal cases, 80 benign mass tumors, and 80 malignant mass tumors). First, the samples are enhanced and segmented, and then features are extracted using three ways: DWT shown in Fig. 7, the contourlet transform shown in Fig. 8, and PCA data. The samples go through the SVM technique with linear kernel function for classification.

When classifying normal and mass tissues, the highest classification rate was for the vertical component of the 1st level DWT, which was 93.33%. The approximate component for the 2nd level DWT, achieved 96.67% classification rate as shown in Fig. 9. This proved to be the highest rate when compared to the vertical, horizontal, and diagonal components.

When distinguishing between benign and malignant mass tumors, the contourlet transform features achieved the highest classification rate 92% as shown in Fig. 10.

Tables 1 and 2 illustrate the different rates for the different components of the 1st and 2nd levels DWT in order to distinguish between normal and mass tissues, and benign and malignant tumors, respectively.

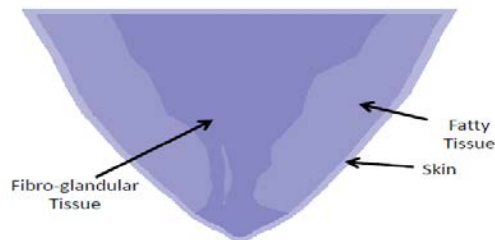


Fig. 5. The generated breast model.

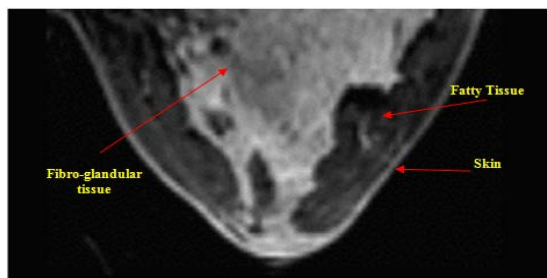
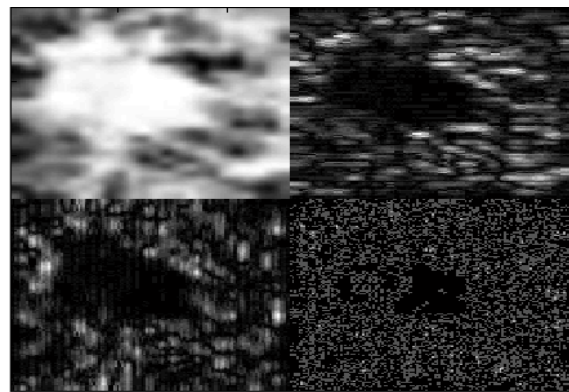


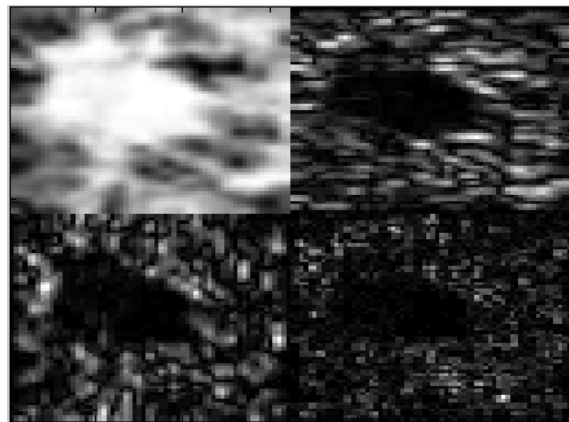
Fig. 6. An MRI scan of a normal breast [32].



(a)



(b)



(c)

Fig. 7. Extracted features using DWT, (a) original image, (b) 1st level DWT, and (c) 2nd level DWT.

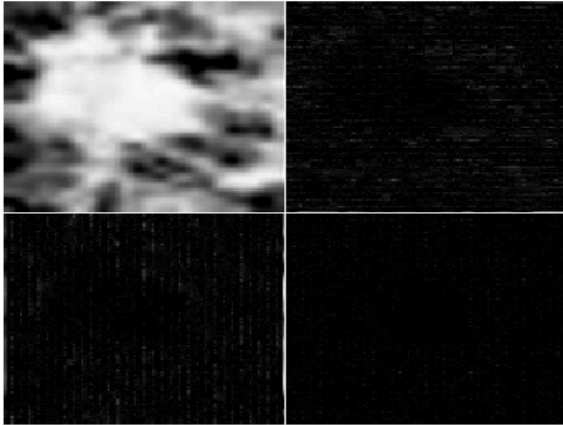


Fig. 8. The contourlet transform coefficients for the malignant mass sample shown in Fig. 7 (a).

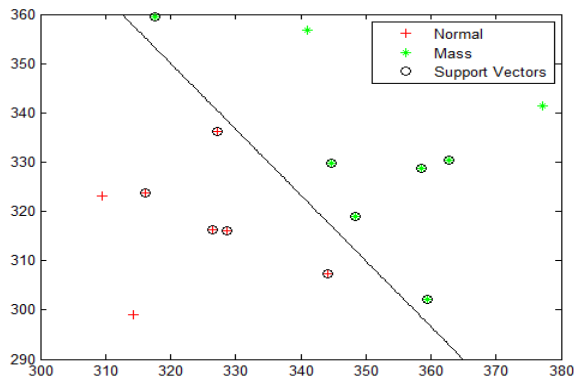


Fig. 9. SVM classification between normal and mass tissues for the approximate component of the 2nd level DWT features.

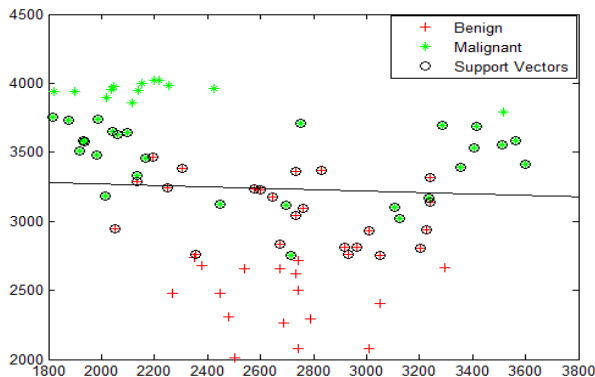


Fig. 10. SVM classification between benign and malignant mass tumors for significant contourlet coefficients features.

Table 1: Classification rates for 1st and 2nd levels DWT to classify between normal and mass tissues

	1 st level DWT	2 nd level DWT
Approximate	83.33%	96.67%
Vertical	93.33%	83.33%
Horizontal	56.67%	50%
Diagonal	56.67%	53.33%

Table 2: Classification rates for 1st and 2nd levels DWT to distinguish between benign and malignant tumors

	1 st level DWT	2 nd level DWT
Approximate	81.25%	73.75%
Vertical	86.25%	66.25%
Horizontal	51.25%	51.25%
Diagonal	55%	50%

For validation purposes, the receiver operating characteristic (ROC) analysis curve is computed for the vertical component of the 1st level DWT features, which is shown in Fig. 11. The area under the curve equals to 0.917; this means the detection rate is 91.7 %, which is a recognized performance compared to other previous work. This computed value is close to the 86.25 % analytical value for the vertical component of the 1st level DWT. The DWT, contourlet, and PCA feature extraction techniques' results are discussed in Table 3.

An electromagnetic breast model is generated and simulated using Ansoft high frequency structure simulated (HFSSTM) software package [33] as shown in Fig. 12. Two-dimensional plane cuts were generated from the model to collect data and test it. A sample of near field data passing through the breast model with a detected tumor is shown in Fig. 13. As previously mentioned in Section III, plane wave excitation is considered for simplicity. It is also used to prove the idea of using electromagnetic waves in conjunction with different image processing techniques for practical detection of tumors as a robust alternative for MRI. Further investigation will be considered for implementing antenna arrays to enhance the tumor detection and provide further hidden information.

Sixty samples (30 benign and 30 malignant) were generated from the model. These samples go through the previous CAD system. The best classification rate was for the approximate and vertical components of the 1st level DWT features

and the contourlet transform features. Table 4 provides the rates for different components of the 1st and 2nd levels DWT. The results of the feature extraction techniques for the electromagnetic model samples are presented in Table 5.

Table 3: Classification rates for different feature extraction techniques to distinguish between normal and mass tissues, and benign and malignant tumors

	normal and mass tissues	benign and malignant tumors
DWT	96.67%	80.73%
Contourlet	52%	92%
PCA	60%	58.75%

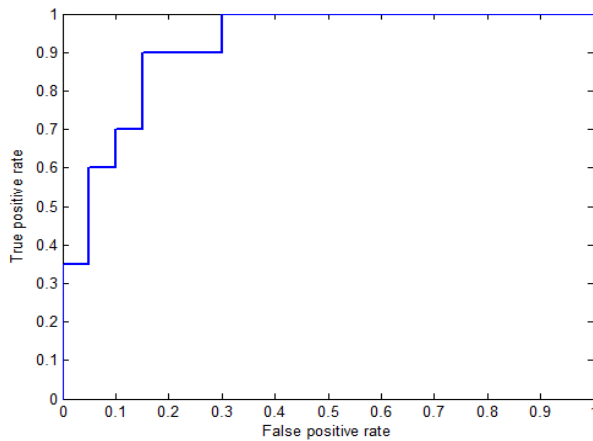


Fig. 11. Computed ROC curve for the vertical component of the 1st level DWT for benign and malignant samples.

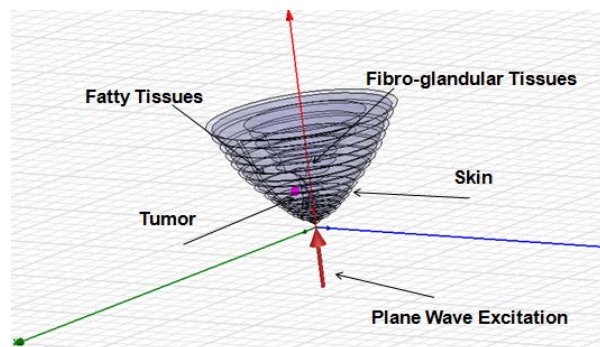
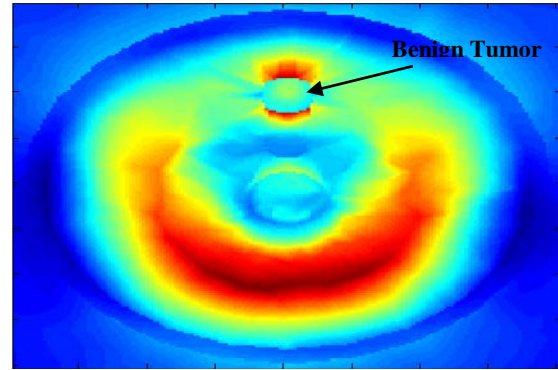
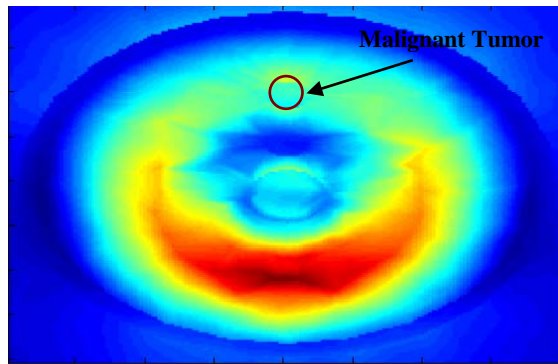


Fig. 12. Electromagnetic breast model using HFSSTM.



(a)



(b)

Fig. 13. Near field plane cuts at the middle of (a) benign and (b) malignant tumors.

Table 4: Classification rates for 1st and 2nd levels DWT to classify between benign and malignant mass tumors for the electromagnetic samples

	1 st level DWT	2 nd level DWT
Approximate	99.9 %	85.71%
Vertical	99.9 %	92.86%
Horizontal	50%	64.29%
Diagonal	64.29%	50%

Table 5: Classification rates for different feature extraction techniques for the electromagnetic samples

	Benign and malignant tumors
DWT	99.9 %
Contourlet	99.9 %
PCA	57.14%

V. DISCUSSIONS

For the DDSM samples, the best classification rate achieved when distinguishing between normal and mass tissues was for the DWT features, namely the vertical component of the 1st

level DWT and the approximate component of the 2nd level DWT as shown in Tables 1 and 2. The PCA and the contourlet transform features did not provide promising results, however, the performance of the PCA features proved to be better. Whereas, when distinguishing between benign and malignant mass tumors; the best classification rate was for the contourlet transform features. The DWT features come in the second rank, while the PCA features yielded only 58.75%. This is clear in Table 3.

A benign tumor of radius 4 mm and ϵ_r equals to 66 is placed near the fibroglandular tissues. One can easily notice from the electric field distribution shown in Fig. 13 (a) that the tumor is obviously detected due to its high dielectric constant relative to the neighboring tissues. A malignant tumor of ϵ_r equals to 20 is detected inside the breast model as shown from the near field data presented in Fig. 13 (b). The tumor in this case is not visible enough; this is due to the fact that its dielectric constant is close to the surrounding tissues.

The classification results of the electromagnetic breast model, shown in Tables 4 and 5, reveal that both the DWT and the contourlet transform have the best classification rate. However, the PCA achieved a weak classification rate. It is clear from the data in Table 5 that the lesions were completely classified (i.e., 99.9 %). This is because the generated samples from the electromagnetic model are not a real extracted data relative to the DDSM database. They were extracted from the proposed HFSSTM model.

VI. CONCLUSIONS

The goal of this work is to detect the masses and classify the tissues in the breast using SVM technique. A new CAD system is introduced, where the DWT, the contourlet transform, and the PCA are used in the feature extraction step. An electromagnetic breast model was generated and tested using the SVM technique and the proposed feature extraction methods and then compared to the DDSM results.

The proposed technique and methods achieved a high classification rates using the DWT and the contourlet transform features. The usage of electromagnetic waves is considered a robust alternative to the MRI for cancer detection. This

CAD system can be applied to detect cancer and classify it in any human organ.

ACKNOWLEDGMENT

Great appreciation to Dr. Magda El-Shenawee and her group at The University of Arkansas.

REFERENCES

- [1] S. Omar, H. Khaled, R. Gaafar, A. R. Zekry, S. Eissa, and O. El-Khatib, "Breast Cancer in Egypt: A Review of Disease Presentation and Detection Strategies," *La Revue de Santé de la Méditerranéorientale*, vol. 9, no. 3, 2003.
- [2] J. Bozek, M. Mustra, K. Delac, and M. Grgic, "A Survey of Image Processing Algorithms in Digital Mammography," *Rec. Advan. In Mult. Sig. Process. And Commun.*, SCI 231, pp. 631-657, 2009.
- [3] T. Bhangale, U. B. Desai, and U. Shama, "An Unsupervised Scheme for Detection of Microcalcifications on Mammograms," *IEEE Image Processing proceedings International Conference*, vol. 1, 2000.
- [4] R. N. Strickland and H. I. Hahn, "Wavelet Transforms for Detecting Microcalcifications in Mammogram," *IEEE Trans. Med. Imaging*, vol. 15, no. 2, pp. 218-229, April 1996.
- [5] T. C. Wang and N. B. Karayiannis, "Detection of Microcalcifications in Digital Mammograms using Wavelets," *IEEE Trans. Med. Imaging*, vol. 17 no. 4, pp. 498-509, August 1998.
- [6] L. M. Bruce and R. R. Adhami, "Classifying Mammographic Mass Shapes using the Wavelet Transform Modulus-Maxima Method," *IEEE Trans. Med. Imaging*, vol. 18, pp. 1170-1177, 1999.
- [7] H. Yoshida, K. Doi, and M. Nishikawa, "Automated Detection of Clustered Microcalcifications in Digital Mammograms using Wavelet Transform Techniques," *Medical Imaging Bellingham Proc. SPIE 2167*, 1994.
- [9] D. Gunawan, "Microcalcification Detection using Wavelet Transform," *IEEE Communications, Computers and signal Processing Conference*, 2001.
- [10] L. C. Juarez, J. V. Ponomaryov, and R. L. Sanchez, "Detection of Microcalcifications in Digital Mammograms Images using Wavelet Transform," *IEEE Proceedings of the Electronics, Robotics and Automotive Mechanics Conference*, 2006.
- [11] T. Balakumaran, I. Vennila, and C. G. Shankar, "Detection of Microcalcification in Mammograms using Wavelet Transform and Fuzzy Shell Clustering," *International Journal*

- of *Computer Science and Information Security (IJCSIS)*, vol. 7, no. 1, 2010.
- [12] J. A. M. Lizcano, C. S. Avila, and L. M. Perez, "A Microcalcification Detection System for Digital Mammography using the Contourlet Transform," *Proceeding of the International conference on Computational and Experimental Engineering and Science, Portugal*, July 2004.
- [13] J. F. D. Addison, S. Wermter, and G. Z. Arevian, "A Comparison of Feature Extraction and Selection Techniques," *Proc. Int'l Conf. on Artificial Neural Networks 2003, Istanbul, Turkey*, pp. 212-215, June 2003.
- [14] Y. I. A. Rejani and S. T. Selvi, "Early Detection of Breast Cancer using SVM Classifier Technique," *International Journal on Computer Science and Engineering*, vol. 1, no. 3, 2009.
- [15] M. Sharkas, M. Al Sharkawy, and D. Ragab, "Detection of Microcalcifications in Mammograms using Support Vector Machine," *IEEE European Modeling Symposium EMS2011, Madrid, Spain*, November 2011.
- [16] S. M. Pizer, et al. "Adaptive Histogram Equalization and its Variations," *Computer Vision, Graphics, and Image Processing*, vol. 39, 1987.
- [17] E. D. Pisano et al., "Contrast Limited Adaptive Histogram Equalization Image Processing to Improve the Detection of Simulated Spiculations in Dense Mammograms," *Digital Imaging*, vol. 11, no. 4, pp. 193-200, 1998.
- [18] Digital database for screening mammography (DDSM). Available online at: <http://marathon.csee.usf.edu/mammography/Database.html>.
- [19] H. Mirzaalian, M. R. Ahmadzadeh, S. Sadri, and M. Jafari, "Various Applying of Wavelet Transform in Digital Mammograms for Detecting Masses and Microcalcifications," *Conference on Machine Vision Applications*, Tokyo, Japan, May 2007.
- [20] T. Edwards, "Discrete Wavelet Transforms Theory and Implementation," *Stanford University*, September 1992. Available online at: <http://qss.stanford.edu/~godfrey/wavelets>
- [21] M. N. Do and M. Vetterli, "The Contourlet Transform: An Efficient Directional Multiresolution Image Representation," *IEEE Trans. Image processing*, vol. 14, no. 12, pp. 2091-2106, December 2005.
- [22] P. J. Burt and E. H. Adelson, "The Laplacian Pyramid as a Compact Image Code," *IEEE Trans. Communications*, vol. COM-31, no. 4, April 1983.
- [23] A. P. N. Vo, T. T. Nguyen, and S. Orintara, "Texture Image Retrieval using Complex Directional Filterbank," *IEEE Proceeding of the International Symposium Circuits and Systems, ISCAS 2006*.
- [24] M. N. Do and M. Vetterli, "Contourlets, in Beyond Wavelets," *G. V. Welland, Ed. Amsterdam, Netherlands: Academic*, chapter 4, pp. 83-105, 2003.
- [25] L. I. Smith, "A Tutorial on Principal Components Analysis," February 2002. Available online at: www.cs.otago.ac.nz/cosc453/student.../principal_components.pdf
- [26] S. R. Gunn, "Support Vector Machines for Classification and Regression," *Technical Report, Faculty of Engineering, Science and Mathematics, School of Electronics and Computer Science*, May 1998.
- [27] I. El-Naqa, Y. Yang, M. N. Wernick, N. P. Galatsanos, and R. M. Nishikawa, "A Support Vector Machine Approach for Detection of Microcalcifications," *IEEE Trans. Med. Imaging*, vol. 21, no. 12, December 2002.
- [28] G. Zhu, M. Popovic, "Enhancing Microwave Breast Tomography with Microwave Induced Thermoacoustic Imaging," *Applied Computational Electromagnetics Society (ACES) Journal*, vol. 24, no. 6, pp. 618-627, December 2009.
- [29] S. Iudicello, F. Bardati, "Functional Imaging of Compressed Breast by Microwave Radiometry," *Applied Computational Electromagnetics Society (ACES) Journal*, vol. 24, no. 1, pp. 64 - 71, February 2009.
- [30] D. A. Woten and M. El-Shenawee, "Quantitative Analysis of Breast Skin for Tumor Detection using Electromagnetic Waves," *Applied Computational Electromagnetics Society (ACES) Journal*, vol. 24, no. 5, pp. 458-463, October 2009.
- [31] H. Kanj and M. Popovic, "Two-Element T-Array for Cross-Polarized Breast Tumor Detection," *Applied Computational Electromagnetics Society (ACES) Journal*, vol. 23, no. 3, pp. 249-254, September 2008.
- [32] R. Weisskoff, "MRImages," Available online at: int.ch.liv.ac.uk
- [33] HFSSTM Software, Version 9, Ansoft Corporation.



Mohamed Al Sharkawy was born in Alexandria, Egypt, in 1978. He graduated from the Department of Electrical Engineering, Arab Academy for Science and Technology (AAST), Alexandria, Egypt, on June 2000, and received both, the M.Sc. and the Ph.D. degrees in Electrical Engineering from the University of Mississippi, USA, on October 2003, and December 2006, respectively. From 2002 to 2006, he worked as a research assistant then as a visiting scholar at the Department of Electrical Engineering at the University of Mississippi till June 2007. Currently, he is an Associate Professor at the Electronics and Communications Department at the AAST, where he is currently teaching graduate and undergraduate courses. His research interests include electromagnetic scattering from parallel chiral and metamaterial cylinders and the application of finite difference time and frequency domain techniques for the analysis and design of compact and ultra wideband antennas and microwave devices for wireless communications, radar applications, and breast cancer detection. He has more than 45 papers in international journals and proceedings of international and national symposia and one book by Morgan & Claypool.



Maha Sharkas obtained her B.Sc., M.Sc., and PhD in 1990, 1996 and 2002, respectively from the Electrical Engineering Department, Alexandria University. She is currently a Professor in the Electronics and Communications Department at the AAST. Her research interests are in the field of signal processing, image watermarking, biometrics, biomedical engineering, and pattern recognition.



Dina Ragab graduated from the Arab Academy for Science and Technology (AAST) Faculty of Engineering, Electronics and Communications Department in 2007. She got her Master's degree in Electrical Engineering in 2011. She is currently a Teacher Assistant at the AAST.

A Dynamic Measurement Method for Determining the Output Impedance of an RF Power Amplifier

Vincent P. McGinn and Veysel Demir

Department of Electrical Engineering
Northern Illinois University, DeKalb, IL 60115, USA
vmcginn@niu.edu, vdemir@niu.edu

Abstract — Described herein is a novel approach for measuring the output impedance of a radio frequency (RF) power amplifier under actual operating (dynamic) conditions. The procedure involves loading the amplifier with three different values of resistance which are close to the intended load resistance value. Three separate experiments yield load excitation voltages (or powers) which permit direct calculation of the source complex impedance. The precision of determining the source impedance of the amplifier under test is only limited by the known tolerance of load resistance values used and the accuracy of measurements taken. The most important attribute of the technique described is that no requirement exists to alter the operating frequency. Also, the technique is applicable at microwave frequencies.

Index Terms — Equivalent circuits, impedance measurement, power amplifiers, radio frequency amplifier.

I. INTRODUCTION

A need exists to determine the complex output impedance of an RF power amplifier. The excellent article by Abramovitz [1] gives possible amplifier topologies with predictions of input and output impedances but provides no guidance on experimentally measuring impedances. Other authors [2] describe impedance matching networks for optimizing power transfer and efficiency but do not directly measure the amplifier output impedance. Factually, this reference [2] notes significant discrepancies between simulation and laboratory measurements. Within the microwave bands load pull techniques can characterize

amplifier output impedances. Recent articles using slide screw tuners indirectly characterize amplifier output impedance via calculations from reflection coefficients [3]. This method is totally impractical at low frequencies. Such a situation exists for a power supply voltage regulator of the feedback amplifier design. Voltage regulation is a low frequency phenomenon and the output of the regulator may exhibit undesirably high impedance at high frequencies. Serrano-Finetti [4] has suggested varying the regulator load sinusoidally to characterize the system output impedance. This approach addresses only low frequency characteristics.

Classical discussions on amplifier output impedance focus on maximum power transfer [5-7] or suggest measurement methods confined to VHF and frequencies beyond [8]. The study which follows suggests a practical method for characterization of amplifier output impedance. Though experimental results are discussed at VHF, the proposed method is applicable at microwave frequencies as well. A detailed error analysis of the method is also provided.

II. DISCUSSION

Amplifiers may be of narrowband (resonant) or wideband design. A narrowband design will change output power as the operating frequency is altered necessitating “retuning.” By definition, however, a wideband design will not exhibit power output changes with respect to operating frequency changes. In either case, the following measurement procedures and calculations are applicable. Thus, the amplifier’s source impedance can be determined at one frequency or many

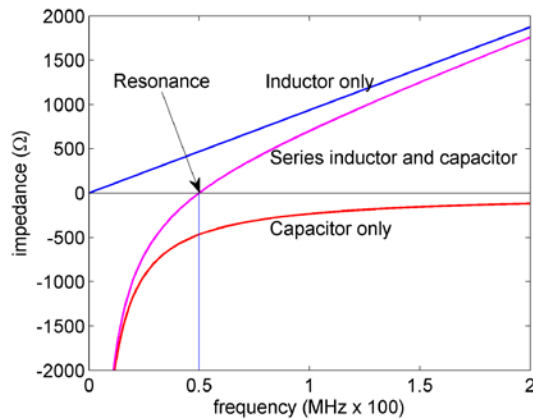


Fig. 1. Series LC reactance vs. frequency.

frequency points. Also, proper modeling allows the technique to be extended through microwave frequencies.

At any single operating frequency the output impedance of an amplifier may be modeled as a Thevenin equivalent circuit: An ideal voltage generator in electrical series with impedance (Z). [6, 9] This impedance, in general, can be complex: that is, $Z=R+jX$ where R is the real (in phase) or resistive component and X is the imaginary (quadrature) or reactive component. Measuring the voltage which appears across a resistor placed at the amplifier output reveals nothing with regard to the amplifier's impedance. However, noting the voltage across a single load does establish a baseline for all measurements to follow. Since Z is complex and possesses two parts (real and imaginary) a minimum of two more experiments (measurements) must be conducted to determine the magnitudes of R and X . For a stable amplifier R will always be positive. However, X may be either negative (capacitively reactive) or positive (inductively reactive). To mitigate the ambiguity of capacitive reactance and inductive reactance a modified version of the baseline measurement will be performed.

The imaginary part of the impedance may be a consequence of multiple reactances of the two different types (capacitive and inductive). Moreover, as system operating frequency is changed the magnitude of impedance may very well vary between peaks and troughs. Temes and LaPatra give an excellent discussion of possible one port impedance characteristics [10].

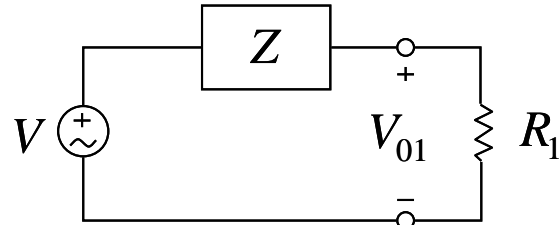


Fig. 2. Thevenin amplifier output model with attached load (R_1).

Irrespective of circuit sophistication, consider an operating amplifier delivering non-zero power to an arbitrary load at a single frequency. The output impedance of this amplifier may be modeled by one of the following: 1) a pure resistance, 2) a resistance in electrical series with an “equivalent” capacitive reactance, or 3) a resistance in electrical series with an “equivalent” inductive reactance. As a numerical illustration consider a 1.49 microHenry inductor in electrical series with a 6.8 picoFarad capacitor. Fig. 1 plots the reactance of the inductor by itself, the reactance of the series combination and the reactance of the capacitor by itself. A plot could also be developed for a parallel connection. However, for the plot presented note that resonance occurs at $f=50.0$ MHz. Below this frequency the LC combination is capacitively reactive and above this frequency it is inductively reactive. It is only at extreme frequency values (high and low) that the composite LC reactance curve is asymptotic to the individual components reactance curves. In the analysis which follows it is assumed that the system under investigation is linear and time invariant. Further, if the amplifier incorporates a form of automatic gain control (or output leveling) this must be disabled.

III. ANALYSIS

Refer to Fig. 2 which models the amplifier output as a Thevenin equivalent circuit (V in series with Z) with load R_1 connected. The voltage V_{01} is noted across R_1 . The load resistance is then changed to a new and different value (R_2). In a similar fashion the voltage drop across this new value of load resistance is noted (V_{02}). Proceeding to a load resistance different from the values of R_1 or R_2 a new load (R_3) is connected to the amplifier. Again, the voltage drop (V_{03}) is noted across R_3 . The ordering of resistance values for R_1 , R_2 and R_3 (low, medium and high) is unimportant. However,

best measurement accuracy is obtained by the widest possible spread of load resistance values. From a practical standpoint, properly designed amplifiers will easily withstand VSWR values of 2.0 or below. Thus, if the intended load is R_0 then other test loads selected might be on the order of $0.5 R_0$ and $2.0 R_0$. Some test configurations may utilize an instrument which measures power to a load resistance. Laboratory tests performed in the development of this paper used a BIRD model 43 in-line wattmeter. The instrument is useful up to frequencies of 2.3 GHz. At higher frequencies it is possible to develop precision loads monitored by a bolometer. This technique remains to be accomplished. Wideband load resistors used for this investigation were verified via a Hewlett Packard 8510C network analyzer.

In such cases where power to a load resistor is measured, the R.M.S. voltage across the load may be directly calculated by:

$$V_{01} = \sqrt{P_{01}R_1}, \quad V_{02} = \sqrt{P_{02}R_2}, \quad V_{03} = \sqrt{P_{03}R_3}.$$

Noting that $Z=R+jX$ we formulate the following:

$$V_{01} = \frac{VR_1}{\sqrt{(R+R_1)^2 + X^2}}, \quad (1)$$

$$\left(\frac{VR_1}{V_{01}}\right)^2 = (R+R_1)^2 + X^2. \quad (2a)$$

Similarly

$$\left(\frac{VR_2}{V_{02}}\right)^2 = (R+R_2)^2 + X^2, \quad (2b)$$

and

$$\left(\frac{VR_3}{V_{03}}\right)^2 = (R+R_3)^2 + X^2. \quad (2c)$$

The ratio of these equations is formulated:

$$K_1 = \left(\frac{R_1}{V_{01}}\right)^2 \left(\frac{V_{02}}{R_2}\right)^2 = \frac{(R+R_1)^2 + X^2}{(R+R_2)^2 + X^2}, \quad (3)$$

and

$$K_2 = \left(\frac{R_1}{V_{01}}\right)^2 \left(\frac{V_{03}}{R_3}\right)^2 = \frac{(R+R_1)^2 + X^2}{(R+R_3)^2 + X^2}. \quad (4)$$

Equations (3) and (4) may be combined to eliminate X :

$$\begin{aligned} &(K_1 - K_1K_2)(R+R_2)^2 \\ &+ (K_1K_2 - K_2)(R+R_3)^2 \\ &+ (K_2 - K_1)(R+R_1)^2 = 0. \end{aligned} \quad (5)$$

Let

$$(K_2 - K_1) = A, \quad (6)$$

$$(K_1 - K_1K_2) = B, \quad (7)$$

$$(K_1K_2 - K_2) = C. \quad (8)$$

Then,

$$A(R+R_1)^2 + B(R+R_2)^2 + C(R+R_3)^2 = 0, \quad (9)$$

or

$$\begin{aligned} &(A+B+C)R^2 + (2ARR_1 + 2BRR_2 + 2CRR_3) \\ &+ AR_1^2 + BR_2^2 + CR_3^2 = 0. \end{aligned}$$

Now, $A+B+C=0$, therefore,

$$R = \frac{-AR_1^2 - BR_2^2 - CR_3^2}{2(AR_1 + BR_2 + CR_3)}. \quad (10)$$

Before proceeding to calculate X it is prudent to determine if a reactive component of Z is present. A simple test to determine the presence of X is offered:

Formulate:

$$V_G = V_{01} \left(1 + \frac{R}{R_1}\right), \quad (11)$$

$$V_H = V_{02} \left(1 + \frac{R}{R_2}\right), \quad (12)$$

$$V_J = V_{03} \left(1 + \frac{R}{R_3}\right). \quad (13)$$

If $V_G=V_H=V_J$ no reactance is present and there exists no need to calculate X : $X=0$. When V_G , V_H and V_J are all equal this voltage is the Thevenin open circuit voltage. If, however, V_G , V_H and V_J all differ the calculation of X may be carried forth.

Now, since R is known refer back to either K_1 or K_2 to find X . Using K_1 :

$$K_1 = \frac{(R+R_1)^2 + X^2}{(R+R_2)^2 + X^2},$$

or

$$\frac{K_1(R+R_2)^2 - (R+R_1)^2}{(1-K_1)} = X^2, \quad (14)$$

and

$$\left[\frac{K_1 (R + R_2)^2 - (R + R_1)^2}{(1 - K_1)} \right]^{1/2} = X \quad (15)$$

This last equation gives the magnitude of X . Unfortunately, the sign of the reactance is unknown. The sign of the reactance can be determined by altering the operating frequency. However, the technique put forth promised impedance determination without changing the frequency of operation. This is still possible by adding a reactance in parallel with the test load resistance and observing output voltage effects with the presence or absence of the load reactance.

Either a capacitor or an inductor may be shunted to the load resistance to determine the sign of the source reactance. For example, if the source reactance is positive (inductive) a capacitor (which is not too large in value) shunted across the load resistance will cause the output voltage (and power) to increase. Alternately, if the source reactance is negative (capacitive) an inductor (which is not too small in value) shunted across the load resistance will cause the output voltage (and power) to rise.

If the source reactance is inductive, there is a value of load capacitance (C_{PEAK}) which will cause the load voltage to be a maximum. Similarly, for a capacitive source reactance there is a load inductance (L_{PEAK}) which will result in a maximum load voltage. For testing purposes it is suggested to select either a load capacitor which is smaller than this “peaking” value or an inductor which is larger than this peaking value. This representation avoids ambiguity. That is, if C were too large (or L too small) output voltage would actually decrease. The value of peaking load reactance (capacitive or inductive) may be calculated by treating the generator/load combination as a voltage divider, finding the first derivative of load voltage with respect to load reactance, and setting the derivative to zero. Recognizing that R is the source resistance and X is the source reactance the following occurs:

$$X_{LOAD} = \frac{R^2 + X^2}{X} \quad (16)$$

The load capacitance or inductance values shunted across the load resistance, which cause output voltage peaking, may be calculated directly:

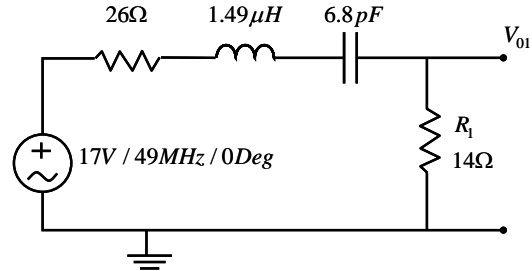


Fig. 3. Thevenin source with complex impedance loaded by resistance R_1 .

$$C_{PEAK} = \frac{X}{2\pi f (R^2 + X^2)} \quad (17)$$

$$L_{PEAK} = \frac{R^2 + X^2}{2\pi f X} \quad (18)$$

IV. DEMONSTRATION FOR COMPLEX SOURCE IMPEDANCE WITH BOTH REACTANCE TYPES

Referring to Fig. 3, the Thevenin source shows a voltage generator of 17 volts R.M.S., a resistance of 26.0 ohms in series with an LC series combination consisting of a 1.49 microHenry inductor and a 6.8 picoFarad capacitor. System operating frequency is set to 49.0 MHz. At this frequency we directly calculate the series reactance of the LC as $-j18.92$ ohms. This Thevenin equivalent circuit is intended to drive a 28.0 ohms load.

The source is respectively loaded with $R_1=14$ ohms, $R_2=28$ ohms, and $R_3=56$ ohms. The following results are recorded:

R (load)	Load Voltage (volts)
$R_1=14$ ohms	$V_{01}=5.38$
$R_2=28$ ohms	$V_{02}=8.32$
$R_3=56$ ohms	$V_{03}=11.3$

Using (3) and (4), one can obtain

$$K_1 = 0.597891129,$$

$$K_2 = 0.275722592.$$

Then, using (6)-(8)

$$A = -0.322168536,$$

$$B = 0.433039037,$$

$$C = -0.1108705.$$

Using (10), R becomes $R = 25.36737201 \Omega$, which checks within 2.433%. Next, one can

determine if reactance X is non-zero. Using (11), (12) and (13):

$$V_G = 15.128 \text{ volts,}$$

$$V_H = 15.865 \text{ volts,}$$

$$V_J = 16.419 \text{ volts.}$$

Since the values of V_G , V_H and V_J are different, we proceed to find the magnitude of X as

$$X = 19.5094182 \Omega,$$

which checks within 3.11%.

Finally, check sign of reactance: Test load reactances will be used to shunt the load resistance. The load resistance may be any value. Select $R_2=28$ ohms. Then, using (17) and (18),

$$C_{PEAK} = 61.87 \text{ pF,}$$

$$L_{PEAK} = 0.17 \mu\text{H.}$$

Recall, without any shunt reactance $V_{02}=8.32$ volts. On hand, convenient values of $C=27$ pF and $L=0.47$ μH are used for testing.

With C connected $V_{LOAD} \cong 7.96$ volts (decreased).

With L connected $V_{LOAD} \cong 8.54$ volts (increased).

The conclusion is that the generator reactance is capacitively reactive. Thus,

$$Z \cong R - jX = 25.367 - j19.509 \Omega.$$

It is interesting at this point to compare measured impedance magnitude versus actual impedance magnitude:

$$|Z|_{MEAS} = \sqrt{25.367^2 + 19.509^2} = 32.00 \Omega,$$

$$|Z|_{ACTUAL} = \sqrt{26^2 + 18.92^2} = 32.155 \Omega.$$

A complete error (sensitivity) analysis is provided in the following section.

V. ERROR ANALYSIS

A. Sensitivity analysis

The impedance of the Thevenin equivalent source of the test case is $Z_{ACTUAL} = 26 - j18.920532 \Omega$. The load voltages can be calculated for Z_{ACTUAL} , the measurement resistors of $R_1 = 14 \Omega$, $R_2 = 28 \Omega$, and $R_3 = 56 \Omega$, and the generator voltage of 17V as

$$V_{L1} = 5.378635 \text{ V,}$$

$$V_{L2} = 8.318949 \text{ V,}$$

$$V_{L3} = 11.312521 \text{ V.}$$

Comparing these analytically calculated voltages with the measured voltages, one can find the percentage errors in these measurements as

$$\frac{|V_{L1} - V_{01}|}{V_{L1}} \times 100 = 0.025370,$$

$$\frac{|V_{L2} - V_{02}|}{V_{L2}} \times 100 = 0.012623,$$

$$\frac{|V_{L3} - V_{03}|}{V_{L3}} \times 100 = 0.110683.$$

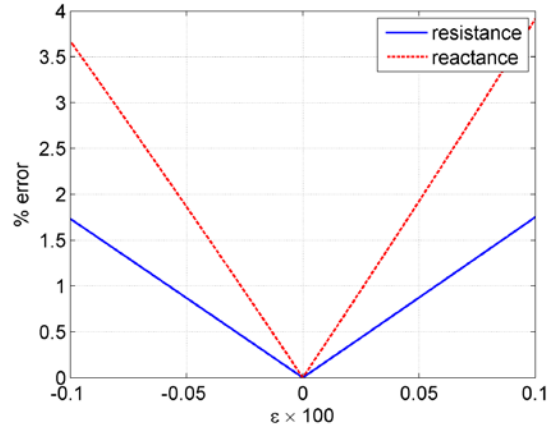


Fig. 4. Error in calculated output impedance when only V_{01} has error.

The resistance and reactance of the output impedance can be calculated using R_1 , R_2 , R_3 , V_{01} , V_{02} , and V_{03} , as described in Sections III and IV, more precisely as

$$R = 25.367373 \Omega,$$

$$X = 19.509418 \Omega.$$

Compared with the Z_{ACTUAL} , the percentage errors in the calculated values out of the measurements are

$$Error_R = \frac{|R_{ACTUAL} - R|}{R_{ACTUAL}} \times 100 = 2.4332,$$

$$Error_X = \frac{|X_{ACTUAL} - X_M|}{X_{ACTUAL}} \times 100 = 3.1124.$$

This analysis reveals that although the measurement errors in the voltages are very small, the errors in the calculated values of output resistance and reactance are comparatively very large. The calculated values are very sensitive to the measurement errors. Therefore, one should carefully assess the accuracy of the obtained results.

To further analyze the affect of measurement errors on the impedance calculations, the following analysis is performed. First, an error is introduced only to the measured voltage V_{01} such that

$$V_{01} = V_{L1} \times (1 + \varepsilon),$$

$$V_{02} = V_{L2},$$

$$V_{03} = V_{L3},$$

where ε is an error term. Then the errors $Error_R$ and $Error_X$ are calculated and plotted versus ε as shown in Fig. 4, which illustrates the extreme sensitivity of the calculations to measurement errors. Similar result can be obtained when error is introduced to only V_{02} or V_{03} .

When the same amount of error is introduced to all three measurements such that

$$V_{01} = V_{L1} \times (1 + \varepsilon),$$

$$V_{02} = V_{L2} \times (1 + \varepsilon),$$

$$V_{03} = V_{L3} \times (1 + \varepsilon),$$

it has been found that the errors, $Error_R$ and $Error_X$, effectively vanish. Therefore, if a measurement system introduces errors to the voltage measurements that are proportional to the measured voltages, then the calculated impedance values are reliable.

B. Optimum choice of measurement resistances

Section III describes a mathematical procedure to calculate unknown output resistance and reactance values of an amplifier through three measurements. Further, we will illustrate that; these values can be obtained through solution of a matrix equation.

Notice that (2) can be rewritten as

$$R_1^2 + 2R_1R + R^2 + X^2 - \frac{R_1^2}{V_{01}^2}V^2 = 0, \quad (19a)$$

$$R_2^2 + 2R_2R + R^2 + X^2 - \frac{R_2^2}{V_{02}^2}V^2 = 0, \quad (19b)$$

$$R_3^2 + 2R_3R + R^2 + X^2 - \frac{R_3^2}{V_{03}^2}V^2 = 0. \quad (19c)$$

One can subtract (19b) from (19a) and (19c) from (19b) and obtain the following equations

$$2(R_1 - R_2)R + \left(\frac{R_2^2}{V_{02}^2} - \frac{R_1^2}{V_{01}^2} \right) V^2 = R_2^2 - R_1^2, \quad (20a)$$

$$2(R_2 - R_3)R + \left(\frac{R_3^2}{V_{03}^2} - \frac{R_2^2}{V_{02}^2} \right) V^2 = R_3^2 - R_2^2. \quad (20b)$$

Equations (20a) and (20b) is a linear set of equations and can be put in the following matrix equation form

$$Ax = y, \quad (21)$$

where

$$A = \begin{bmatrix} \left(\frac{R_2^2}{V_{02}^2} - \frac{R_1^2}{V_{01}^2} \right) & 2(R_1 - R_2) \\ \left(\frac{R_3^2}{V_{03}^2} - \frac{R_2^2}{V_{02}^2} \right) & 2(R_2 - R_3) \end{bmatrix},$$

$$y = \begin{bmatrix} R_2^2 - R_1^2 & R_3^2 - R_2^2 \end{bmatrix}^T,$$

$$x = \begin{bmatrix} V^2 & R \end{bmatrix}^T.$$

Solution of $Ax = y$ yields R and V^2 , which then can be used to calculate X .

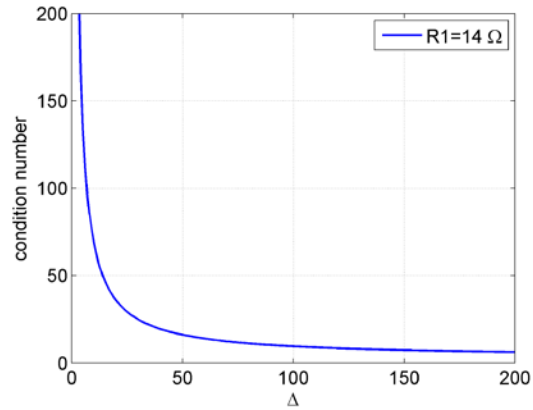


Fig. 5. Variation of condition number as a function of Δ .

A system of equations is considered to be well-conditioned if a small change in the coefficient matrix or a small change in the right hand side results in a small change in the solution vector, while a system of equations is considered to be ill-conditioned if a small change in the coefficient matrix or a small change in the right hand side results in a large change in the solution vector [11]. The condition number of the system described by the example given is calculated using the measurement data in the previous sections as

$Cond(A) = 50.35$. The condition number for a well-conditioned system should be close to unity. The calculated condition number verifies that the system is not well conditioned.

In the above calculation

$$Cond(A) = \|A\| \cdot \|A^{-1}\|,$$

where $\|A\|$ is the row sum norm (also called the uniform matrix norm) of matrix A . Thus,

$$\|A\| = 2(R_3 - R_2) + \left(\frac{R_3^2}{V_{03}^2} - \frac{R_2^2}{V_{02}^2} \right) \quad (22.a)$$

$$\|A^{-1}\| = \frac{2(R_3 - R_2) + 2(R_2 - R_1)}{2(R_2 - R_3) \left(\frac{R_2^2}{V_{02}^2} - \frac{R_1^2}{V_{01}^2} \right) - 2(R_1 - R_2) \left(\frac{R_3^2}{V_{03}^2} - \frac{R_2^2}{V_{02}^2} \right)} \quad (22.b)$$

To simplify the analysis, if we choose equal increments in the measurement resistances such that $(R_2 - R_3) = (R_1 - R_2)$, then the condition number becomes

$$Cond(A) = \frac{\left(4(R_3 - R_2) + 2 \left(\frac{R_3^2}{V_{03}^2} - \frac{R_2^2}{V_{02}^2} \right) \right)}{\left(\frac{R_3^2}{V_{03}^2} - \frac{R_2^2}{V_{02}^2} \right) - \left(\frac{R_2^2}{V_{02}^2} - \frac{R_1^2}{V_{01}^2} \right)} \quad (23)$$

In this equation, we can replace the measured voltages by the following using (1)

$$V_{01}^2 = V^2 \frac{R_1^2}{(R_1 + R)^2 + X^2},$$

$$V_{02}^2 = V^2 \frac{R^2}{(R_2 + R)^2 + X^2},$$

$$V_{03}^2 = V^2 \frac{R_3^2}{(R_3 + R)^2 + X^2},$$

to obtain the condition number in terms of source voltage and resistances as

$$Cond(A) = \frac{\left(4(R_3 - R_2)V^2 + 2 \left((R_3 + R)^2 - (R_2 + R)^2 \right) \right)}{\left((R_3 + R)^2 - (R_2 + R)^2 \right) - \left((R_2 + R)^2 - (R_1 + R)^2 \right)}.$$

If we write $R_2 = R_1 + \Delta$, $R_3 = R_1 + 2\Delta$, then after some manipulations we can simplify the condition number expression as

$$Cond(A) = \frac{\left(4V^2 + 2(2R_1 + 3\Delta + 2R) \right)}{2\Delta} \quad (24)$$

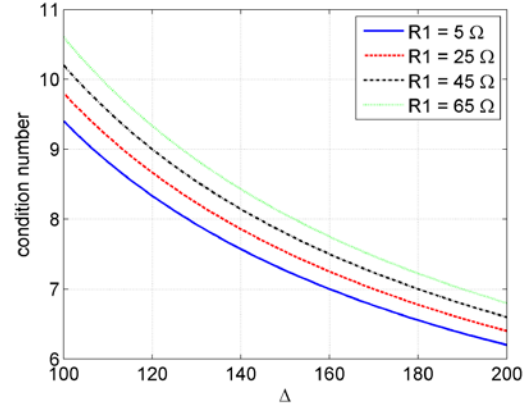


Fig. 6. Condition number vs. Δ for various values of R_1 .

This form of condition number expression allows us to analyze what values of resistances would be better to use in the measurements to obtain a system with a smaller condition number. This equation reveals that Δ needs to be large and R_1 needs to be small in order to achieve a well conditioned system. Figures 5 and 6 illustrate the variation of condition number with R_1 and Δ .

While choosing R_1 , R_2 , and R_3 , the main limiting factor would be the maximum allowable VSWR. If R and X can be estimated or are approximately known, they can be used to calculate maximum and minimum allowable measurement resistances. For a given VSWR

$$S = \frac{1 + |\Gamma|}{1 - |\Gamma|}, \quad (25)$$

where

$$\Gamma = \frac{R_M - R - jX}{R_M + R + jX}. \quad (26)$$

Here, R_M is the value of the measurement resistance to be determined for approximately known R and X values. Using (25) and (26), one can write

$$|\Gamma|^2 = G = \frac{(S-1)^2}{(S+1)^2} = \frac{(R_M - R)^2 + X^2}{(R_M + R)^2 + X^2}. \quad (27)$$

Rearranging terms, one can obtain a quadratic equation as

$$R_M^2 + \frac{-2R(1+G)}{(1-G)} R_M + (R^2 + X^2) = 0. \quad (28)$$

Solution of (28) for R_M leads to

$$R_M = R \frac{S^2 + 1}{2S} \pm \frac{1}{2} \sqrt{R^2 \left(S^2 - 2 + \frac{1}{S^2} \right) - 4X^2}, \quad (29)$$

which yields the minimum and maximum allowable values of measurement resistances, i.e. R_1 and R_3 , if $R_1 < R_2 < R_3$.

As a follow-up to the condition number analysis above, one can express (29) as $R_M = R_2 \pm \Delta$, where

$$R_2 = R \frac{S^2 + 1}{2S}, \quad (30)$$

$$\Delta = \sqrt{R^2 \left(S^2 - 2 + \frac{1}{S^2} \right) - 4X^2}, \quad (31)$$

and $R_1 = R_2 - \Delta$. When used in (24), The values of Δ , based on (31), and R_1 , based on (30) and (31), will yield the minimum condition number, thus the best well-conditioned system, subject to the maximum allowable VSWR in the system, if the measurement resistance values are to be chosen with equal increments of Δ .

VI. CONCLUSION

Proper installation of an RF power amplifier requires knowledge of the amplifier output impedance. With such information, correct load matching is made possible. Matching considerations address power output, efficiency, spurious signal rejection qualities, and possible system longevity. Presented here is a straightforward way to determine the amplifier's output impedance. The method has been checked through operational tests and simulation. Additionally provided is a complete sensitivity analysis for the technique.

ACKNOWLEDGMENT

The authors express sincere gratitude to Mr. William McConnell of Northrop Grumman Corporation, Electronic Systems Division for his support, friendship, and suggestions for this research.

REFERENCES

- [1] A. Abramovitz, "A Practical Approach for Analysis of Input and Output Impedance of Feedback Amplifiers," *IEEE Transactions on Education*, vol. 52, no. 1, pp. 169-176, Feb. 2009.
- [2] Z. Wang, S. Gao, C.-W. Park, "A Simple Method for Tunable Load Impedance Matching Network

of Power Amplifier," *International Conference on Microwave and Millimeter Wave Technology (ICMMT)*, pp. 484-487, 2010.

- [3] M. Pierpoint, R. D. Pollard, J. R. Richardson, "An Automated Measurement Technique for Measuring Amplifier Load-Pull and Verifying Large Signal Device Models," *IEEE - MTT-S International Microwave Symposium Digest*, pp. 625-628, 1986.
- [4] R. E. Serrano-Finetti, "Output Impedance Measurement Low Power Sources and Conditioners," *IEEE Transactions on Instrumentation and Measurement*, vol. 58, no. 1, pp. 180-186, Jan. 2009.
- [5] Frederick E. Terman, *Electronics and Radio Engineering*, NY: McGraw-Hill, 1955.
- [6] Paul M. Chirlian, *Basic Network Theory*, NY: McGraw-Hill, 1969.
- [7] V. Zomorrodian, U. K. Mishra, R. A. York, "Modeling of CPW Based Passive Networks using Sonnet Simulations for High Efficiency Power Amplifier MMIC Design," *Journal of The Applied Computational Electromagnetics Society (ACES)*, vol. 26, no. 2, pp. 131-140, February 2011.
- [8] Nathan Marcuvitz, *Waveguide Handbook*, NY: McGraw-Hill, 1951.
- [9] B. James Ley, Samuel G. Lutz and Charles F. Rehberg, *Linear Circuit Analysis*, NY: McGraw-Hill, 1959.
- [10] Gabor C. Temes and Jack W. LaPatra, *Circuit Synthesis and Design*, NY: McGraw-Hill, 1977.
- [11] A. K. Kaw, *Introduction to Matrix Algebra*, lulu.com, March 2008.



Vincent P. McGinn is a Professor of Electrical Engineering at Northern Illinois University. His Ph.D. is from the Pennsylvania State University and his teaching venue includes Fordham University, Penn State, The University of Tulsa, VMI and the Air Force Institute of Technology. He has authored numerous publications on low observables, electromagnetic compatibility, and high frequency radiation. His employment has included numerous aerospace firms including Rockwell International and Northrop Grumman. Dr. McGinn is a member of Eta Kappa Nu, Tau Beta Pi and is a registered professional engineer. He is also an IEEE Wireless Certified Professional (WCP).



Veysel Demir received the B.Sc. degree in Electrical Engineering from Middle East Technical University, Ankara, Turkey, in 1997 and the M.Sc. and Ph.D. degrees in Electrical Engineering from Syracuse University, Syracuse, NY, in 2002 and 2004,

respectively.

During his graduate studies, he worked as a Research Assistant at Sonnet Software, Inc., Liverpool, NY. He worked as a Visiting Research Scholar in the Department of Electrical Engineering at the University of Mississippi from 2004 to 2007. He joined the Department of Electrical Engineering at Northern Illinois University as an Assistant Professor in August 2007. His research interests include numerical analysis techniques as well as microwave and radiofrequency (RF) circuit analysis and design. He has coauthored more than 40 technical journal and conference papers. He is a coauthor of the books *Electromagnetic Scattering Using the Iterative Multiregion Technique* (Morgan & Claypool, 2007) and *The Finite Difference Time Domain Method for Electromagnetics with MATLAB Simulations* (Scitech 2009).

Dr. Demir is a member of IEEE, Sigma Xi, and Applied Computational Electromagnetics Society (ACES).

Optimization of Reception Antenna Composed with Unbalanced Fed Inverted L Element for Digital Terrestrial Television

Daisuke Yagyū¹ and Mitsuo Taguchi²

¹ Information Media Center
Nagasaki University, Nagasaki, 852-8521, Japan
d-yagyū@nagasaki-u.ac.jp

² Division of Electrical Eng. & Computer Science, Graduate School of Engineering
Nagasaki University, Nagasaki, 852-8521, Japan
mtaguchi@nagasaki-u.ac.jp

Abstract — The structure of the array antenna for the reception antenna of the digital terrestrial television broadcasting in Japan is optimized by PSO algorithm. The unbalanced fed ultra low profile inverted L antenna is used as the driven element and two wires are located at the forward and backward directions of the driven element. In the case of antenna size of 170 mm by 325 mm by 29 mm, the return loss bandwidth less than -10 dB is satisfied at the whole broadcasting frequency band (240 MHz) and the directivity of 5.44 dBi to 7.19 dBi is obtained. In the numerical analysis, the electromagnetic simulator WIPL-D based on the method of moment is used.

Index Terms — Inverted L antenna, PSO, reception antenna, WIPL-D.

I. INTRODUCTION

The digital terrestrial television broadcasting in Japan started on December 2003, and the analog broadcasting ended on July 2011 except the devastated area by the Great East Japan Earthquake [1]. For the reception of the conventional analog terrestrial broadcasting, directional antennas with high gain, and high front-to-back ratio, such as the Yagi-Uda antenna, are used in order to suppress the ghost image due to the echo. On the other hand, a small antenna with low front-to-back ratio is sufficient for the reception of the digital terrestrial broadcasting. By now, many antennas such as a square loop

antenna, a planar antenna, and a W-loop antenna mounted on a car window are proposed for the reception antenna of the terrestrial television broadcasting [2-4]. The authors have proposed the planar sleeve antenna composed of a coplanar waveguide for the reception antenna of the digital terrestrial television [5]. Although good return loss characteristics are obtained at the whole broadcasting frequency band, the directivity becomes low (2.32 dBi to 3 dBi). The high gain antenna is desired for the reception at the far area from the broadcasting station.

The authors have proposed two element phased array dipole antennas [6]. Two half-wave dipoles with 90 degree phase difference feed are located with a distance of less than a quarter wavelength. By controlling the mutual coupling between two dipoles, a front-to-back ratio of 15.3 dB is obtained. Then the authors have proposed an ultra low profile inverted L antenna located on parallel wire conductors [7]. This antenna consists of a coaxial line. The inner conductor of the coaxial line is extended from the end of the outer conductor, that is, this antenna is excited at the end of the outer conductor. The antenna height is around $\lambda/30$ (λ : wavelength). The length of the horizontal element of this antenna is almost a quarter wavelength. In the case of the length of parallel wires is 0.49λ and three wires are located with the width of 0.124λ , the maximum gain becomes 3.99 dBi and the return loss bandwidth less than -10 dB is 6.13 %. The authors used an

ultra low profile inverted L antenna located on parallel conducting wires for the driven element of three element array antenna for the reception antenna of the terrestrial television [8]. In order to widen the return loss bandwidth, the antenna height h becomes larger and the distance between horizontal wires $p_{xp} = p_{xm}$ are shorter compared with those in [7]. Although the directivity of 6.0 dBi to 7.77 dBi is obtained, the return loss bandwidth is satisfied only for 170 MHz of the television frequencies from 470 MHz to 710 MHz.

In this paper, the particle swarm optimization (PSO) algorithm [9, 10] is used for the optimization of the geometry parameters of the antenna proposed in [8] to satisfy the return loss less than -10 dB from 470 MHz to 710 MHz. The genetic algorithm is also used for the optimization of the antenna structure [11-13]. Since there are ten parameters should be optimized and the handling of the real number is easy in the PSO, the PSO algorithm is used for the optimization in this paper. In the numerical analysis, the electromagnetic simulator WIPL-D based on the method of moment is used [14].

II. ANALYTICAL MODEL

Figure 1 shows the structure of the analytical model. The driven element No. 1 is an ultra low profiled inverted L antenna located on three parallel wires. The inverted L antenna is composed of a coaxial radiator. This antenna consists of a horizontal arm in the y -direction and a small leg in the z -direction. The inner conductor of the coaxial line is extended from the end of an outer conductor, that is, this antenna is excited at the end of an outer conductor. The parallel wires are connected to each other by a single perpendicular wire at the base of the inverted L antenna. The length of horizontal element L determines the resonant frequency. The length $L1$ is adjusted for the impedance matching. The radii of outer and inner conductors of the coaxial line are 1.095 mm and 0.255 mm, respectively. The radius of parallel wire a is 1.5 mm. The height of the horizontal element is h . The wire elements No. 2 and No. 3 are located in the forward and backward directions of antenna. In this paper, the Smith chart and the return loss are normalized by the characteristic impedance 75Ω of the feeder of the television receiver.

III. ALGORITHM OF OPTIMIZATION

PSO algorithm is a population-based stochastic approach for solving continuous and discrete optimization problems [9, 10]. PSO algorithm and its conditions used, in this paper, are described as follows.

A. Solution space

Solution Space: 10-dimension

Dz : 40 to 120[80],

Dy : 130 to 290[208],

Rz : -120 to -40[-65],

Ry : 300 to 460[320]

h : 15 to 35[24.5],

L : 90 to 170[130],

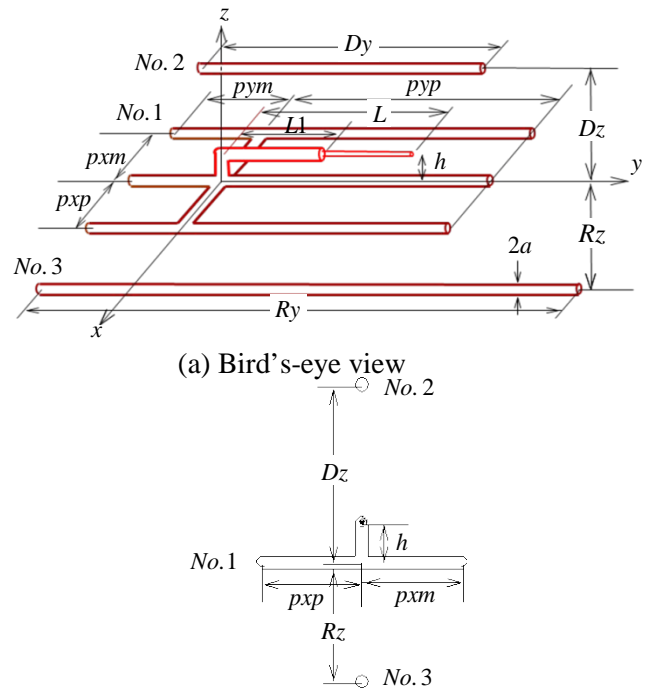
$L1$: 25 to 65[41]

$p_{xp}=p_{xm}$: 10 to 70[40],

p_{ym} : 14 to 74[44],

p_{yp} : 150 to 270[210]

A unit of all parameters is mm. The value in [] shows a value shown in [8].



(b) Cross sectional view seen from y -direction
 Fig. 1. Analytical model of antenna.

A minimum and maximum value for each dimension in the 10-dimensional optimization is referred to as $Xmin_n$ and $Xmax_n$, respectively, where n ranges from 1 to 10.

B. Fitness function

In this paper, the fitness value is calculated by a bandwidth. The bandwidth is defined as the frequency range where the return loss is less than -10 dB at 75 Ω system. The fitness value is defined by the following equation:

$$fitness\ value = \min(F_L, F_H) + 0.1|F_H - F_L|, \quad (1)$$

$$F_L = f_c - f_{lowest}, \quad F_H = f_{highest} - f_c$$

where f_{lowest} and $f_{highest}$ is the lowest and highest frequency of calculated frequency band, respectively. f_c is defined as the center frequency 590 MHz of the frequency band of the digital terrestrial television broadcasting in Japan. If F_L or F_H becomes less than zero, then it is set to be zero. If the calculated frequency band differs from the broadcasting frequency band, F_L differs from F_H . Then, the first term of equation (1) takes the smaller value of F_L and F_H . The fitness value is increased in the updating step. Therefore, the lower value of F_L and F_H becomes large. This means that the center frequency of the calculation frequency band approaches to f_c in the optimization process. The second term of equation (1) accelerates the extending of the return loss bandwidth. In this paper, the coefficient of the second term is fixed as 0.1 based on our experience.

C. Initialization

Each particle begins at its own random location with a velocity that is random both in its direction and magnitude. Initial position in each dimension is given in the following equation:

$$x_n = \text{rand}(\) * (Xmax_n - Xmin_n) + Xmin_n, \quad (2)$$

where x_n is the particle's coordinate in the n -th dimension. The random number function $\text{rand}(\)$ returns a number between 0.0 and 1.0.

In this paper, the absolute value of velocities of each particle is limited to 10% of the analytical range in each dimension. $Vmax_n$ shows the maximum limit of the absolute value of velocities. $Vmax_n$ is defined as

$$Vmax_n = 0.1 * (Xmax_n - Xmin_n). \quad (3)$$

The initial velocity defined as

$$v_n = \{2 * \text{rand}(\) - 1\} * Vmax_n, \quad (4)$$

where v_n is the velocity of the particle in the n -th dimension. v_n takes an arbitrary value from $-Vmax_n$ to $Vmax_n$.

D. Iterations

The following procedures are iterated.

1) Evaluate the particle's fitness:

The fitness value is computed by the coordinate of each particle. In the numerical analysis of antenna characteristics, the electromagnetic simulator WIPL-D based on the method of moment is used. The coordinate and the velocity of each particle are calculated by the program written in FORTRAN. This program generates an input file of WIPL-D and executes the solver of WIPL-D. In addition, this program demands the return loss from the input impedance value that WIPL-D output. The antenna characteristics and the return loss are calculated at every 5 MHz from 450 MHz to 1 GHz. The larger frequency increment is preferable from the standpoint of the computation time. However, the input impedance characteristics rapidly vary as shown in Fig. 4. Therefore, the frequency increment of 5 MHz is chosen.

2) Compare to $pbest$, $gbest$:

$pbest$ is the location in parameter space of the best fitness returned for a specific particle. $gbest$ is the location in parameter space of the best fitness returned for the entire swarm. If the fitness value resulting from a change in coordinate of a particle is larger than the fitness value at $pbest$ of each particle, $pbest$ is changed by that coordinate. In the first iteration, each $pbest$ is defined as the initial state of each particle.

If the fitness value resulting from a change in coordinate of each particle is larger than the fitness value at $gbest$, $gbest$ is changed by that coordinate. In the first iteration, $gbest$ is defined as the coordinate of the particle with best fitness.

3) Update the particle's velocity:

For the next iteration, the velocity of the particle is changed according to the relative locations of $pbest$ and $gbest$. It is accelerated in the directions of these locations of greatest fitness according to the following equation:

$$v_n = w * v_n + c_1 * \text{rand}() \times (pbest_n - x_n) + c_2 * \text{rand}() \times (gbest_n - x_n). \quad (5)$$

The new velocity is simply the old velocity scaled by w and increased in the direction of $gbest$ and $pbest$ for that particular dimension. c_1 and c_2 are scaling factors. In this paper, $w=0.729$, $c_1=c_2=1.494$ [10]. If the absolute value of v_n is greater than $Vmax_n$, v_n is assumed to be $Vmax_n$ or $-Vmax_n$.

4) Move the particle:

For the next iteration, new coordinate x_n is calculated for each dimension according to the following equation:

$$x_n = x_n + v_n * \Delta t. \quad (6)$$

In this paper, Δt is assumed to be 1.

5) Boundary conditions:

In this paper, as for the boundary condition to limit the coordinate of each particle in solution space, the absorbing wall is adopted. That is, if new calculated coordinate x_n is less than $Xmin_n$, x_n is replaced as $Xmin_n$. If x_n is greater than $Xmax_n$, x_n is replaced as $Xmax_n$. In either case, v_n is set to zero.

IV. RESULTS AND DISCUSSION

Table 1 shows the comparison of the fitness value for the different number of population. The number of trial is 10. gFIT indicates the best fitness at the number of iteration IX. If the return loss bandwidth is satisfied at the whole broadcasting frequency band (240 MHz), IX indicates the number of iteration when the return loss bandwidth of 240 MHz is obtained at the first time. As the number of population is increased, the good results satisfying the return loss bandwidth are slightly increased. Therefore, from the standpoint of computation time, the number of population is fixed to 50 in the optimization in the subsequent sections.

Based on the above-mentioned algorithm, the antenna parameters with the bandwidth of 240 MHz and more are obtained. The number of unknowns on WIPL-D is 25. The average computation time for the population of 50 and the iteration of 50 is about 6 hours 40 minutes by using PC with AMD Turion™ 64 processor driven at 2 GHz.

Figure 2 shows the example of the convergence of fitness value in the case of population of 50 and the number of maximum iteration is 50. In this trial, the fitness value which satisfies the return

Table 1: Fitness value for different number of population

	50		60		70		80	
	IX	gFIT	IX	gFIT	IX	gFIT	IX	gFIT
1	37	115.0	29	116.5	29	111.0	20	120.0
2	38	120.0	37	120.5	47	120.0	30	120.0
3	33	120.0	45	120.0	26	116.0	21	121.0
4	49	105.0	46	116.5	32	120.0	40	115.0
5	23	120.0	44	120.5	49	121.5	22	115.0
6	36	110.0	47	86.0	49	120.5	44	115.0
7	42	110.5	34	105.0	36	116.0	18	120.0
8	45	120.0	29	120.5	42	95.5	11	120.0
9	33	105.5	38	115.0	18	120.0	47	115.5
10	37	66.0	47	115.5	35	116.5	46	116.0

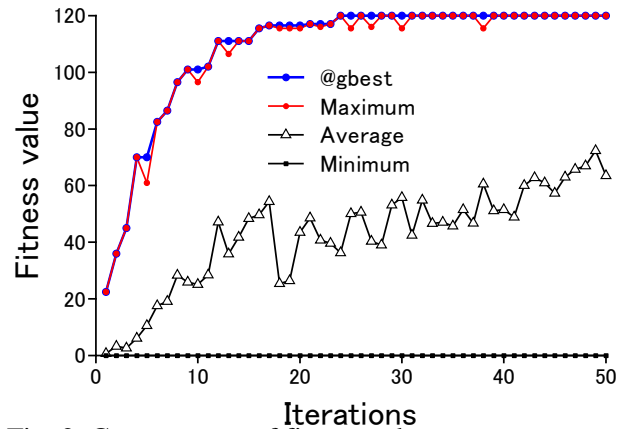


Fig. 2. Convergence of fitness value.

loss bandwidth of 240 MHz is obtained at the number of iteration of 25.

Figure 3 shows the distribution of D_y as the function of D_z , and R_y as the function of R_z from

the obtained antenna parameters. The distribution of R_y can be divided to the following five groups:

- Group A: $R_z < -85, R_y < 347.5,$
- Group B: $-84 < R_z < -80, 365 < R_y < 385,$
- Group C: $R_z > -79.2, R_y < 382.5,$
- Group D: $R_z < -91.5, R_y > 385,$
- Group E: $R_z > -77.6, R_y > 400.$

In each group, the typical antenna parameters are choosing from the solution in the dense portion in the figure of $R_z - R_y$. Figures 4 and 5 show the input impedance and the return loss characteristics of the antenna of each group, respectively. Figure 6 shows the directivities of antennas of all groups. The directivity of the antenna in Group A becomes higher at the lower frequencies. The parameters of antenna in Group A are as follows; $D_z = 74.0$ mm, $D_y = 185.9$ mm, $R_z = -92.7$ mm, $R_y = 325.0$ mm, $h = 30.6$ mm, $L = 121.4$ mm, $L1 = 25.9$ mm, $pxp = pxm = 12.9$ mm, $pym = 31.6$ mm, $pyp = 214.8$ mm. The element No. 3 is located for extending the return loss bandwidth at lower frequencies. The average value of the length of the element No. 3 is 325.5 mm in the Group A, as shown in Figure 3. This length is almost a half wave length at the lowest frequency. Therefore, the directivity of the Group A is improved at lower frequencies.

Figure 7 shows the distribution of D_y as the function of D_z , and R_y as the function of R_z in Group A. Four sample data are shown in these figures. Figures 8 and 9 show the input impedance and return loss characteristics of four sample antennas, respectively. Figure 9 shows the directivity of these antennas. The directivity of these antennas are almost the same.

Figures 10 and 11 show the electric field radiation patterns of the antenna of Group A in xz -plane and yz -plane, respectively. Figure 12 shows the comparison of the return loss and the directivity characteristics for the initial design [8] and the optimized solution (Group A).

Figure 13 shows the photograph of fabricated antenna. The inverted L element is fabricated by the semi rigid coaxial cable with the characteristic impedance of 50Ω . The coaxial cable is extended from the base point of antenna to the backward of parallel wires. The antenna is fixed by the expanded polystyrene. In order to measure the input impedance at the feed point not the return loss, the length of coaxial cable has to be compensated. Since this compensation is not so easy, the return loss is measured by the vector

network analyzer with the characteristic impedance of 50Ω . Figure 14 shows the comparison of measured and calculated return loss characteristics normalized by 50Ω . Since the width of parallel wires ($pxm + pxp$) is narrower than the wavelength, the leakage current may flow on the surface of semi rigid cable. This may cause the discrepancy between calculated and measured data at the lower frequencies.

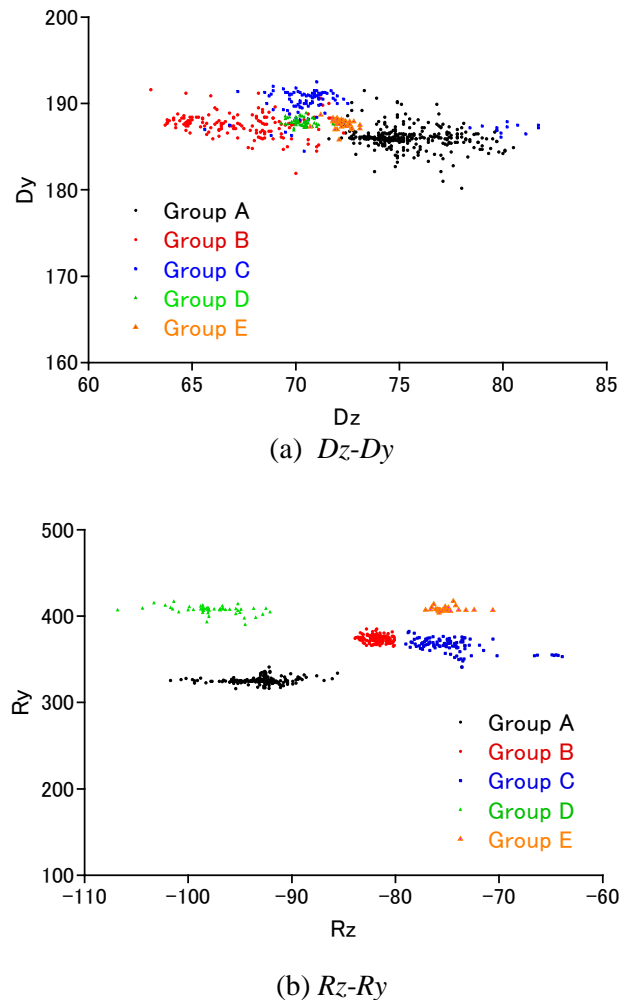


Fig. 3. Distribution of optimized results.

V. CONCLUSION

As the reception antenna of the terrestrial digital television, three element array antenna has been proposed and its structure has been optimized by applying PSO algorithm. The unbalanced fed ultra low profile inverted L antenna on three parallel wires is used as the driven element of proposed antenna. In the case of antenna size of

170 mm by 325 mm by 29 mm, the return loss bandwidth of 240 MHz and the directivity of 5.44 dBi to 7.19 dBi are obtained.

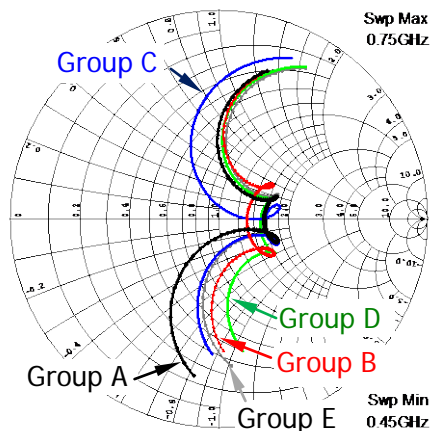


Fig. 4. Input impedance characteristics.

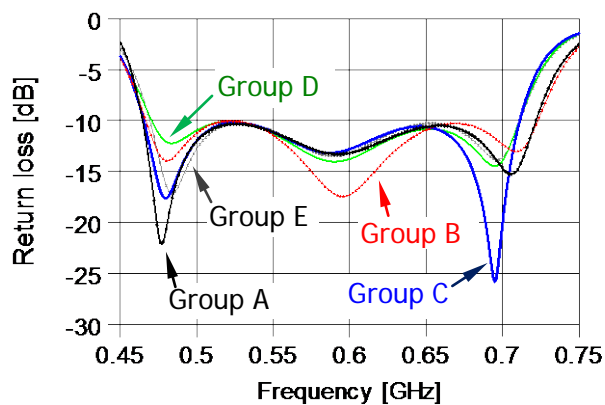


Fig. 5. Return loss characteristics.

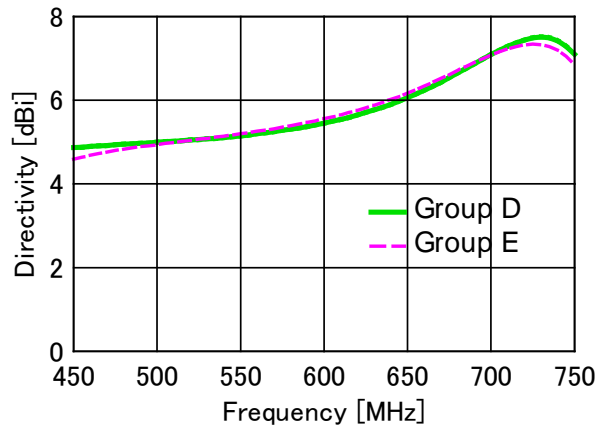
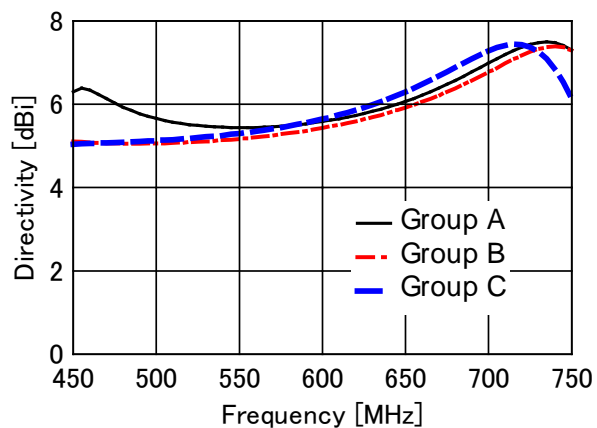


Fig. 6. Directivity characteristics.

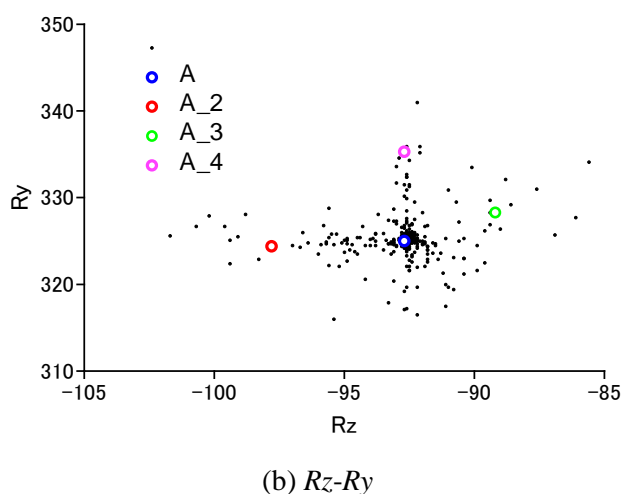
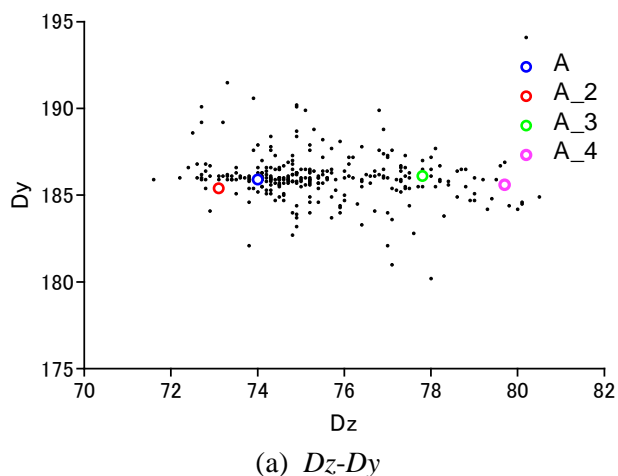


Fig. 7. Distribution of optimized results.

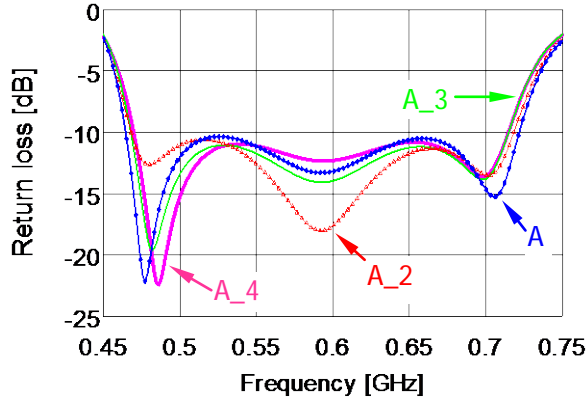


Fig. 8. Return loss characteristics.

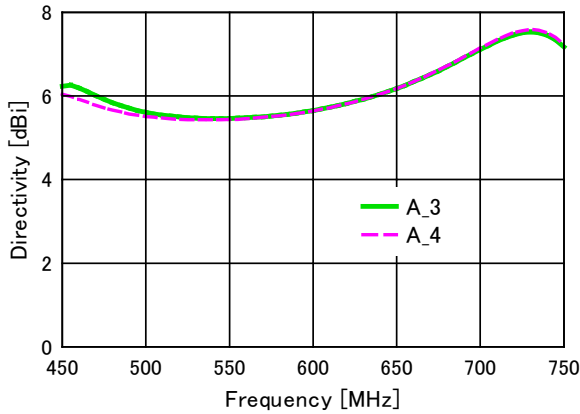
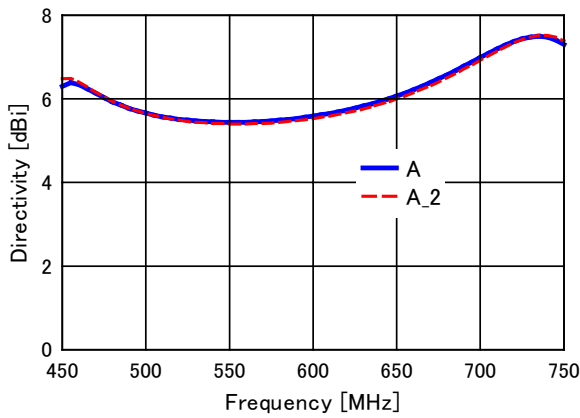


Fig. 9. Directivity characteristics.

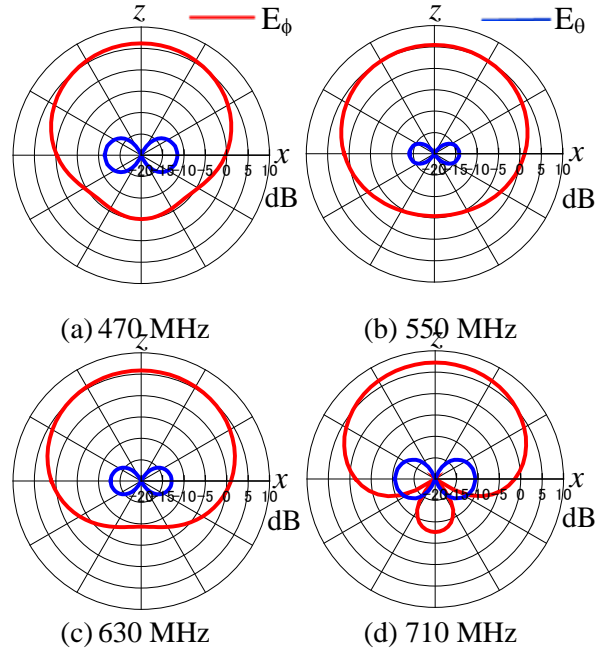


Fig. 10. Electric field radiation patterns in xz -plane. $Dz = 74.0$ mm, $Dy = 185.9$ mm, $Rz = -92.7$ mm, $Ry = 325.0$ mm, $h = 30.6$ mm, $L = 121.4$ mm, $Ll = 25.9$ mm, $pxp = pxm = 12.9$ mm, $pym = 31.6$ mm, $pyp = 214.8$ mm.

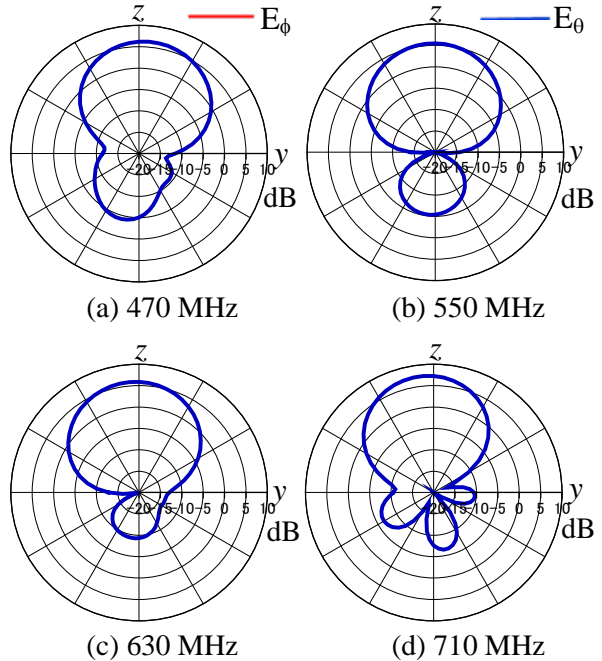


Fig. 11. Electric field radiation patterns in yz -plane. $Dz = 74.0$ mm, $Dy = 185.9$ mm, $Rz = -92.7$ mm, $Ry = 325.0$ mm, $h = 30.6$ mm, $L = 121.4$ mm, $Ll = 25.9$ mm, $pxp = pxm = 12.9$ mm, $pym = 31.6$ mm, $pyp = 214.8$ mm.

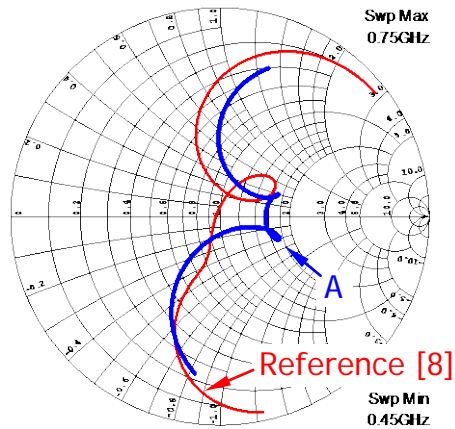


Fig. 12. Comparison of input impedance characteristics for initial design and optimized solution.

$D_z = 74.0$ mm, $D_y = 185.9$ mm, $R_z = -92.7$ mm, $R_y = 325.0$ mm, $h = 30.6$ mm, $L = 121.4$ mm, $L1 = 25.9$ mm, $p_{xp} = p_{xm} = 12.9$ mm, $p_{ym} = 31.6$ mm, $p_{yp} = 214.8$ mm.



Fig. 13. Photograph of fabricated antenna.

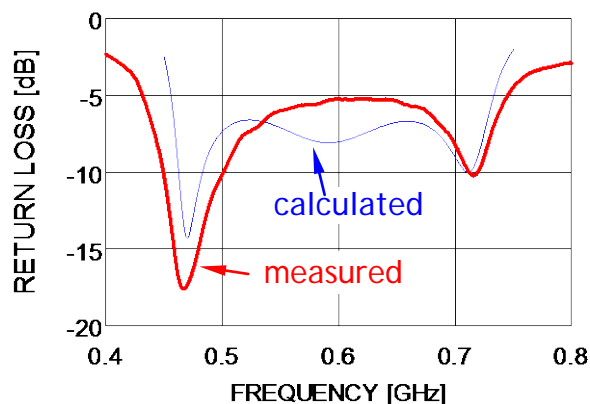


Fig. 14. Return loss characteristics normalized by 50Ω .

REFERENCES

- [1] M. Taguchi, "Portable TV Antennas," in *Antenna Engineering Handbook, Fourth Edition*, Chap. 30, New York: McGraw-Hill, 2007.
- [2] Y. Okano, "Development of Tabular Broad Band Antenna for UHF-TV," *Trans. ICICE*, vol. J85-B, no. 8, pp. 1426-1433, Aug. 2002. (in Japanese).
- [3] Y. Okano and K. Sakauchi, "Development of Convenient Planar Broadband Antenna for Terrestrial Digital Broadcasting," *Trans. IEICE*, vol. J90-B, no. 7, pp. 679-688, July 2007. (in Japanese).
- [4] T. Sato, N. Michishita, Y. Yamada, and K. Ogino, "Measurement of Electrical Characteristics of W-Loop Antenna Mounted on Car for Digital Terrestrial Broadcasting," *Trans. IEICE*, vol. J91-B, no. 9, pp. 1069-1071, Spt. 2008. (in Japanese).
- [5] Y. Seto and M. Taguchi, "Planar Sleeve Antenna for Reception of Digital Terrestrial Television," *IEICE Technical Report*, no. AP2009-21, May 2009. (in Japanese).
- [6] M. Taguchi, K. Era, and K. Tanaka, "Two Element Phased Array Dipole Antenna," *Applied Computational Electromagnetic Society (ACES) Journal*, vol. 22, no. 1, pp. 112 - 116, March 2007.
- [7] M. Taguchi and T. Araki, "Ultra Low Profile Inverted L Antenna on Parallel Wires," *Proc. on 26th Annual Review of Progress in Applied Computational Electromagnetics*, pp. 652-655, April 2010.
- [8] M. Taguchi and Shaojie Yang, "Reception Antenna Composed with Unbalanced Fed Inverted L Element for Digital Terrestrial Television in Japan," *Proc. on 2010 Int. Conference on Communications, Circuits and Systems, #07_M1_03*, July 2010.
- [9] J. Kennedy and R. C. Eberhart, "Particle Swarm Optimization," *Proc. IEEE Int. Conf. Neural Networks*, vol. IV, pp. 1942-1948, Piscataway, NJ, 1995.
- [10] J. Robinson and Y. Rahmat-Samii, "Particle Swarm Optimization in Electromagnetics," *IEEE Trans. Antennas Propag.*, vol. 52, no. 2, pp. 397-407, Feb. 2003.
- [11] B. J. Barbisch, D. H. Werner, and P. L. Werner, "A Genetic Algorithm Optimization Procedure for the Design of Uniformly Excited and Nonuniformly Spaced Broadband Low Sidelobe Arrays," *Applied Computational Electromagnetic Society (ACES) Journal*, vol. 15, no. 2, pp. 34-42, July 2000.
- [12] D. S. Linden and R. MacMillan, "Increasing Genetic Algorithm Efficiency for Wire Antenna Design Using Clustering," *Applied Computational Electromagnetic Society (ACES) Journal*, vol. 15, no. 2, pp. 75-86, July 2000.
- [13] C. M. de J. van Coevorden, A. R. Bretones, M. F. Pantoja, S. G. Garcia, and A. Monorchio, "A New

Implementation of the Hybrid Taguchi GA: Application to the design of a Miniaturized Log-Periodic Thin-Wire Antenna,” *Applied Computational Electromagnetic Society (ACES) Journal*, vol. 24, no. 1, pp. 21-31, February 2009.

[14] WIPL-D d.o.o.: <http://www.wipl-d.com/>, WIPL-D Pro v7.0, 2008.



Daisuke Yagyu Prof. Daisuke Yagyu received his B. E. and M. E. degrees from Nagasaki University, Japan in 1994 and 1996, respectively. From 2000 to 2006, he was a Research Associate at Nagasaki University.

Since 2007, he has been an Assistant Professor at Nagasaki University. His research interests are the antennas for wide band communications and the computer networks.

He is a member of the Institute of Electronics, Information and Communication Engineers of Japan.



Mitsuo Taguchi Prof. Mitsuo Taguchi received his B. E. and M. E. degrees from Saga University, Japan in 1975 and 1977, respectively, and a Dr. Eng. Degree from Kyushu University Japan in 1986. From 1977 to 1987, he was a Research Associate at Saga University. From 1987 to 2007, he

was an Associate Professor at Nagasaki University.

Since 2007, he has been a Professor at Nagasaki University. In 1996 he was a visiting researcher at the Department of Electrical Engineering at the University of California, Los Angeles. His research interests are the small antenna for mobile communication and UWB antennas. Dr. Taguchi is a member of ACES, IEEE, the Institute of Electronics, Information and Communication Engineers of Japan and the Institute of Image Information and Television Engineers of Japan.

Optimum Design of SIW Longitudinal Slot Array Antennas with Specified Radiation Patterns

S. E. Hosseinijad, N. Komjani, H. Oraizim, and M. T. Noghani

Department of Electrical Engineering
Iran University of Science and Technology, Narmak, Tehran, 16846-13114, Iran
ehsan_hosseinijad@elec.iust.ac.ir

Abstract — In this paper, an optimum design is presented for substrate integrated waveguide (SIW) longitudinal slot array antennas based on the method of least squares (MLS). Elliott's design procedure for dielectric filled waveguides is considered, taking into account the internal and external mutual couplings. The MLS error function is a multi-term function based on design goals, including specified radiation patterns and matching of the input impedance. We use the hybrid method of genetic algorithm-conjugate gradient for the error function minimization. This approach is very effective because of combining the “pattern synthesis” with “impedance matching” and “calculation of array parameters”. This procedure increases the speed of design as well as synthesizing patterns with specified characteristics. The MLS design results and those obtained by HFSS and CST simulation software are in good agreement and verify the accuracy of the proposed method.

Index Terms — MLS, optimization, slot array, and SIW.

I. INTRODUCTION

Waveguide slot array antennas have many applications in communication and radar systems [1-2], due to their significant advantages such as: high efficiency, high gain, mechanical strength, and the absence of spurious radiations from the feed system. The most common configuration for slot array antennas is the longitudinal slots due to low cross polarized levels. Using Elliott's design

procedure [3-5], a slot array can be accurately synthesised.

SIW is a new structure proposed to replace the conventional rectangular waveguide [6-10]. Having the benefits of rectangular waveguides, SIWs are easily fabricated, have lower cost, smaller size, lower weight, and are easier integrated with other planar circuits. As a result, SIW is a good structure for microwave and millimeter-wave applications.

Using the equivalent waveguide for SIW, one can use Elliott's design procedure to design the SIW longitudinal slot array antennas. SIWs have considerably lower height than common rectangular waveguides. Thus, the internal mutual coupling of higher order modes is significant. Consequently, it is suitable to use the design formulas of [5], which account for the three sources forming the field of slots, namely: incident field (TE_{10}), external, and internal coupling.

This paper presents an optimum method for the design of SIW longitudinal slot array antennas, based on the method of least squares (MLS). An error function is formulated consisting of three terms, namely those for the design equations, input impedance matching, and pattern synthesis. The error function is then minimized with respect to the design parameters (namely slot lengths, offsets, and excitation) using the hybrid method of genetic algorithm and conjugate gradient method.

II. DESIGN PROCEDURE

A. SIW design

First, the SIW should be designed for the desired operating frequency. The structure is

shown in Fig. 1 where d is the diameter of metallic vias, p is the distance between them, h is the height and a_{SIW} is the width of SIW. There is a region in the plane of d - p where the SIW is equivalent to a metallic rectangular waveguide and has similar guiding characteristics [7].

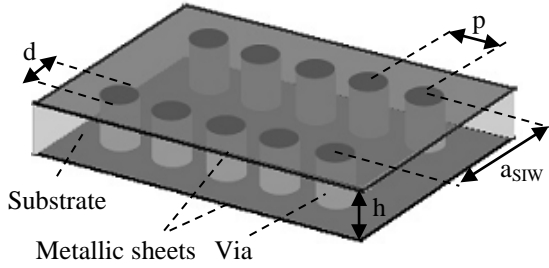


Fig. 1. SIW structure.

This region has the following properties:

- 1- It does not present any band-gap in its operating bandwidth ($p < 0.25 \lambda_c$).
- 2- It has negligible leakage loss ($p \leq 2d$).
- 3- It is physically realizable ($p > d$).

where, λ_c is the cutoff wavelength of the TE_{10} mode. An accurate empirical formula has been proposed in [8, equation 21], which gives an error of less than 1% for the condition $p > 1.2d$. Consequently, the region can be defined as:

$$p < 0.25 \lambda_c. \quad (1)$$

$$1.2d < p \leq 2d. \quad (2)$$

The operating frequency is set between the cutoff frequency of TE_{10} and TE_{20} modes by choosing the correct width for the SIW (a_{SIW}). This, results in a single mode waveguide (only TE_{10}).

B. Calculation of the isolated slot admittance

The isolated admittance of a slot (Y/G_0) can be obtained by different methods such as: direct measurements, analytical calculations or computer aided simulations. We have used a finite-element commercial software (HFSS) due to its simplicity and lower cost.

The simulation model is shown in Fig. 2 in which the admittance matrix at the test port and the center of slot are equivalent. Having done the simulation, one could plot the parametric curves of Y/G_0 with respect to the slot length ($2l$) and offset (x); and then obtain a closed form function for the normalized admittance of the isolated slot. The

admittance characteristics exhibit stronger dependency on the slot parameters in the SIW with much thinner height [10]. Consequently, to achieve high accuracy in curve fitting, polynomial functions with steps $0.1mm$ for $2l$ are used. The closed forms of real and imaginary parts of Y/G_0 are:

$$(Y/G_0)_{real} = r_i(x)(2l) + r_0(x),$$

$$r_i(x) = t_{i2}x^2 + t_{i1}x + t_{i0}, \quad i = 0,1. \quad (3)$$

$$(Y/G_0)_{imag} = i_1(x)(2l) + i_0(x),$$

$$i_i(x) = u_{j2}x^2 + u_{j1}x + u_{j0}, \quad i = 0,1. \quad (4)$$

For example, at the frequency of $f=10GHz$ according to the SIW design rules mentioned in the previous section, the following parameters are considered: $d=0.5mm$, $p=0.9mm$, $a_{SIW}=15.4mm$, $\epsilon_r=2.2$ and $h=1.5mm$. The metallic sheet thickness is $0.1mm$ and the slot width is $0.5mm$. The resulted curves are shown in Fig. 3.

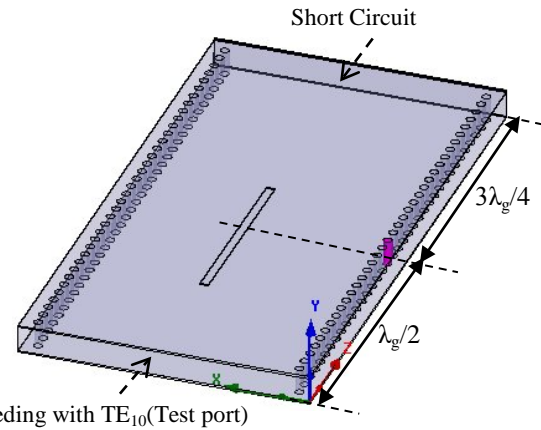


Fig. 2. The simulation model used to calculate the Y/G_0

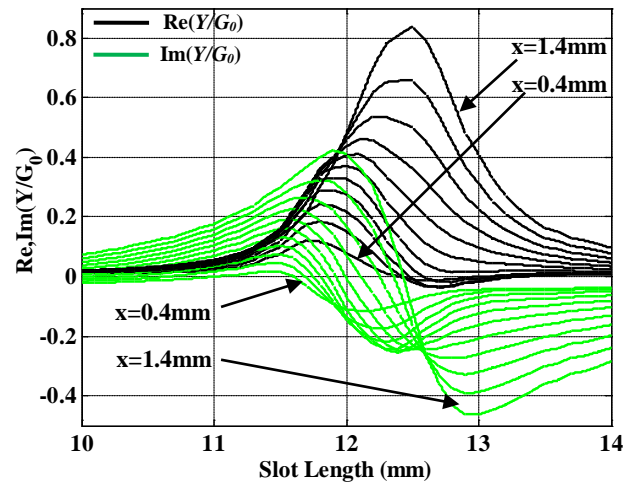


Fig. 3. Normalized admittance of an isolated slot with steps $0.1mm$ for offset.

C. The error function

The total error function is formulated according to the design goals, consisting of three terms, namely one for the two design equations, one for the impedance matching and the third for the pattern synthesis. Then:

$$\mathcal{E}_{total} = \mathcal{E}_{design_equ} + \mathcal{E}_{input_match} + \mathcal{E}_{synthesis} \quad (5)$$

1. The error function for design equation

Design equations for a linear array of slots with standing-wave excitation is presented in [5]. The error function for design equations is:

$$\mathcal{E}_{design_equ} = W_1 \sum_{n=1}^N \sum_{m=1}^N \left| \frac{f_n \left(\frac{2f_m^2}{Y_m/G_0} + MC_m \right)}{f_m \left(\frac{2f_n^2}{Y_n/G_0} + MC_n \right)} \frac{V_n^s}{V_m^s} \right|^2, \quad (6)$$

where, W_1 is the weighting function. Definitions of all other symbols are found in [5]. This equation is obtained by setting the two fundamental design equations equal, and dividing the terms corresponding to the mn 'th slot by the ij 'th slot in the array.

2. The error function for impedance matching

Since slot spacings are half a wavelength, the input admittance of the equivalent transmission line model is written as the sum of all the active admittances of slots:

$$Y_{in} = \sum_{n=1}^N \frac{Y_n^a}{G_0} = \sum_{n=1}^N \frac{2f_n^2}{Q_n} = 1 + j0. \quad (7)$$

So we can write this part of the error function as follows:

$$\mathcal{E}_{input_match} = \mathcal{E}_{real} + \mathcal{E}_{imag} \\ = W_2 \left| \text{Re}(Y_{in}) - 1 \right|^2 + W_3 \left| \text{Im}(Y_{in}) \right|^2. \quad (8)$$

3. The error function for pattern synthesis

The pattern of the linear array (including the element factor due to slot):

$$S(\theta) = \sum_{n=1}^N \left| \frac{V_n^s}{V_1^s} \right| s_n(\theta) e^{jn(k_0 \frac{\lambda_0}{2} \cos \theta)}, \quad (9)$$

where, $k_0 = 2\pi/\lambda_0$ and $s_n(\theta)$ is the element factor of n 'th slot is derived by making the slot equivalent to a dipole of length $2l_n$:

$$s_n(\theta) = \frac{\cos(kl_n \cos \theta) - \cos(kl_n)}{\sin \theta}. \quad (10)$$

The error function of pattern synthesis is written as:

$$\mathcal{E}_{synthesis} = W_4 \left| S(\theta) - S_{spec}(\theta) \right|^2, \quad (11)$$

where, $S_{spec}(\theta)$ is the specified pattern with desired characteristic such as sidelobe level, gain and beamwidth.

4. Minimization technique of the error function

The MLS error function of the slot array design is a very complex multi-variable function. Finding optimum solutions is a challenging problem due to the presence of many extrema. Global optimization (GO) methods such as genetic algorithm (GA) or local optimization (LO) methods such as conjugate gradient (CG) cannot be used solely since: 1. GO methods may require long processing time, since they iteratively evolve toward the exact solution by means of probabilistic rules. They also devote more effort to search for the global optimum region instead of finding the precise position of the local optimum. 2. LO methods are in general very fast, but they may not be well-suited to this work because they are unable to escape from local minima in a multi-extrema problem. Therefore, the high accuracy and fast speed is the direct result of hybridization of global and local optimizers.

We have used the hybrid GA-CG method in the current work. This algorithm is developed using MATLAB optimization functions. The optimization starts with the GA optimizer with a rough initial value and continues for several iterations. The population size used for the GA optimization is 60, the type of cross over function is "Scattered", the mutation function is "Adaptive feasible" and the number of generations is usually selected between 10-30. The results obtained by the GA optimizer are used as suitable initial values for the CG optimizer which is sensitive to the starting point. The number of iterations which provides the optimum result is usually 200-300.

Constraints applied to the design parameter (length and offset of slots) are originated from physical limitations (waveguide dimensions) and radiation characteristics (resonance length of slot). The values of lengths are constrained to the range

of (10 to 14mm) and offsets constrained to the range of (0.2 to 1.5mm).

The computation time for the two examples given in this paper is in the order of a few minutes, while optimization of same examples using optimizers in full-wave simulation softwares such as Ansoft HFSS takes several days. It should also be mentioned that achieving all of the design goals (array pattern synthesis and input matching) is a cumbersome task in full-wave simulation software.

III. RESULTS

For verification purpose, two SIW linear array antennas at the frequency of $f=10GHz$ are designed. SIW structure parameters and the normalized admittance of the isolated slot are given in section II. Width of the equivalent waveguide for the SIW is obtained $15.0536mm$.

First array is considered with seven slots and it is aimed to give a SLL of -20dB. This is done by setting an upper and lower limit for the side lobes at specific angles θ , so that the pattern stays within these limits. Consequently, the error function for the pattern synthesis is:

$$\begin{aligned} \mathcal{E}_{synthesis} = & W_4^{upper} \sum_{m=1}^M |S(\theta_m) - h_m^{upper}|^2 \\ & + W_4^{lower} \sum_{m=1}^M |S(\theta_m) - h_m^{lower}|^2, \quad (12) \end{aligned}$$

where, h_m^{upper} and h_m^{lower} are the upper and lower limits of SLL of the desired pattern, respectively and θ_m denotes an angle between 0 to 180 degree. Applying the Method of Least Squares to the mentioned array, results in $S_{11} = -11dB$ at $f=10GHz$. Comparing the results obtained by the MLS with full-wave simulations for several examples of linear slot array, shows that setting the desired input admittance as $Y_{in}=0.7+j0.3$ (instead of ideal value of $Y_{in}=1+j0$) in the error function, results in better impedance matching. The need for such an adjustment in MLS design goal is mainly due to two factors; the approximations in the Elliott's design formulas (low height of waveguide) and in making the SIW equivalent to a conventional metallic waveguide. It should be noted that the value of Y_{in} stated above, is suitable for the design of almost every antenna array of this type. The obtained slots parameters (Fig. 4) are shown in Table 1.

Comparing the results obtained by MLS with those from HFSS and CST simulation (Fig. 5) shows a good agreement.

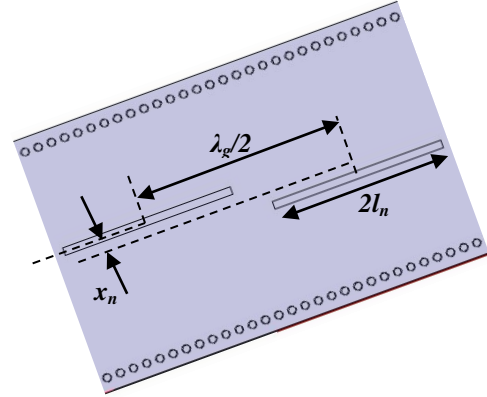


Fig. 4. Slot parameters.

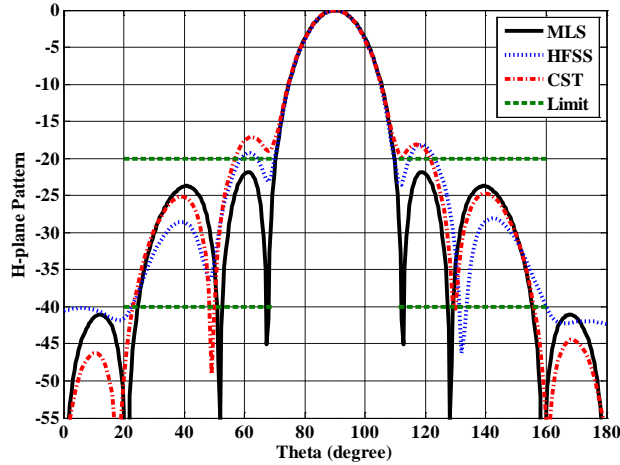
Second array is considered with fourteen elements to achieve a high gain. It is known that Dolph-Chebyshev's method for pattern synthesis, provides a minimum beamwidth for a given sidelobe level, making it a suitable candidate for directive beam pattern design. Therefore, the error function for pattern synthesis is:

$$\mathcal{E}_{synthesis} = W_4 |S(\theta) - S_{dolphi}(\theta)|, \quad (13)$$

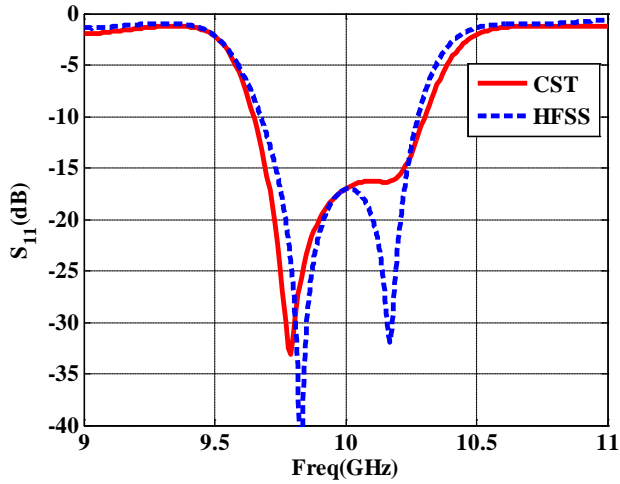
where, S_{dolphi} is Dolph-Chebyshev's pattern. In this example, the element factor is not included in the error function of pattern synthesis to simplify the optimization procedure. However it is considered in the final MLS pattern. The obtained slots parameters from MLS are shown in Table 2 and the results are shown in Fig. 6. A good agreement is seen between MLS and the simulation results.

Table 1: MLS results

Seven Elements Linear Array							
n	$ x_n $	$2\ell_n$	$ V_n^s/V_1^s $	n	$ x_n $	$2\ell_n$	$ V_n^s/V_1^s $
1	0.581	11.070	1.000	5	0.823	11.203	1.683
2	0.752	11.042	1.276	6	0.752	11.042	1.276
3	0.823	11.203	1.683	7	0.581	11.070	1.000
4	0.879	11.226	1.836				

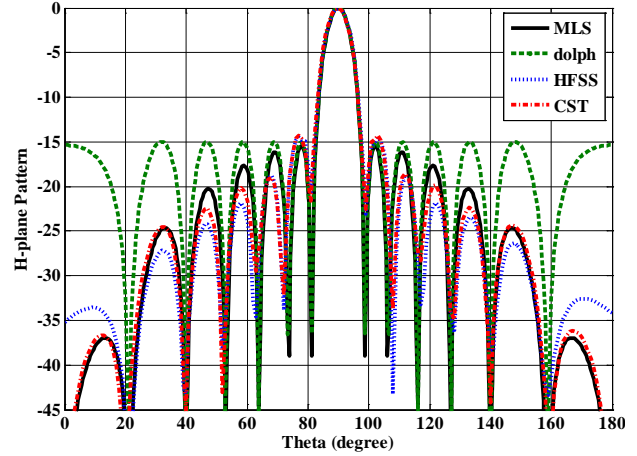


(a)

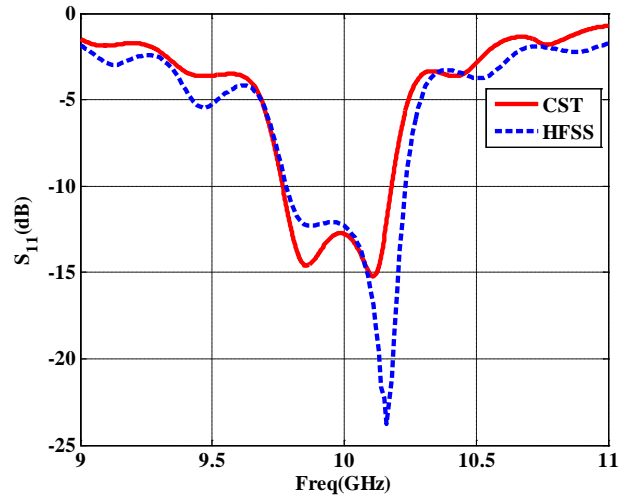


(b)

Fig. 5. A seven element linear array, (a) H-plane pattern, (b) S_{11} (dB).



(a)



(b)

Fig. 6. A fourteen element linear array, (a) H-plane pattern, (b) S_{11} (dB).

Table 2: MLS results

Fourteen Elements Linear Array							
n	$ x_n $	$2\ell_n$	$ V_n^s/V_1^s $	n	$ x_n $	$2\ell_n$	$ V_n^s/V_1^s $
1	0.475	11.359	1.000	8	0.611	11.068	0.686
2	0.664	10.794	0.440	9	0.609	11.055	0.661
3	0.555	11.000	0.509	10	0.592	11.049	0.630
4	0.585	11.028	0.582	11	0.586	11.018	0.570
5	0.594	11.044	0.626	12	0.552	11.006	0.513
6	0.608	11.062	0.669	13	0.666	10.786	0.435
7	0.613	11.064	0.682	14	0.474	11.360	1.000

VI. CONCLUSION

A very effective method is presented for the design of SIW slot array antennas. The proposed method has been applied to the design of seven and fourteen slot array antennas with specified radiation patterns. The good agreement between the MLS design results and those are obtained by HFSS and CST simulation software verifies the accuracy of the proposed method. The hybrid optimization method of GA-CG has the advantage of giving results in a very short computation time.

REFERENCES

[1] H. Oraizi and M. T. Noghani, "Design and Optimization of Waveguide-Fed Centered Inclined

Slot Arrays," *IEEE Trans. Antennas Propagat.*, vol. 57, pp. 3991-3995, 2009.

- [2] R. A. Gilbert, "Waveguide Slot Antenna Arrays," in *Antenna Engineering Handbook*, McGraw-Hill, New York, 2007.
- [3] R. S. Elliott and L. A. Kurtz, "The Design of Small Slot Arrays," *IEEE Trans. Antennas Propagat.*, vol. 26, pp. 214-219, Mar. 1978.
- [4] R. S. Elliott, "An Improved Design Procedure for Small Arrays of Shunt Slots," *IEEE Trans. Antennas Propagat.*, vol. 31, pp. 48-53, Jan. 1983.
- [5] R. S. Elliott and W. R. O'Loughlin, "The Design of Slot Arrays Including Internal Mutual Coupling," *IEEE Trans. Antennas Propagat.*, vol. 34, pp. 1149-1154, 1986.
- [6] F. Xu and K. Wu, "Guided-Wave and Leakage Characteristics of Substrate Integrated Waveguide," *IEEE Trans. Microw. Theory Tech.*, vol. 53, pp. 66-73, Jun. 2005.
- [7] D. Deslandes and K. Wu, "Accurate Modeling, Wave Mechanisms, and Design Considerations of a Substrate Integrated Waveguide," *IEEE Trans. Microw. Theory Tech.*, vol. 54, pp. 2516-2526, Jun. 2006.
- [8] L. Yan, W. Hong, K. Wu, and T. J. Cui, "Investigations on the Propagation Characteristics of the Substrate Integrated Waveguide Based on the Method of Lines," *Proc. Inst. Elect. Eng. Microw. Antennas Propagat.*, vol. 152, pp. 35-42, Feb. 2005.
- [9] L. Yan, W. Hong, G. Hua, J. Chen, K. Wu, and T. J. Cui, "Simulation and Experiment on SIW Slot Array Antennas," *IEEE Microwave And Wireless Components Letters*, vol. 14, no. 9, Sep. 2004.
- [10] F. Xu, W. Hong, P. Chen, and K. Wu, "Design and Implementation of Low Sidelobe Substrate Integrated Waveguide Longitudinal Slot Array Antennas," *IET Microwaves, Antennas & Propagation*, vol. 3, pp. 790-797, 2009.



Seyed Ehsan Hosseininejad was born in Semnan, Iran in 1987. He received the B.S. degree in Electrical and Electronic Engineering from Semnan University in 2009. He is currently working towards the M.S. degree at the Iran University of Science and Technology (IUST), Tehran. His current areas of research interests include microstrip antennas, slot array antennas, plasmonics, and nanoantennas.



Nader Komjani received his B.Sc., M.Sc., and Ph.D. degree all in Electrical Engineering from Iran University of Science and Technology, Tehran, Iran, in 1988 and 1991, and 2000, respectively. He is currently the associate professor with Iran University of Science and Technology. His research interests are in the areas of UWB and multiband microstrip antennas, numerical methods in electromagnetic, phased array antennas and passive and active microwave systems.



Homayoon Oraizi received B.E.E. degree from American University of Beirut, Lebanon, in 1967, M.Sc. and Ph.D. degrees in Electrical Engineering from Syracuse University, Syracuse, NY, in 1969 and 1973, respectively. In 1985, he joined the Department of Electrical Engineering, Iran University of Science and Technology, Tehran, Iran, where he is a Full Professor of electromagnetic engineering. He has authored or coauthored over 170 papers in international journals and conferences. Dr. Oraizi is a Fellow of Electromagnetic Academy, a fellow of Japan Society for the Promotion of Science and a senior member of IEEE.



Mahmoud T. Noghani was born in Tehran, Iran in 1982. He received the B.S. degree in Electrical and Electronic Engineering from Sharif University of Technology in 2005, and the M.S. degree in Electrical and Communication Engineering from Iran University of Science and Technology (IUST) in 2008. He is currently working towards the Ph.D. degree at the IUST. His research interests are RF and Microwave passive structures, Antennas and EM wave propagation and Photonic and Nanophotonic devices and components design.

Application of ANNs in Evaluation of Microwave Pyramidal Absorber Performance

M. Agatonović, Z. Marinković, and V. Marković

Department of Telecommunications
Faculty of Electronic Engineering, University of Niš, 18 000 Niš, Serbia
marija.agatonovic@elfak.ni.ac.rs, zlatica.marinkovic@elfak.ni.ac.rs,
vera.markovic@elfak.ni.ac.rs

Abstract — To evaluate the overall anechoic chamber performance it is necessary to determine reflectivity of the absorbers. As manufacturer specifications usually give only information about frequency dependent reflection coefficient at normal incidence of EM waves, a time-consuming electromagnetic analysis is necessary to calculate the reflection coefficient at off-normal incident angles. In this paper, an efficient alternative approach to obtain the reflection coefficient at off-normal incidence is proposed. It is based on artificial neural networks trained to model the absorber reflectivity dependence on the frequency and incident angle of horizontally and vertically polarized electromagnetic waves. The model has been developed for pyramidal absorbers at low microwave frequencies (0.4 GHz–1 GHz).

Index Terms — Artificial neural networks, incident angle, microwave pyramidal absorber, reflectivity.

I. INTRODUCTION

The internal appearance of a radio frequency (RF) anechoic chamber, where measurements of antenna radiation patterns, electromagnetic compatibility (EMC) and radar cross section (RCS) are performed, is covered with a radiation absorber material (RAM). In an anechoic chamber, the transmitter is located at one end of the chamber and the receiver is located at the opposite end, called quiet zone or test region. Generally, electromagnetic waves in the chamber propagate in all directions. Reflections from the walls, floor and ceiling affect the complex wave front at the receiver. The total electromagnetic field in this

region is equal to the sum of the direct and reflected EM waves between the source of EM energy and the device under test. The RAM is specifically designed and shaped to absorb the incident RF radiation in the test region to avoid measurement errors. Various parameters that affect performance of a microwave absorber include shape, volume, dimensions, and material properties. Research in the field of radiation absorber material has been mostly focused on the development of absorbers with good performance in term of reflection at normal incidence of EM waves, reduced scattering in broad range of incident angles, greater bandwidth and reduced thickness [1-4]. The final objectives of such research have been to provide cost savings in the process of the construction of an anechoic chamber, and to improve its overall performance.

In the manufacturer specifications of a microwave pyramidal absorber, the most commonly used type of microwave absorbers, information about frequency dependent reflection coefficient at normal incidence of EM waves can be found. Absorber characteristics when incident angles deviate from normal are usually unknown. In practice, microwave absorber should offer favorable properties at off-normal incidence as well. Since these data are not available due to practical limitations of the test fixtures to measure the RF absorber reflectivity, simulations employing EM solvers are successfully used to determine the absorber performance [1-2]. A potential disadvantage of EM simulations is that they are computationally intensive for large structures such as a microwave pyramidal absorber used at frequencies below 1 GHz. Besides EM

models, a number of numerical models are developed to optimize absorber dimensions and material parameters [3, 5-11].

In this work, we suggest an application of artificial neural networks (ANNs) in the evaluation of microwave pyramidal absorber performance. ANNs are very convenient as a modeling tool since they have the ability to learn from the presented data, and therefore, they are especially useful for problems not fully mathematically described. In other words, ANNs are able to map dependence between two datasets. The learning process is an optimization procedure through which parameters of the ANN are optimized in order to have the ANN outputs as close as possible to the desired target values. Compared to standard data fitting/interpolation technique, e.g. polynomial interpolation, ANNs have greater capability of fitting a nonlinear and complex dependency, especially in the cases where increasing the order of the used polynomials does not change fitting accuracy. Owing to the mentioned advantages ANNs have been efficiently applied in a wide range of modeling problems. There are many publications reporting the results of applications of the neural networks in the microwave area, referring to both passive and active microwave devices and circuits [13-21]. The idea presented in this paper is to replace cumbersome EM calculations requested for determining the reflectivity by an efficient neural model, i.e. to train an ANN to model reflectivity of an absorber against polarization, frequency, and incident angle. As it is shown in the paper, the developed ANN models are able to give accurate results providing significant time savings. The paper is organized as follows. In Sections II and III, the theoretical background on microwave absorbers as well as on artificial neural networks is given. The proposed approach is described in Section IV, followed by the numerical results given in Section V. The last section contains the concluding remarks.

II. MICROWAVE PYRAMIDAL ABSORBERS

Depending on the electromagnetic absorbing mechanism, dielectric and magnetic absorbers are commonly used for lining the internal appearance of the anechoic chamber. Hybrid absorbers, that

combine both the magnetic and dielectric absorbers, can also be found in some anechoic chambers.

Dielectric absorbers are usually made of carbon impregnated polyurethane foam. Generally, the primary loss mechanism is the conversion of RF energy into heat, although most radiation absorber materials do not get very warm when they are illuminated by EM waves [4]. Performance of dielectric absorbers is a function of frequency-dependent electrical characteristics of the material such as relative permittivity (ϵ_r) and loss tangent ($\tan \delta$). In reality, losses in the dielectric are directly determined by the concentration of carbon particles in the material. Microwave absorbers using dielectric losses are electrically conductive in most cases. Dielectric absorbers are usually shaped into pyramids and wedges [1-11]. A number of such elements are fastened to the square base made of the same absorbing material. Elements are typically bounded to the metallic surfaces of the internal chamber walls, mostly by the adhesive glue of low relative dielectric constant.

The cross-section of a pyramidal absorber linearly increases towards the chamber wall having a function of impedance transformer. The propagation of an EM wave with normal incidence to the wall can be modeled as propagation across an equivalent transmission line of characteristic impedance of 377Ω (free-space impedance). In order to achieve the optimal matching condition, the transmission line is loaded with the same impedance (metal wall covered by the absorber).

The reflectivity behavior versus frequency depends on the height of a particular pyramid, with larger pieces giving better absorption performance at lower frequencies. Consequently, the selection of pyramidal absorber for lining the internal appearance of the anechoic chamber varies depending on the lowest operating frequency. For specific applications like EMC measurements, or applications with weight restrictions, pyramidal absorbers employing high pyramids are required [6-7]. Generally, a pyramidal absorber has good performance in attenuating the reflections of electromagnetic waves when the height of pyramids is greater than the wavelength of EM waves. When an EM wave illuminates the absorber surface, it can be

reflected, scattered at pyramid tips, or absorbed. At the lower frequencies, when the pyramids height becomes smaller compared to the wavelength of EM waves, performance of the pyramidal absorber rapidly deteriorates. Since the absorber dissipates only a part of the incident EM wave energy, reflections from metal walls are significantly higher than the absorption and scattering at pyramid tips.

If the geometry of an anechoic chamber is designed in such a way that the EM wave from the transmitter reaches the receiver after several reflections from the walls, floor and ceiling, the EM wave is attenuated enough, and does not affect the measurement accuracy.

To determine the reflection coefficient of a microwave pyramidal absorber sample using a 3D EM solver, in the first step, the radar cross section (RCS) of reference metallic reflector must be calculated. The RCS is a far field parameter that determines the scattering properties of a specific target. It represents a complex parameter depending on the incident wave, i.e. depending on the polarization, propagation angle, operation frequency of the incident wave and the target itself (geometry, material characteristics). A perfect electric rectangular conductor has theoretical RCS value that can be expressed as a function of the operating frequency as follows

$$\sigma = \frac{4\pi L^2 W^2}{\lambda^2}, \quad (1)$$

where σ is radar cross section (m^2), L is the length of metal reflector (m), W is the width of metal reflector (m), λ is the wavelength of the electromagnetic wave (m). Normalized value in dB can be written as

$$RCS = 10 \log \left(\frac{\sigma}{\lambda^2} \right), \quad (2)$$

and represents a reference value when the reflection of the pyramidal absorber is determined. After the RCS of a metallic reflector is obtained, a microwave absorber in the form of an array of pyramids is placed on the metal surface. RCS of the structure is then calculated. The reflection coefficient of the pyramidal absorber is determined as the difference between the RCS values of metallic reference and pyramidal absorber sample. In the case of normal incidence of the EM wave on the absorber surface, the RCS

is calculated in the same direction, normal to the plane in which the metallic reflector is placed. However, if the incident angle of EM wave is off-normal (e.g. θ), the RCS is taken from the direction $-\theta$ [2].

III. ARTIFICIAL NEURAL NETWORKS

For the purpose of developing a neural model of a microwave pyramidal absorber standard multilayer ANNs can be exploited. A multilayer perceptron (MLP) neural network is shown in Fig. 1 [13]. An MLP ANN is built up of a number of elementary processing units, called neurons, which is organized into layers (an input layer, an output layer as well as several hidden layers). Every neuron in each layer is connected to all neurons from the adjacent layer but no connections are permitted between the neurons belonging to the same layer. Each neuron is characterized by an activation function and its bias, and each connection between two neurons by a weight factor.

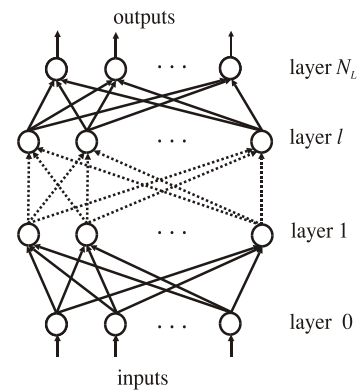


Fig. 1. Multilayer perceptron neural network.

Input signals propagate gradually from the input layer through the hidden layers up to the output layer. The output of the l -th layer can be written as

$$Y_l = F(W_l Y_{l-1} + B_l), \quad (3)$$

where Y_l and Y_{l-1} are outputs of l -th and $(l-1)$ -th layer, respectively, W_l is a weight matrix between $(l-1)$ -th and l -th layer and B_l is a bias matrix between $(l-1)$ -th and l -th layer. Function F is the activation function of each neuron and, it is linear for input and output layer and sigmoid (tan-sig in the particular case) for hidden layers [13]. With

one or two hidden layers, ANNs can approximate virtually any input-output mapping.

A neural network is trained to learn relationship between sets of input-output data that are characteristics of the structure under consideration. The most known training procedure is the back propagation algorithm and its modifications such as quasy-Newton or Levenberg-Marquardt algorithms [13]. The back propagation algorithm can be described shortly as follows: after the input vectors are presented to the input neurons, the output vectors are computed. These output vectors are then compared with desired values and errors are determined. Error derivatives are then calculated and summed up for each weight and bias until whole training set has been presented to the network. The error derivatives are used to update the weights and biases for neurons in the model. The training process continues until errors are lower than the prescribed values or until the maximum number of epochs (epoch - the whole training set processing) is reached. Once trained, the network provides fast response for different input vectors, even for those not included in the training set (generalization capability, which is the most important feature of ANNs).

Having in mind that the most sensitive region of the typical neuron transfer functions is in the narrow range $[-1, 1]$ in the case of the tan-sigmoid function), to avoid saturation of neurons the input and output data are scaled from the original range to the normalized range $[-1, 1]$. Therefore the ANN response is normalized and has to be de-normalized to obtain the final output values. Normalization and de-normalization are done as described in [13].

To determine accuracy of an ANN model, average test error (ATE [%]), worst-case error (WCE [%]), and correlation coefficient, r , between the reference and the data simulated by the ANN are calculated, [13].

The Pearson product-moment correlation coefficient r is defined by:

$$r = \frac{\sum (x_i - \bar{x})(y_i - \bar{y})}{\sqrt{\sum (x_i - \bar{x})^2 \sum (y_i - \bar{y})^2}}, \quad (4)$$

where x_i represents the reference value, y_i is the ANN computed value, \bar{x} is the reference sample

mean, and \bar{y} is the ANN sample mean. The correlation coefficient is an indicator how the modeled values match the reference ones. If a correlation coefficient is close to one that means that MLP ANN has an excellent predictive ability, whereas a coefficient close to zero indicates poor performance of the network.

Since computing of the trained ANN response can be done practically instantaneously due to performing only basic mathematical operations and calculating elementary functions, neural models are much faster than the computatively intensive and time-consuming EM models. This ability qualifies them as very suitable to be applied in the area of modeling of different EM structures, as it is shown in this paper for the case of the microwave absorbers modeling.

IV. PROPOSED MODEL

As mentioned in Section II, determination of the reflectivity of microwave pyramidal absorbers in 3D EM solvers takes a lot of time. In order to make the time needed for the reflectivity calculation shorter, here a microwave pyramidal absorber model based on ANNs is proposed.

It consists of two ANNs trained to model dependence of the absorber reflection coefficient on the frequency and incident angle of the horizontally and vertically polarized EM wave illuminating the absorber. According to this, each ANN has two neurons in the input layer corresponding to the frequency and the incident angle and only one neuron in the output layer corresponding to the reflectivity of the modeled absorber at the desired polarization, Fig. 2.

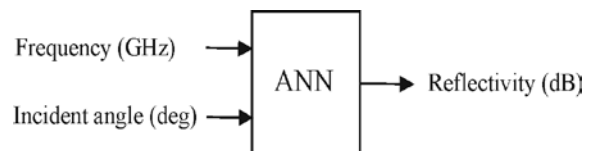


Fig. 2. Proposed ANN model.

The data used to train the ANN are values of the reflection coefficient obtained in a 3D EM solver for certain number of input combinations. Since the number of hidden neurons cannot be a priori known, it should be determined during the training process. Namely, ANNs with a different number of hidden neurons are trained and

compared, and according to the test statistics, the best structure for the considered case is found. After the completed training and evaluation, the trained ANN can be used for fast calculating the reflectivity of the modeled absorber without using a 3D EM solver. It is important to note that reflectivity can be determined accurately for any input value belonging to the same range as the inputs used in the training process.

V. NUMERICAL RESULTS

The proposed model has been developed for an absorber sample of 6x6 pyramids aimed for use in an anechoic chamber at low microwave frequencies (0.4 GHz – 1 GHz).

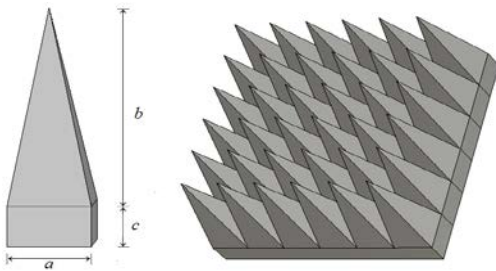
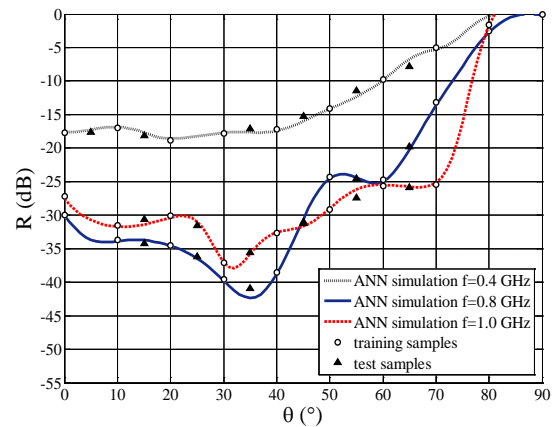


Fig. 3. Analyzed sample of the microwave pyramidal absorber ($a=330$ mm, $b=900$ mm, $c=210$ mm).

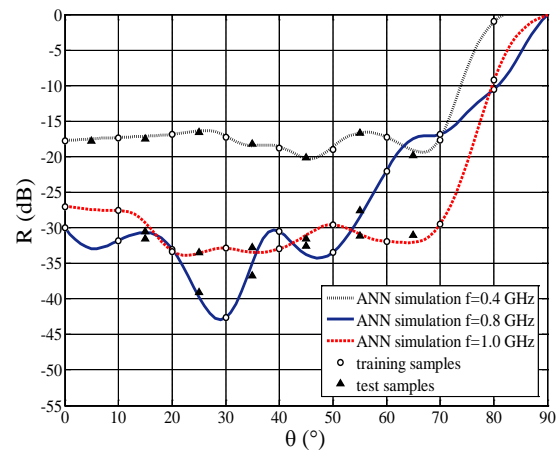
It is supposed that the absorber is made of carbon impregnated polyurethane foam whose complex relative permittivity is frequency dependent. At the frequency of 0.4 GHz it has a value of $1.28 - j 0.16$ which gradually decreases to $1.1 - j 0.1$ at 1 GHz [3]. The training and test data for ANN models are obtained using the full-wave electromagnetic solver WIPL-D [22]. ANNs for both horizontally and vertically polarized EM illuminating waves have been developed and validated independently. In both cases, the training data consisted of the training samples referring to the incidence angles from 0° to 90° , in steps of 10° . For each angle, the absorber reflection coefficient has been determined by EM simulations in the frequency range of 0.4 GHz - 1 GHz with a step of 0.1 GHz. Further, ANNs with a different number of hidden layers have been trained and tested. After intensive experimentation, it has been found that the following ANNs provided the best test statistics: for vertically polarized EM waves an ANN having

two hidden layers with 15 neurons in each of them, and for horizontally polarized EM waves an ANN with two hidden layers having 20 neurons each. For the chosen ANNs, the Pearson product-moment correlation coefficient calculated for the case of the simulation of the reflectivity for the training inputs has value of 0.9999 for vertically polarized EM waves, and 0.9998 for horizontally polarized EM waves.

To illustrate accuracy of the proposed model, i.e. to show how much the ANNs have learned the training data and how much are capable to generalize, in Figs. 4 and 5 there is the reflectivity plotted against the incidence angle. Figure 4 refers to the training frequencies (0.4GHz, 0.8 GHz, and 1 GHz), whereas Fig. 5 refers to the frequency not used for the training (0.85 GHz).



(a)



(b)

Fig. 4. Reflectivity performance of the microwave pyramidal absorber at training frequencies for (a) vertically and (b) horizontally polarized EM waves.

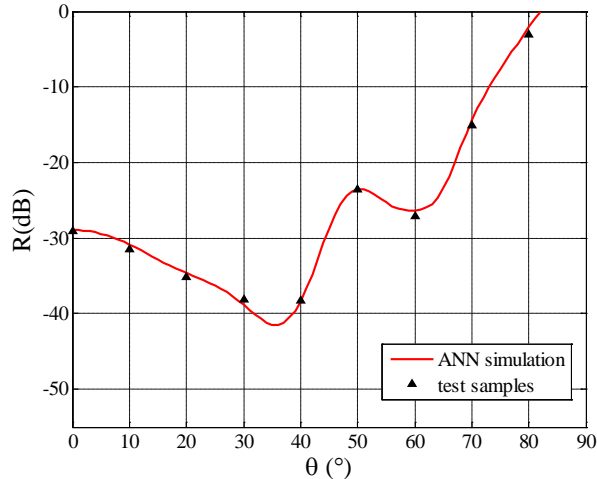


Fig. 5. Reflectivity performance of the microwave pyramidal absorber at test frequency $f=0.85$ GHz for vertically polarized EM waves.

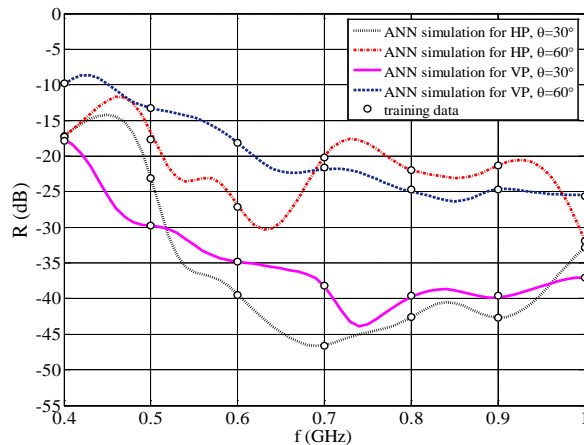


Fig. 6. Reflectivity performance of the microwave pyramidal absorber for different incident angles of EM waves.

In addition, the reflectivity versus frequency for both polarizations and different incidence angles is plotted in Fig. 6.

Lines represent the reflectivity simulated by the ANN models, whereas the symbols refer to the reference data obtained by the EM solver. Circles correspond to the training values of the incidence angles and triangles correspond to the values of the incident angle not used for the network training.

A good agreement of the simulated and the reference values for both training and test samples confirm the ability of the ANN model to simulate accurately the absorber reflectivity for different inputs. As an additional illustration, in order to

compare the reflectivity simulated by the EM solver with the one obtained by the ANN model, in Fig. 7. There are reflectivity values used for the training purposes calculated by the EM solver and the reflection coefficient simulated by the ANN model in steps of 0.01 GHz for the frequency, and 1° for the incident angle. The plots confirm that the ANN model calculates the reflectivity with the same accuracy as the EM solver.

Using the ANN model instead of the EM solver significant time savings can be provided. For example, to calculate the reflectivity for one input combination (one frequency point at a fixed incident angle) in WIPL-D, the simulation time was 0.5 minutes at 0.4 GHz, and 25 minutes at 1 GHz. Simulations were performed at a Pentium dual-core computer (2 GHz CPU with 4GB RAM memory). With further increasing of the operating frequency, the EM solver needs more time to calculate reflectivity since the structure of the absorber sample becomes electrically larger. On the other side, ANN trained to predict the reflectivity of the absorber can determine the reflectivity for a given input combination in a matter of second, independently of the operating frequency.

VI. CONCLUSION

In this paper, modeling of microwave pyramidal absorber utilizing artificial neural networks (ANNs) is reported. An ANN model has been developed to estimate absorber performance at different incident angles of electromagnetic waves and operating frequencies, for vertical as well as horizontal polarization. For model development, the reflectivity calculated by the EM solver has been used. As illustrated, the reflectivity calculated by the ANN model is very close to the reference reflectivity obtained by the EM solver. Once trained ANN model calculates the reflectivity directly, outside the EM solver, not by subtracting RCSs of the metallic reflector and the pyramidal absorber sample as it is usually done in 3D EM solvers, consequently saving the simulation time while maintaining the accuracy as illustrated in the presented example.

The ANN model simulates reflectivity in a matter of seconds independently of the operating frequency, which is its advantage over the EM solvers where simulation time depends on the frequency and is order of tens of minutes.

Therefore, a new design methodology that is both accurate and fast at the same time can be an alternative solution to time-consuming simulations using full-wave electromagnetic solvers.

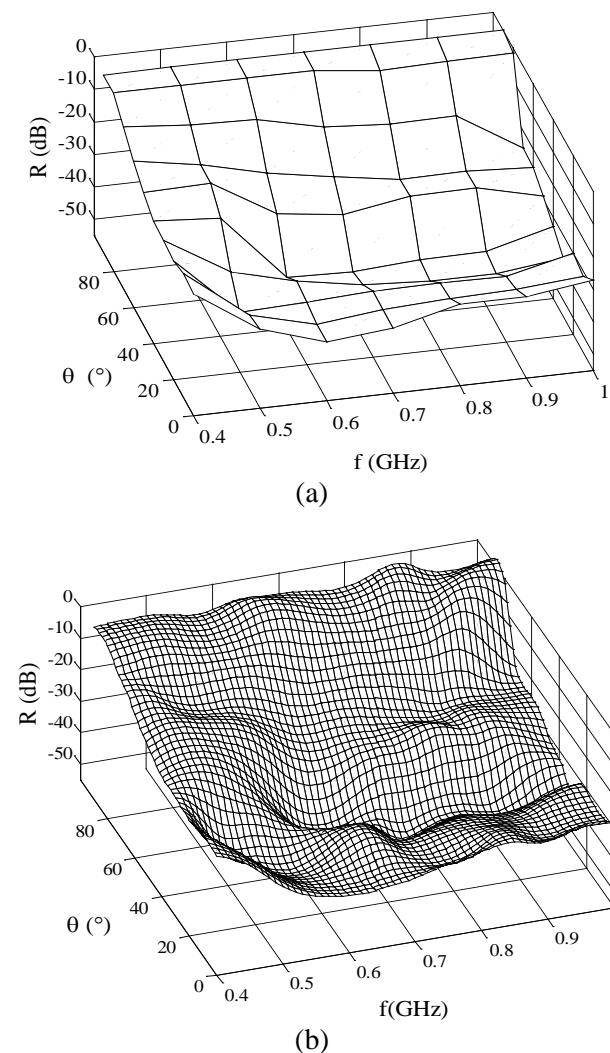


Fig. 7. Reflectivity performance of the microwave pyramidal absorber (a) training samples calculated by the full-wave EM solver (b) simulated by the ANN model.

ACKNOWLEDGEMENT

The work was supported by the project III-43012 of the Serbian Ministry of Education and Science.

REFERENCES

- [1] B. K. Chung and H. T. Chuah, "Modeling of RF Absorber for Application in the Design of Anechoic Chamber," *Progress in*

Electromagnetics Research (PIER), vol. 43, pp. 273-285, 2003.

- [2] B. B. Janić and B. M. Kolundžija, "RF Absorber Reflectivity Evaluation using RSC Calculation," *IEEE AP-S International Symposium 2007*, Honolulu, Hawaii, USA, pp. 6043-6046, June 2007.
- [3] A. Khajepour and S. A. Mirtaheri "Analysis of Pyramid EM Wave Absorber by FDTD Method and Comparing with Capacitance and Homogenization Methods," *PIERS*, vol. 3, pp. 123-131, 2008.
- [4] J. T. Gear, "Microwave Absorbers Manage Military Electronics RF Interference," *Defense Electronics*, pp. 6-9, 2004.
- [5] H. Anzai, M. Saikawa, Y. Naito, and T. Mizumoto, "The Equivalent Representation of Pyramidal Absorbers and its Application to the Analysis of Electromagnetic Wave Absorber's Characteristics," *Proceedings of the IEEE International Symposium on EMC*, Atlanta, USA, pp. 563-567, 1995.
- [6] C. L. Holloway, P. M. McKenna, R. A. Dalke, R. A. Perala, and C. L. Devor, "Time-Domain Modeling, Characterization, and Measurements of Anechoic and Semi-Anechoic Electromagnetic Test Chambers," *IEEE Trans. on EMC*, vol. 44, no. 1, pp. 102-118, 2002.
- [7] E. Kuester and C. A. Holloway, "A Low-Frequency Model for Wedge or Pyramid Absorber Arrays-I: Theory," *IEEE Trans. on EMC*, vol. 36, no. 4, pp. 300-307, 1994.
- [8] S. Kent and M. Kartal, "Dielectric Absorber Design for Wide Band-Wide Oblique Incidence Angle using Genetic Algorithm," *Int. J. Electron. Commun. (AEÜ)*, vol. 61, pp. 398-404, 2007.
- [9] E. Michielssen, J. M. Sajer, S. Ranjithan, and R. Mittra, "Design of Lightweight, Broad-Band Microwave Absorbers using Genetic Algorithms," *IEEE Trans. on MTT*, vol. 41, no. 6/7, pp. 1024-1031, 1993.
- [10] S. Kent and M. Kartal, "Genetic Algorithm Approach on Pyramidal Dielectric Absorbers," *Int. J. of RF and Microwave Computer-Aided Engineering*, vol. 18, no. 3, pp. 286-294, 2008.
- [11] T. Kaufmann, K. Sankaran, and C. Fumeaux, "A Review of Perfectly Matched Absorbers for the Finite-Volume Time-Domain Method," *Applied Computational Electromagnetic Society (ACES) Journal*, vol. 23 no. 3, pp. 184-192, 2008.
- [12] E. A. Hashish and S. M. Eid, "Design of Wideband Planar Absorbers using Composite Materials," *Applied Computational Electromagnetic Society (ACES) Journal*, vol. 24, no. 4, pp. 413-418, 2009.

- [13] Q. J. Zhang and K. C. Gupta, *Neural Networks for RF and Microwave Design*, Artech House, Inc. Norwood, MA, USA, 2000.
- [14] C. Christodoulou and M. Gerogiopoulos, *Applications of Neural Networks in Electromagnetics*, Artech House, Inc. Norwood, MA, USA, 2000.
- [15] S. S. Gultekin, K. Guney, and S. Sagiroglu, "Neural Networks for the Calculation of Bandwidth of Rectangular Microstrip Antennas," *Applied Computational Electromagnetic Society (ACES) Journal*, vol. 18, no. 2, pp. 110-120, 2003.
- [16] J. E. Rayas-Sanchez, "EM-Based Optimization of Microwave Circuits using Artificial Neural Networks: The State-of-the-Art," *IEEE Trans. Microw. Theory Tech.*, vol. 52, no. 1, pp. 420-435, Jan. 2004.
- [17] V. Marković and Z. Marinković, "HEMT Noise Neural Model Based on Bias Conditions," *COMPEL*, Emerald, vol. 23, no. 2, pp. 426-435, 2004.
- [18] L. Zhang, Q. -J. Zhang, and J. Wood, "Statistical Neuro-Space Mapping Technique for Large-Signal Modeling of Nonlinear Devices," *IEEE Trans. on MTT*, vol. 56, no. 11, pp. 2453-2467, 2008.
- [19] R. Ghayoula, N. Fadlallah, A. Gharsallah, and M. Rammal, "Design, Modeling, and Synthesis of Radiation Pattern of Intelligent Antenna by Artificial Neural Networks," *Applied Computational Electromagnetic Society (ACES) Journal*, vol. 23, no. 4, pp. 336-344, 2008.
- [20] H. Kabir, Y. Cao, and Q. Zhang, "Advances of Neural Network Modeling Methods for RF/Microwave Applications," *Applied Computational Electromagnetic Society (ACES) Journal*, vol. 25, no. 5, pp. 423-432, 2010.
- [21] Z. Marinković, G. Crupi, A. Caddemi, and V. Marković, "Microwave FinFET Modeling Based on Artificial Neural Networks Including Lossy Silicon Substrate," *Microelectronic Engineering*, vol. 88, no. 10, pp. 3158-3163, 2011.
- [22] WIPL-D Pro v7.1, "*Software and User's Manual*," WIPL-D d.o.o., Belgrade, 2009.



Marija Agatonović received a Dipl.-Ing degree in Electrical Engineering in 2006 from the University of Niš, Faculty of Electronic Engineering, Serbia. She is a Ph.D. student at the University of Niš and a scholarship holder of the Serbian Ministry of Education and Science. Her research areas are artificial neural networks and their application in electromagnetics.



Zlatica Marinković received the Dipl.-Ing. degree in Electrical Engineering from the University of Niš, Faculty of Electronic Engineering, Serbia in 1999, and the M.Sc. and Ph.D. degrees from the same University in 2003 and 2007, respectively. She is a Teaching and Research Assistant with the University of Niš, Faculty of Electronic Engineering, Serbia. Her research areas are: microwave electronics and artificial neural networks and their application in the field of microwaves.

She serves as the Secretary of IEEE MTT-S Chapter of Serbia and Montenegro and is the editor-in-chief of the journal "Microwave Review".



Vera Marković received a Dipl.-Ing degree in Electrical Engineering in 1980, the M.Sc. degree in 1985 and Ph.D. degree in 1992, all from the University of Nis, Faculty of Electronic Engineering. Her main research areas include neural network modeling of microwave devices for wireless communications, the investigation of biological effects of microwave radiation, etc.

She is currently working as a full professor at the Department of Telecommunications, University of Nis, Faculty of Electronic Engineering. She has published a monograph, two textbooks and about 250 scientific papers. She is vice chair of the IEEE Serbia & Montenegro Section.

Design of High Performance Dual Frequency Concentric Split Ring Square Element for Broadband Reflectarray Antenna

Siti H. Yusop¹, Norbahiah Misran^{1,2}, Mohammad T. Islam², and Muhammad Y. Ismail³

¹ Department of Electrical, Electronic and Systems Engineering
Faculty of Engineering and Built Environment
Universiti Kebangsaan Malaysia, Selangor, 43600 UKM Bangi, Malaysia
yuzai_angah@yahoo.com, bahiah@vlsi.eng.ukm.my

² Institute of Space Science (ANGKASA)
Universiti Kebangsaan Malaysia, Selangor, 43600, Malaysia
titareq@yahoo.com

³ Department of Communication Engineering
Faculty of Electrical and Electronics Engineering
Universiti Tun Hussein Onn Malaysia, Johor, 86400 Parit Raja, Malaysia
yusofi@uthm.edu.my

Abstract — An analysis of phase variation and phase range of concentric split ring square element for broadband reflectarray antenna is presented in this paper. This element is the combination of a splitted single square and ring element whereas the square element is the modification of the conventional annular ring in which, instead of using annul as the hole, this new idea presents a square as the hole in the ring. This will modifies the current distribution in the element which will then improve the performance of the bandwidth as the objective of this work. The physical interpretation of the elements is presented and variety of frequency responses pattern is described and analysed. The design procedure and critical parameters consist of phase range and phase slope (or variation) are also discussed. The proposed antenna element effectively covers two frequency operations (13.44 GHz and 18.36 GHz) in Ku-band range. Bandwidth broadening is achieved by introducing the ring square combination of element and the practical phase range is achieved through the use of RF35 (thickness = 1.524 mm) as the substrate. The new concept of split initiates to a wider bandwidth (up to 67.6%) for the

antenna and can applied to any two frequency operations of Ku-band applications.

Index Terms — Broader bandwidth, dual frequency, Ku-band, reflectarray antenna.

I. INTRODUCTION

Microstrip reflectarrays present an alternative to the conventional parabolic reflectors [1, 2]. As its name implies, a reflectarray antenna combines some of the best features of reflector and array antennas. In its basic form, a microstrip reflectarray consists of a flat array of microstrip patches or dipoles printed on a thin dielectric substrate. A feed antenna illuminates the array whose individual elements are designed to scatter the incident field with the proper phase required to form a planar phase surface in front of the aperture, as shown in Fig. 1. A large reflectarray antenna is made of thousands antenna elements printed on the flat surface and illuminated by a feed horn [3, 4,11].

A plane wavefront can be obtained by controlling the scattering properties of each element. The basic design procedure entails the use of phase-design curves. Various approaches

have been proposed in the past which include the use of variable size patches and identical patches with variable size stubs for obtaining the required phase shift [4, 5].

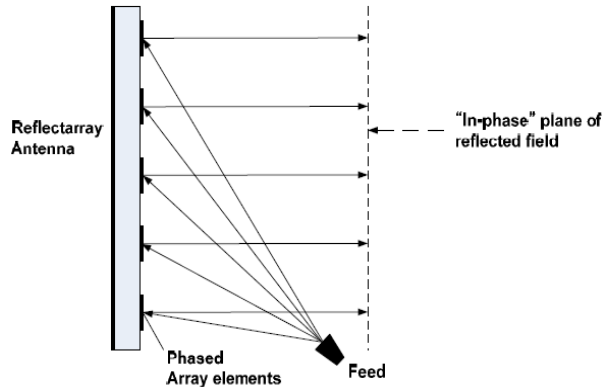


Fig. 1. Geometrical view of a reflectarray antenna.

The microstrip reflectarray has several applications due to its low-profile and small mass characteristic. One of the applications is that the flat reflectarray can be surface-mounted on a building side wall as a Ku-band Direct Broadcast Satellite (DBS) antenna. It also can be mounted on the rooftop of a large vehicle for satellite reception [4]. Recently, researchers have much interest in designing antenna which covers two frequency operations as been done in [6] and [7]. As stated in [6], the dual frequency covers X and Ka-band with the used of one layer substrate only while in [7], the dual frequency operation is achieved at 10 GHz and 18 GHz. This is evident that the dual frequency operation is possible for a simple design of one layer substrate reflectarray antenna element.

However, there is one distinct disadvantage associated with the reflectarray antenna which is its inherent characteristic of narrow bandwidth, which generally cannot exceed much beyond 10% depending on its element design, aperture size, focal length, etc [4]. For a printed microstrip reflectarray, its bandwidth is primarily limited by two factors which are the microstrip patch elements on the reflectarray surface and the differential spatial phase delay. This paper discussed the new concept of element to overcome the narrow bandwidth of the reflectarray antenna element.

II. ANTENNA STRUCTURE AND DESIGN

The element introduced in this paper namely concentric split ring square element is the combination of split ring and split square ring elements. RF35 is used as the substrate material with the dielectric constant of 3.54 and the loss tangent of 0.0018 at 1.9 GHz, while copper metal was used to simulate the designed element and the ground plane. The unit cell size is 10 mm x 10 mm. CST Microstripes software is used as the tool to analyze the phase variation graph. In CST Microstripes model, 0° phase reflection is used to define the resonance, whereas for a perfect conductor this is 180° relative to the incident wave.

In Fig. 2, R is the square ring element radius, O is the outer ring radius, I is the square length while g is the gap size for the split of the element. The nominal inner radius of the outer split ring element is 3.56 mm with the ring width is 0.4 mm and the radius of the split square ring is 3.06 mm which gives the ratio of R/O value equals to 0.86. The value of R and I is fixed at the same value to give the ratio of I/R equals to 1. Ideally the gap size should be smaller [8, 9] so that the resonant frequency is not increased but in this work, the gap size is limited to 0.28 mm due to the fabrication tolerances.

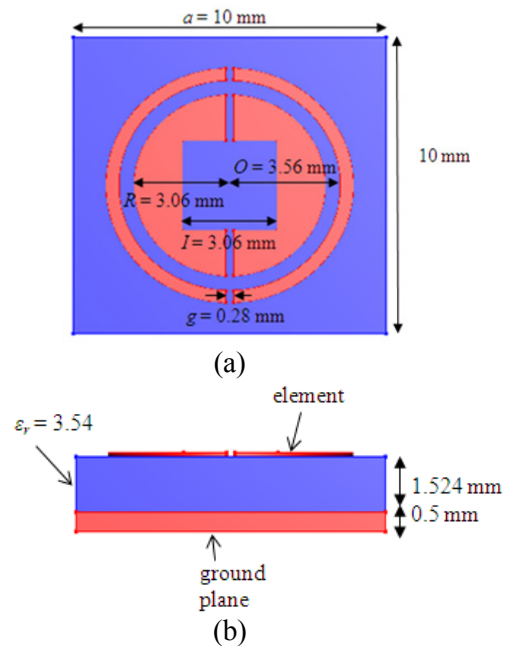


Fig. 2. The view of concentric split ring square reflectarray element (a) top-view (b) side-view.

The methodology used to establish a suitable design for the concentric split ring square reflectarray element is shown in Fig. 3. The first step of validation is to familiarize with the software and confirm the design procedure. Then, the basic annul of conventional ring element is replaced by the new potential concept of square hole. The combination of this new element with ring is to observe the operation of dual frequency resonance which is to reduce the cost of development two antennas for dual frequency operation.

From studies in [8, 9, and 10], the introduction of gap into a structure can affect the frequency response performance. In this work, the gap (or split) introduction into the elements then been analysed for bandwidth enhancement. Once the nominal size of element is determined, phase curve graph is plotted to observe its phase slope and phase range performance. As a final step of checking performance of the proposed reflectarray element, a unit cell was manufactured, and tested using the waveguide approach [4]. The side walls of the equivalent TEM waveguide are formed by a perfect magnetic conductor, while its bottom and top walls are composed of a perfect electric conductor using metal guides. Using the equivalent unit cell waveguide approach, phase of the reflected wave was calculated for the loaded waveguide.

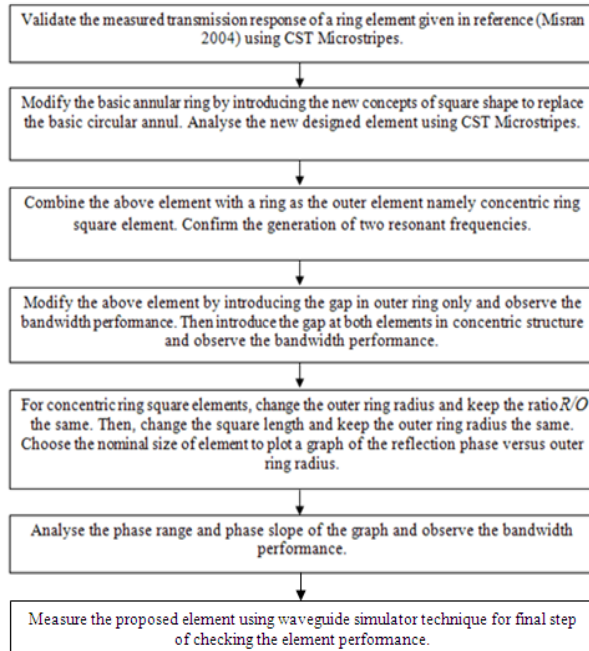


Fig. 3. Design methodology for concentric split ring square element.

Figure 4 shows the frequency response for concentric split ring square element with gaps and concentric solid ring square element without the gaps. The reflection phase shown in this figure are for vertical polarization where for the proposed element structure, vertical polarization will result in different reflection phase due to the introduction of vertical splits.

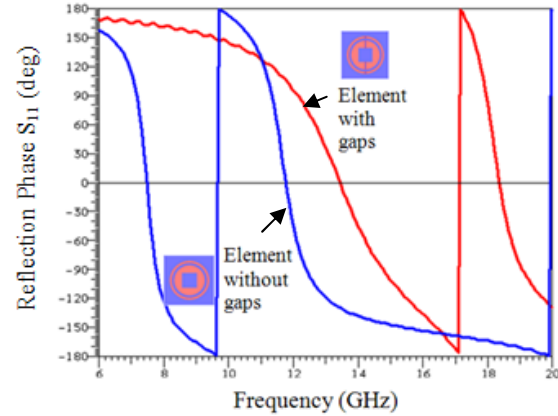


Fig. 4. Frequency response for two designed element.

The slope of the phase versus length curve is a measure of the bandwidth of the reflectarray, as a curve with a smaller slope will lead to less phase error when the electrical size of the elements change with frequency [1].

From Fig. 4, it is clearly shown that, for the first resonance, the gradient of the curve is largely decreased when gap is introduced in the design. This entails the bandwidth enhancement from 26.9% to 67.6%. While for the second resonance, the bandwidth is slightly improved from 19.8% to 20.3%.

The concentric ring square element produces two frequencies operation which covers Ku-band at 13.44 GHz and 18.36 GHz as shown in Fig. 5.

It is observed from Fig. 5 that at the first resonant frequency, the first element of splitted ring is strongly excited while at the second resonant frequency, the second element of splitted square is strongly excited. This evident that the outer ring is determining the first resonance, while the inner square ring determining the second resonance. From Fig. 5, it is also clearly shown that only quarter of element is simulated since we are using

the concept of symmetry that is available for the waveguide approach.

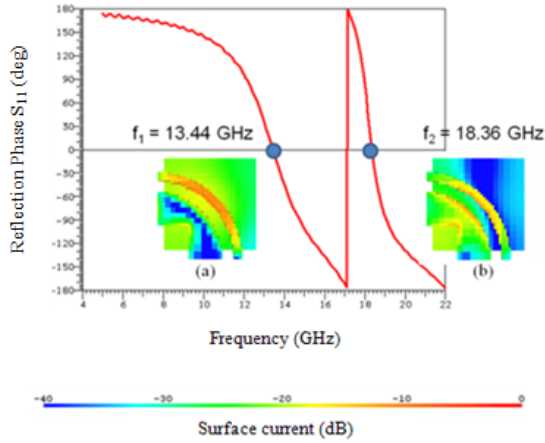


Fig. 5. Surface current distribution (a) at 13.44 GHz and (b) at 18.36 GHz for a grounded concentric split ring square reflectarray element.

For the experimental validation of the element analysis, the element is designed in an array environment for compromising TE₁₀ mode of waveguide simulator. The elements were inserted in the waveguide, where the ground plane with the apertures are in contact with the waveguide flange. Figure 6 shows the fabricated element with the developed waveguide simulator and the full set-up of measurement process.

From Fig. 6, it is shown that a waveguide simulator is used to measure the performance of the developed element. This waveguide is needed to be designed to compromise with the analysed resonant frequency of the designed element. The single port is used to get the scattering parameter, S₁₁.

III. RESULTS AND DISCUSSION

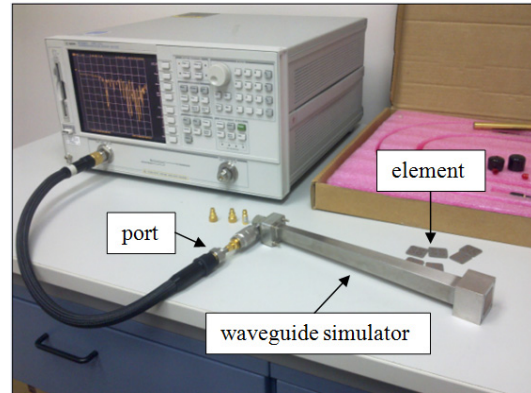
With the designed structure dimension given in Section 2, the simulated reflection phase versus outer ring radius is plotted and shown in Fig. 7 and Fig. 8 for first and second resonant frequency respectively. For Fig. 7 and 8, the ratio of $R/O = 0.86$, $I/R = 1$ and $g = 0.28$ mm is fixed for the phase studies.



(a)



(b)



(c)

Fig. 6. Measurement stage (a) waveguide simulator and (b) fabricated element inserted into the waveguide aperture (c) full set-up of measurement process.

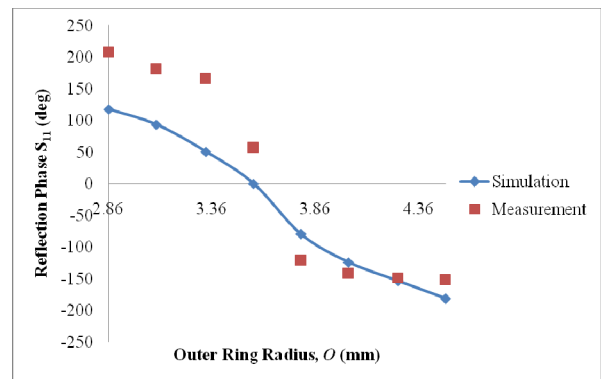


Fig. 7. Phase curve of concentric split ring square element at $f_1 = 13.44$ GHz.

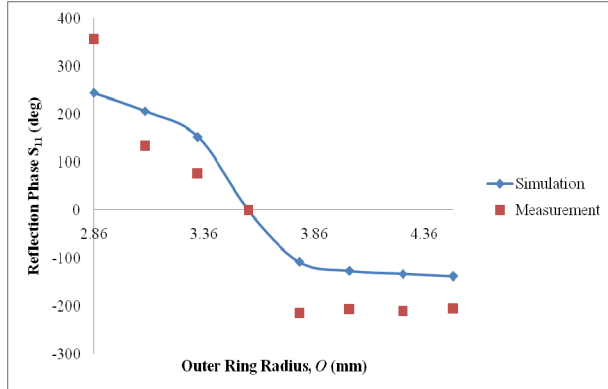


Fig. 8. Phase curve of concentric split ring square element at $f_2 = 18.36$ GHz.

The linear phase range simulated at the first resonance is 320° with the gradient of $0.15^\circ/\mu\text{m}$ and the phase range at the second resonance is 464° with the gradient of $0.33^\circ/\mu\text{m}$.

The bandwidth performance is 67.6% and 20.3% at the first and second resonance, respectively. The concentric element concept is used to achieve a dual frequency operation compared to the single element concept which gives only one resonant frequency.

Both simulation and measurement results show good agreement with slight differences due to minor fabrication error and some noise from signal reflected inside the waveguide simulator.

In the concentric element design, the critical feature of mutual coupling should be taken care of because the design which consist two elements using copper metal material can easily caused a short circuit. In this work, the gap between the first and second resonance element is fixed at 0.5 mm.

Table 1 shows the summary of comparison between concentric solid ring square element and concentric split ring square element. The introduction of split on the structure significantly affects the frequency response performance and improves the narrow bandwidth of the antenna element.

IV. CONCLUSION

A new design of reflectarray elements for the broadband dual frequency Ku-band application is proposed in this work which is the concentric split ring square element. By modifying the current distribution of the physical geometry of the basic concentric ring square element leads to a better

phase variation and bandwidth. This new design gives the good performance in bandwidth which is up to 67.6% and 20.3% in dual frequency operations. The phase range for the element is also in a good practical region which gives the value of 320° and 464° at both resonant frequencies respectively. The reflectarray antenna is easy to fabricate and low cost. These features are very useful for worldwide portability of communication applications.

Table 1: Comparison of two studied element shapes performance

Element Parameter	Concentric Solid Ring Square	Concentric Split Ring Square
Resonant Frequency (GHz)	$f_1 = 7.48$ $f_2 = 11.78$	$f_1 = 13.44$ $f_2 = 18.36$
Phase Range ($^\circ$)	at $f_1 = 249$ at $f_2 = 230$	at $f_1 = 320$ at $f_2 = 464$
Phase Slope ($^\circ/\mu\text{m}$)	at $f_1 = 0.54$ at $f_2 = 0.50$	at $f_1 = 0.15$ at $f_2 = 0.33$
Bandwidth Performance (%)	at $f_1 = 26.9$ at $f_2 = 19.8$	at $f_1 = 67.6$ at $f_2 = 20.3$

ACKNOWLEDGMENT

The authors would like to thank the MOSTI Secretariat, Ministry of Science, Technology and Innovation of Malaysia, Science fund: 01-01-02-SF0376, for sponsoring this work.

REFERENCES

- [1] D. M. Pozar, S. D. Targonski and H. D. Syrigos, "Design of Millimeter Wave Microstrip Reflectarrays," *IEEE Trans. Antennas Propag.*, vol. 45, no. 2, pp. 287-296, 1997.
- [2] H. Rajagopalan and Y. R. Samii, "Dielectric and Conductor Loss Quantification for Microstrip Reflectarray: Simulations and Measurements," *IEEE Trans. Antennas Propag.*, vol. 56, no. 4, pp. 1192-1196, 2008.
- [3] C. M. Han, "Dual-band Reflectarrays Using Microstrip Ring Elements and Their Applications with Various Feeding Arrangements," PhD Thesis, Office of Graduate Studies of Texas A&M University, Texas, 2006.
- [4] J. Huang and J. A. Encinar, *Reflectarray Antennas*, John Wiley and Sons, United States of America, 2008.

- [5] D. M. Pozar and T. A. Metzler, "Analysis of a Reflectarray Antenna Using Microstrip Patches of Variable Size," *Electron. Letter*, vol. 29, no. 8, pp. 657-658, 1993.
- [6] M. Zawadzki and J. Huang, "A Dual-Band Reflectarray for X- and Ka-Bands," *Progress in Electromagnetics Research Symposium (PIERS), Honolulu, Hawaii*, 2003.
- [7] A. M. Abbosh, "Design of Dual-band Microstrip Reflectarray Using Single Layer Multiresonance Double Cross Elements," *Progress In Electromagnetics Research Letters*, vol. 13, pp. 67-74, 2010.
- [8] N. Misran, "Design Optimisation of Ring Elements for Broadband Reflectarray Antennas," PhD Thesis, Faculty of Engineering, The Queen's University Belfast, Ireland, 2004.
- [9] C. M. Han and K. Chang, "Ka-band Reflectarray Using Ring Elements," *Electron. Letter*, vol. 39, no. 6, pp. 491-493, 2003.
- [10] N. Misran, R. Cahill and V. F. Fusco, "Concentric Split Ring Element for Dual Frequency Reflectarray Antennas," *Electronic Letters*, vol. 39, no. 25, 2003.
- [11] B. Devireddy, A. Yu, F. Yang and A. Z. Elsherbeni, "Gain and Bandwidth Limitations of Reflectarrays," *Applied Computational Electromagnetics Society (ACES) Journal*, vol. 26, no. 2, pp. 170-178, 2011.



Siti Hafizah Yusop was born in Melaka, Malaysia in 1984. She received the B.Eng. Degree in Communication and Computer Engineering from Universiti Kebangsaan Malaysia (UKM), in 2007. She is currently working toward the M.Sc. degree at the same university. Since February

2008, she is a Research Scholar in the Department of Electrical, Electronic and Systems Engineering, UKM. Her current research interest is reflectarray antenna design.



Norbahiah Misran was born in Selangor, Malaysia in 1976. She received her B.Eng. Degree in Electrical, Electronic & System Engineering from Universiti Kebangsaan Malaysia (UKM) in 1999, and Ph.D. degree in Communication Engineering from Queen's University of Belfast, UK

in 2004. From 1999 to 2004 she was an Assistant Lecturer at UKM. She is currently a lecturer at the same

universiti since 2004. Her current research interests include antennas, RF design and ionospheric studies.



Mohammad Tariqul Islam was born in Dhaka, Bangladesh in 1975. He received the B.Sc. and M.Sc. Degree in Applied Physics and Electronics from University of Dhaka, Dhaka, Bangladesh in 1998 and 2000, respectively and Ph.D. degree in Telecommunication Engineering from Universiti

Kebangsaan Malaysia (UKM) in 2006. He has served as a faculty member of Multimedia University (MMU), Malaysia from May 2007 until May 2008. He is currently a lecturer at Institute of Space Science (ANGKASA), UKM, Malaysia. His research interests concerns the enabling technology for RF, antenna technology, smart antenna receiver and MIMO.



Muhammad Yusof Ismail is a lecturer in Communication Engineering Department, Faculty of Electrical and Electronics Engineering, Universiti of Tun Hussein Onn Malaysia (UTHM). He obtained his Ph.D. degree in Electrical Engineering from Queen's University of Belfast,

UK and B.Eng. Degree in Electrical Engineering from Universiti Kebangsaan Malaysia (UKM). His research interests include design of passive and active microstrip reflectarray antenna, development of reconfigurable reflectarray antenna and developing tunable microwave devices.

A Switchable UWB Slot Antenna using SIS-HSIR and SIS-SIR for Multi-Mode Wireless Communications Applications

Yingsong Li¹, Wenxing Li², and Wenhua Yu²

¹ College of Information and Communication Engineering,
Harbin Engineering University, Harbin, Heilongjiang, 150001, CHINA
liyingsong@hrbeu.edu.cn, liwenxing@hrbeu.edu.cn

² Department of Electrical Engineering,
Pennsylvania State University, University Park, PA 16802, USA
wxy6@psu.edu

Abstract — A coplanar waveguide (CPW) fed ultra wideband (UWB) antenna with switchable functions and notched band characteristics for multi-mode wireless communication applications is proposed in this paper. The proposed UWB antenna has two stop bands which are achieved by using stepped impedance stub (SIS) loaded stepped impedance resonators (SIR) and SIS loaded hexagon stepped impedance resonators (HSIR). The switchable characteristics are obtained by employing two ideal switches on SIS-HSIR and SIS-SIR. By controlling the two switches ON and OFF, the proposed UWB antenna can work in multiple modes. The proposed switchable UWB antennas have been designed, analyzed, fabricated and measured. Simulated and experimental results show that the proposed antenna has switchable characteristics, tunable notch band functions and good radiation patterns. The proposed switchable UWB slot antenna can be used as a multi-mode antenna for multiple protocol communications.

Index Terms — UWB antenna; notch band characteristics; switchable antenna; resonator filters; reconfigurable antenna

I. INTRODUCTION

With the development of wireless communication, high speed data and high efficiency communications have been studied widely in recent years. Especially, in February 2002 the

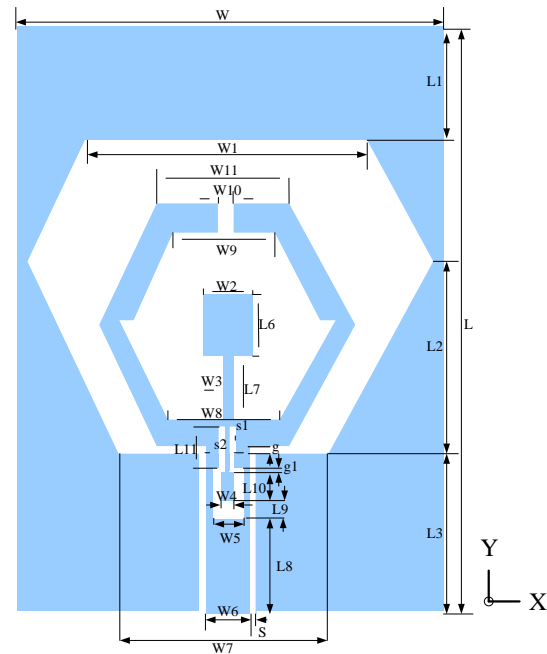
Federal Communications Commission (FCC) in United States conditionally released unlicensed operation of the personal UWB products ranging from 3.1GHz to 10.6GHz [1]. Ultra-wideband (UWB) technology has attracted much attention for use in communication and sensing applications in the commercial domain. Ultra wideband (UWB) is a well-known high speed data ratio, low power and high resistance to interference in wireless communication [1]. For these reasons, UWB communication has been a good topic in academic and industrial field. UWB antenna is an important part in UWB wireless communication applications. Therefore, designing a good antenna can not only reduce the potential interference between UWB systems and narrow band systems but also meet multiple protocol communication requirements. A lot of UWB antennas have been proposed for UWB applications and notch band UWB applications [2-24]. However, most of the previous UWB antennas have large size and complex structures. A number of previous antennas cannot work as a UWB antenna and a notch band UWB antenna, simultaneously. To reduce the size of the antennas, printed wide slot antennas are developed for UWB applications such as rectangular wide slot [7], polygon wide slot [8], circular wide slot [9,23]. Plenty of effective technologies are proposed to reduce the potential interference between UWB systems and narrow band systems. Most of proposed notch band UWB antennas are designed by etching various slots on radiation patch or ground plane

[7-14]. The notch band UWB antennas using stubs [15-18], parasitic strip [19], SRRs [20-23] and integrating with filters in active area [25] are also investigated. However, the notch band characteristic is not good enough to filter the out band signal. The etched slots on radiation patch and ground plane will leak electromagnetic wave. And most of the notched band structures are complex and difficult to design. In addition, the notch depth is poor. The proposed UWB antennas just work in UWB states or notch band UWB states. To let antenna work in multi-mode communications, switch technologies and reconfigurable methods are proposed to meet those requirements [26-30]. SIS and SIRs has good resonator characteristics in designing filters. Recently, SIS is used to design couplers and shown in [31] and SIR and HSIR are employed to design filters [32-34]. These proposed structures have good coupling characteristics and out band suppression functions. In this article, a polygon wide slot antenna for reconfigurable UWB communication applications is presented numerically and experimentally. The proposed antenna can be used as a multi-mode antenna, such as a UWB antenna, a dual notch band UWB antenna or a dual band antenna. The dual notch band functions are obtained by integrating a SIS-HSIR in hexagon radiation patch and a SIS-SIR in CPW transmission signal strip line. By adjusting the dimensions of SIS-HSIR and SIS-SIR, the center frequency and bandwidth of the two notch bands can be tuned to meet practical requirement. The reconfigurable characteristic is achieved by using two ideal switches on SIS-HSIR and SIS-SIR. By controlling the two switches ON and OFF, the proposed antenna can work as a UWB antenna, a dual notch band antenna/tri-band antenna, a notch band UWB antenna or a dual band UWB antenna. Details of the antenna design and both numerical and experimental results are presented and discussed. Good agreement between measured and simulated results demonstrates that the designed antenna is suitable for UWB communications, multi-band communications and notch band UWB communication applications.

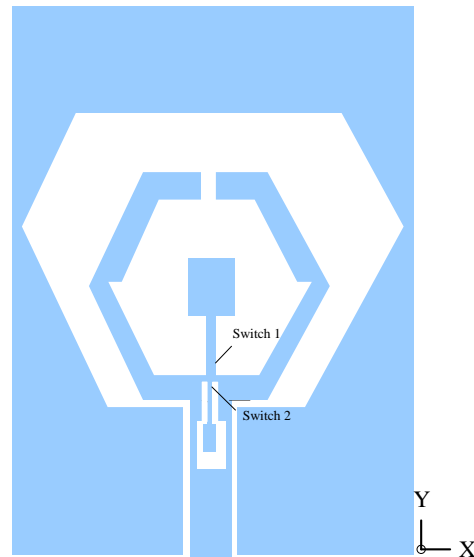
II. ANTENNA DESIGN

The geometries of the proposed antennas are shown in Fig. 1. Figure 1 (a) illustrates the geometry of the proposed dual notch band UWB

antenna (antenna 1). Antenna 1 consists of a polygon wide



(a) Proposed dual notch band UWB antenna.



(b) Proposed switchable UWB antenna.

Fig. 1. Geometry of proposed antennas.

slot, a hexagon radiation patch, a SIS-HSIR etched in hexagon radiation patch, a SIS-SIR embedded in CPW fed signal strip line and a 50Ω CPW fed structure. Figure 1 (b) is the proposed switchable UWB antenna based on the proposed dual notch band UWB antenna 1. In this paper, the proposed

switchable antenna is denoted as antenna 2. To obtain reconfigurable function, two switches are set on SIS-HSIR and SIS-SIR, respectively. In this design, the two switches are ideal and the presence of a metal bridge represents ON state and the absence of a metal bridge represents OFF state [29]. In this paper, a substrate with relative permittivity of 2.65, a loss tangent of 0.002 and a thickness of $h=1.6\text{mm}$ is used in antenna designs. The SIS-HSIR produces the notch band near 5.5GHz (lower notch band) and the SIS-SIR generates the notch band near 8.5GHz (higher notch band). The two switches control the mode of the proposed reconfigurable UWB antenna. The $50\ \Omega$ CPW fed structure consists of the CPW transmission signal strip line with a signal strip width $W_6=3.6\text{mm}$, and gap between the CPW ground plane and transmission signal strip with width $S=0.2\text{mm}$. The $50\ \Omega$ CPW structure of the proposed UWB antenna is designed by using the standard equations [35-36]. The designed antenna has a compact size which is $32\text{mm} \times 24\text{mm}$ ($L \times$

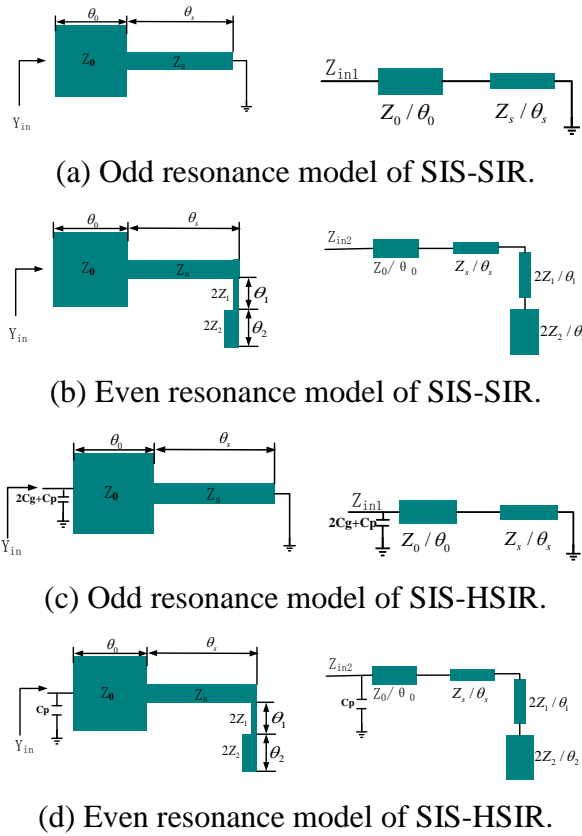


Fig. 2. Transmission line model of symmetrical SIS-SIR and SIS-HSIR.

W). In this paper, the proposed antenna is investigated by means of HFSS which is based on finite element method (FEM).

Transmission line model of the symmetrical SIS-SIR and SIS-HSIR are shown in Figs. 2 (a-d). Figs. 2 (a) and (b) are the transmission line models of SIS-SIR. Figs. 2 (c) and (d) are the transmission line model of SIS-HSIR. From Fig. 1, the SIS-HSIR and SIS-SIR with quasi-lumped SIS connected to the central position of the high impedance line are employed to generate the two notch bands. As illustrated in Fig. 2, Z_0 and θ_0 denote the characteristic impedance and electrical length of the low impedance coupled lines, respectively. The high impedance line has the characteristic impedance and electrical length Z_s and θ_s . The Z_i and θ_i ($i=1,2$) show the characteristic impedance and electrical length of the sections of the inner SIS of SIS-HSIR which is etched on the hexagon radiation patch and SIS-SIR which is embedded on the CPW transmission signal strip line. Moreover, gap W_{10} of the proposed SIS-HSIR is equivalent to capacitances C_p and $C_g/2 + C_p$ for odd mode and even mode, respectively [33]. The proposed dual notch band UWB antenna integrated with SIS-HSIR and SIS-SIR configurations can be analyzed in terms of odd and even excitations. The following resonance frequencies of SIS-HSIR and SIS-SIR for the odd and even excitations can be separately extracted from condition $Y_{in} = 0$ ($Z_{in} = \infty$) [32-34].

(a) Odd mode resonance condition

$$\tan \theta_0 \tan \theta_s = R, \quad (1)$$

(b) Even mode resonance condition

$$\frac{1}{2R_1} \left[1 + \frac{\tan \theta_0 \tan \theta_1}{R} \right] \left[\frac{\tan \theta_1}{R_1} + \frac{\tan \theta_2}{R_2} \right] + \left[\tan \theta_s + \frac{\tan \theta_0}{R} \right] \left[\frac{1}{R_1} + \frac{\tan \theta_1 \tan \theta_2}{R_2} \right] = 0, \quad (2)$$

where the parameters are described as:

$$R = Z_0 / Z_s, R_1 = Z_1 / Z_s, R_2 = Z_2 / Z_s.$$

As expected from Fig. 2 and the equations (1) and (2), the resonance frequencies for odd mode and even mode can be postulated by using the equations (3) to (6) [32-34].

$$f_r \left(\tan \theta_0 + \frac{\tan \theta_s}{R} \right) - \frac{1}{\pi Z_s R} + \frac{\tan \theta_0 \tan \theta_s}{\pi Z_s R^2} = 0, \quad (3)$$

$$f_r \left[\begin{aligned} & 2R_1 \left(\frac{\tan \theta_1 \tan \theta_2}{R_2} - \frac{1}{R_1} \right) (1 - R \tan \theta_s \tan \theta_1) \\ & + \left(\frac{\tan \theta_1}{R_1} + \frac{\tan \theta_2}{R_2} \right) (\tan \theta_s + R \tan \theta_0) \end{aligned} \right] + \frac{1}{2\pi Z_s} \left(\frac{\tan \theta_1}{R_1} + \frac{\tan \theta_2}{R_2} \right) \left(\frac{\tan \theta_0 \tan \theta_s}{R} - 1 \right) = 0, \quad (4)$$

$$+ \frac{R_1}{\pi Z_s} \left(\frac{\tan \theta_1 \tan \theta_2}{R_2} - \frac{1}{R_1} \right) (\tan \theta_s + \frac{\tan \theta_0}{R}) = 0, \\ f_r (2C_g + C_p) \left(\tan \theta_0 + \frac{\tan \theta_s}{R} \right) - \frac{1}{\pi Z_s R} + \frac{\tan \theta_0 \tan \theta_s}{\pi Z_s R^2} = 0, \quad (5)$$

$$f_r C_p \left[\begin{aligned} & 2R_1 \left(\frac{\tan \theta_1 \tan \theta_2}{R_2} - \frac{1}{R_1} \right) (1 - R \tan \theta_s \tan \theta_1) \\ & + \left(\frac{\tan \theta_1}{R_1} + \frac{\tan \theta_2}{R_2} \right) (\tan \theta_s + R \tan \theta_0) \end{aligned} \right] + \frac{1}{2\pi Z_s} \left(\frac{\tan \theta_1}{R_1} + \frac{\tan \theta_2}{R_2} \right) \left(\frac{\tan \theta_0 \tan \theta_s}{R} - 1 \right) + \frac{R_1}{\pi Z_s} \left(\frac{\tan \theta_1 \tan \theta_2}{R_2} - \frac{1}{R_1} \right) (\tan \theta_s + \frac{\tan \theta_0}{R}) = 0. \quad (6)$$

In this paper, equations (3) and (4) are used to calculate the resonance frequency of SIS-SIR. Equations (5) and (6) are employed to calculate the center resonance frequency of SIS-HSIR. Gap W10 is a capacity which can adjust the center frequency of the proposed lower notch band. The proposed reconfigurable characteristic is obtained by using two ideal switches on SIS-SIR and SIS-HSIR. By controlling the switches ON and OFF, the designed antenna can be used as UWB antenna, a dual notch band UWB antenna/ tri-band antenna, a notch band UWB antenna/dual-band antenna. In this paper, the presence of a metal bridge represents ON states and the absence of a metal bridge represents OFF states. During parametric study, two ideal switches are replaced by using a microstrip line with width equal to 1.2mm for SIS-HSIR and 0.6mm for SIS-SIR.

III. PARAMETRIC STUDY

Every geometrical parameter has different effects on the performance of the proposed switchable UWB antenna. In this design, SIS-HSIR and SIS-SIR have public high impedance

line between two ideal switches. So, the parameters of SIS-HSIR and SIS-SIR play an important effect on impedance bandwidth and notch characteristics. In this section, the parameters of SIS-HSIR, SIS-SIR, gap W10 of SIS-HSIR, notch band characteristics and switchable function are investigated and discussed using HFSS. The proposed switchable antenna is optimized and the details parameters are listed as follows: L=32, W=25, L1=5.7, L2=10.3, L3=9, L6=4, L7=2, L8=5, L9=0.3, L10=2, L11=3, W1=15.8, W2=5, W3=1.2, W4=1.4, W5=2.2, W6=3.6, W7=12, W8=6.4, W9=5.6, W10=0.6, W11=8.4, s1=0.5, s2=0.4, S=0.2, g=0.5, g1=0.7. (all in mm). During the investigation, one parameter is changed and the other parameters are fixed.

A. Effects of length L6 of SIS-HSIR

Figure 3 gives the simulated return losses of proposed antenna 1 with varying L6. It can be seen from Fig. 3 that the center frequency of the lower notch band moves to low frequency with higher notch band changeless. L6 alters the characteristic impedance Z_i (i=1,2) and electrical length θ_i (i=1,2) of SIS-HSIR. This can be calculated using equations (1), (2), (5) and (6). In this design, SIS-HSIR works in even mode. Therefore, the equations (2) and (6) are chosen to calculate the center frequency of the lower notch band at the beginning of this design.

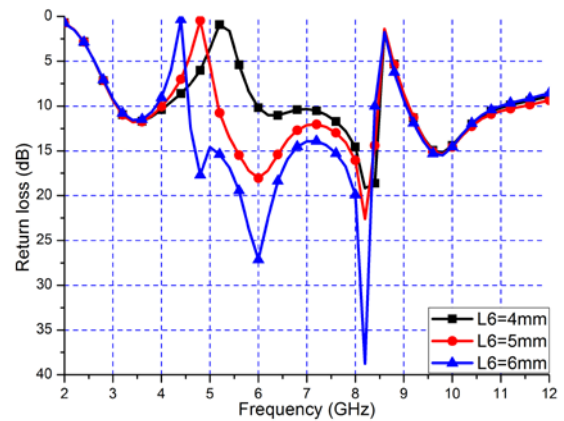


Fig. 3. Effects on return losses of L6.

B. Effects of length W2 of SIS-HSIR

Figure 4 shows the simulated return losses of antenna 1 as a function of frequency for different

values of W_2 . It is found that the center frequency also moves to low frequency with the increase of width W_2 of SIS-HSIR. The center frequency of higher notch band keeps constant. This is due to W_2 which changes the characteristic impedance $Z_i(i=1,2)$ and electrical length $\theta_i(i=1,2)$ of SIS-HSIR. So, the center frequency has been changed. This can be verified by the equations (2) and (6).

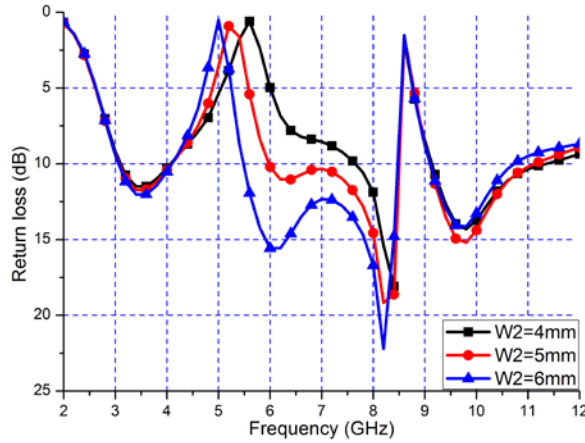


Fig. 4. Effects on return losses of W_2 .

C. Effects of length L_7 of SIS-HSIR

Figure 5 demonstrates the simulated return losses of the proposed dual notched band antenna 1 in terms of L_7 . With varying L_7 from 1.5mm to 2.5mm, the center frequency of lower notch band also moves to low frequency. Furthermore, the impedance bandwidth between 5.4GHz and 8.5GHz is improved. However, the notch depth of the higher notch band deteriorated more or less. This is caused by changed L_7 which has effects on the characteristic impedance and electrical length of public high impedance line of SIS-HSIR and SIS-SIR between two ideal switches of antenna 2.

D. Effects of gap W_{10} of SIS-HSIR

Figure 6 illustrates the simulated return losses of antenna 1 with respect to gap W_{10} of SIS-HSIR. With the increasing of W_{10} , the center frequency of lower notch band is adjusted. The gap W_{10} of the proposed SIS-HSIR is equivalent to capacitances C_p and $C_g/2 + C_p$ for odd mode and even mode, respectively. The changed gap alters the capacity of SIS-HSIR. So, the resonance frequency of SIS-HSIR will be adjusted and can be calculated using formula (5) and (6).

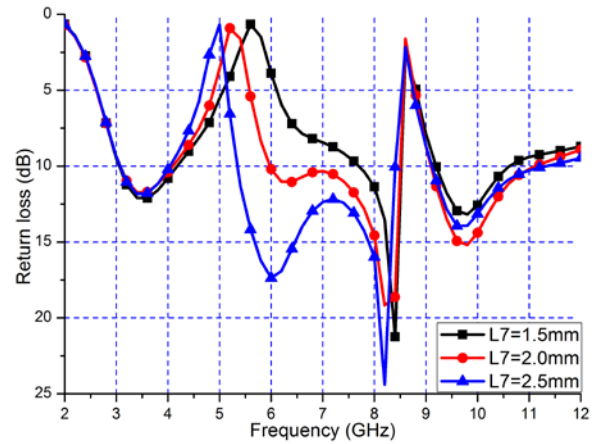


Fig. 5. Effects on return losses of L_7 .

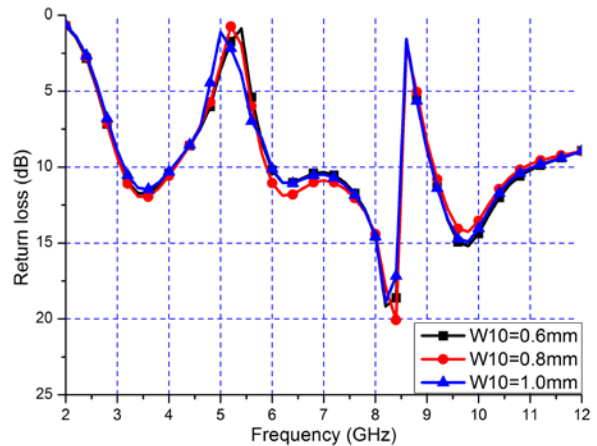


Fig. 6. Effects on return losses of W_{10} .

E. Effects of the length L_{10} of SIS-SIR

Figure 7 shows the simulated return losses of SIS-SIR with varying L_{10} . In terms of L_{10} ranging from 1.0mm to 2.0mm, the higher notch band moves to low frequency. The impedance bandwidth between the two notch bands deteriorated more or less, and then the impedance bandwidth is getting better. In addition, the notch depth of higher notch band is also improved. This is due to that the length L_{10} changes the coupling between SIS and SIR. The changed parameters of SIS-SIR alter the resonance frequency of SIS-SIR.

F. Effects of width W_4 of SIS-SIR

The simulated return losses of antenna 1 with various W_4 are shown in Fig. 8. It can be seen from Fig. 8 that the higher notch band moves to low frequency with the increasing of W_4 . The

impedance bandwidth and notch depth are also improved. However, the lower notch band keeps constant. This is caused by the changed SIS which not only alters the distribution inductance but also changes the characteristic impedance $Z_i(i=1,2)$ and electrical length $\theta_i(i=1,2)$ of SIS-SIR. This can be postulated using (1)-(4). In this paper, the SIS-SIR works in its even mode. So, the resonance frequency can be calculated using equations (2) and (4).

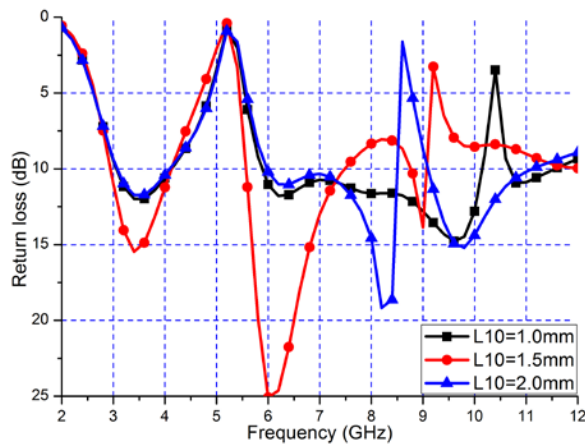


Fig. 7. Effects on return losses of L10.

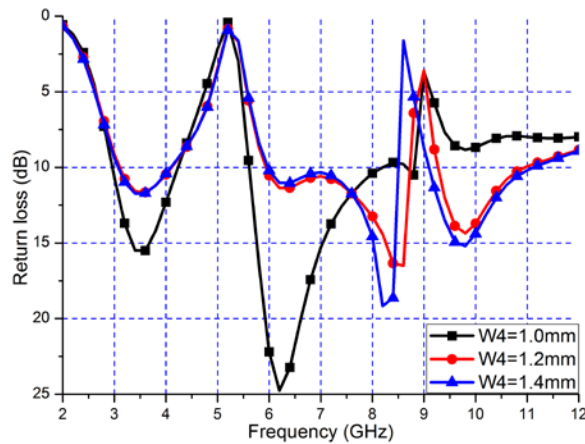


Fig. 8. Effects on return losses of W4.

G. Effects of gap g_1 of SIS-SIR

Figure 9 illustrates the simulated return losses in terms of gap g_1 . From Fig. 9, the notch depth of higher notch band is improved and then the notch depth is deteriorated. The higher notch band also moves to the low frequency by increasing g_1 from 0.5mm to 0.9mm. The length of SIS is changed by various g_1 which changes the coupling capacity of

gap g_1 . The coupling between SIS and SIR is also changed. In this paper, the adjustment of SIS-SIR is limited by the width of the CPW transmission signal line W6. Therefore, by choosing proper coupling gap g_1 , a proper higher notch band can be adjusted to meet the requirement of our project.

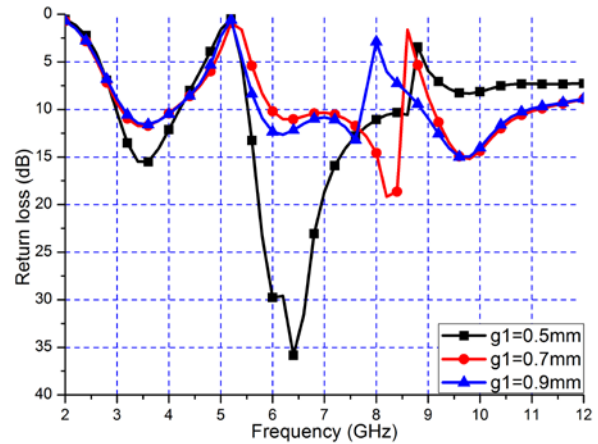


Fig. 9. Effects on return losses of g_1 .

H. Notch band characteristics

Figure 10 demonstrates the proposed notch band characteristic of antenna 1. It can be seen from Fig. 10 that antenna 1 with SIS-HSIR and SIS-SIR has two notch bands near 5.5GHz and 8.7GHz, respectively. Antenna 1 with only SIS-HSIR only has a lower notch band and antenna 1 with only SIS-SIR has a higher notch band. So, the lower notch band near 5.5GHz is produced by SIS-HSIR and the higher notch band is generated by SIS-SIR. The two notch band can be adjusted independently according to the investigation and discussions aforementioned. Antenna 1 without SIS-HSIR and SIS-SIR is a UWB antenna covering the whole band ranging from 3.1GHz to 10.6GHz. In addition, antenna 1 with only SIS-SIR has a resonance frequency near 11GHz. This is caused by SIS-SIR embedded in CPW transmission line which changes the current flowing along CPW excitation line.

I. Switchable characteristics

Figure 11 expounds the simulated switchable characteristic of proposed switchable antenna 2. In this simulation, two ideal switches are used to simulate the switchable functions. Two ideal switches are replaced by using a microstrip line with width equal to 1.2mm for SIS-HSIR and

0.6mm for SIS-SIR. The presence of a metal bridge represents ON states and the absence of a metal bridge represents OFF states. The switchable antenna 2 has the same dimension as antenna 1. It can be seen from Fig.11 that antenna 2 is dual notch band UWB antenna with both switches ON. Antenna 2 can be used as a dual notch band UWB antenna or a tri-band antenna. Antenna 2 is a notch band UWB antenna with one switch ON and the other switch OFF. When switch 1 (SW1) is ON and switch 2 (SW2) is OFF, antenna 2 has a notch band near 5.5GHz. The notch band is produced by SIS-HSIR. When switch 1 (SW1) is OFF and switch 2 (SW2) is ON, antenna 2 has a notch band near 8.5GHz. The notch band is produced by SIS-SIR. So, the lower notch band is switched using SW1 and the higher notch band can be switched by controlling SW2. Antenna 2 is a UWB antenna with two switches OFF. The UWB antenna covers the whole UWB band. Antenna 2 has an impedance bandwidth of 8GHz. In a word, antenna 2 can be used as a notch band UWB antenna/ dual band antenna, a dual band antenna/ tri-band antenna or a UWB antenna by controlling proposed switches ON and OFF.

IV. RESULTS AND DISCUSSIONS

Based on the studies and discussions of the parameters of proposed antenna 1, the notch characteristic and switchable functions of antenna 2, antenna 2 has been optimized utilizing HFSS. According to our project, the proposed two notches are located at 5-6GHz for HiperLAN/2 (5.15-5.35GHz and 5.47-5.725GHz in Europe) and IEEE 802.11a bands (5.15-5.35GHz and 5.725-5.825GHz in US) which is used for wireless local area network (WLAN) communications and 4.4GHz-5.0GHz and 8.5GHz-9.0GHz for satellite communication and military communication applications. In this paper, the two notch bands are designed for reducing potential interference between UWB and narrow bands systems. During the optimizing process, the parameters are adjusted according to the results of the parameters study and the optimized results given in section 3.

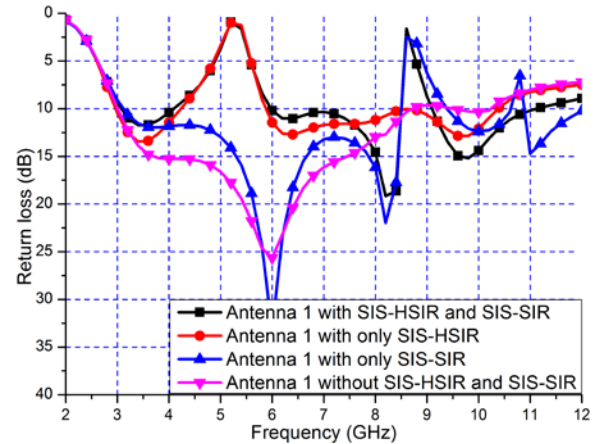


Fig. 10. Effects of SIS-HSIR and SIS-SIR.

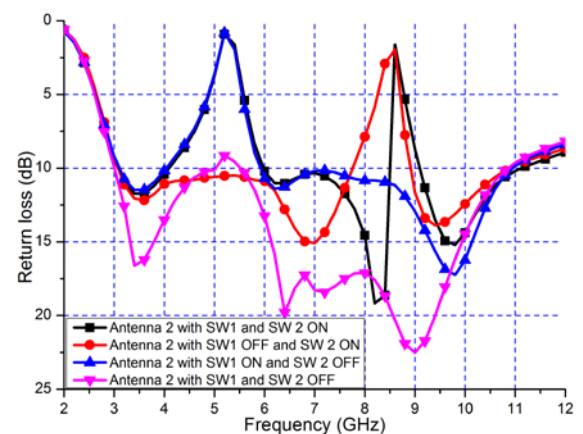
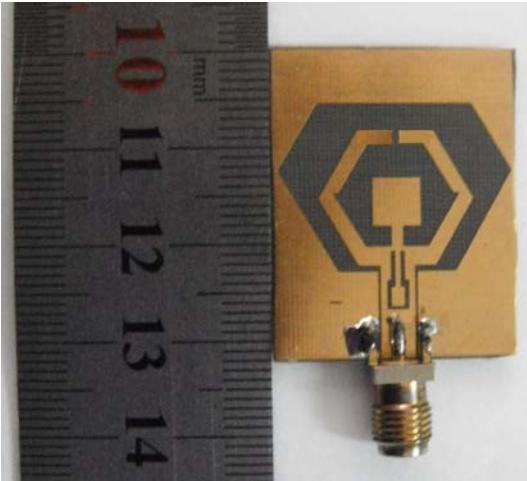
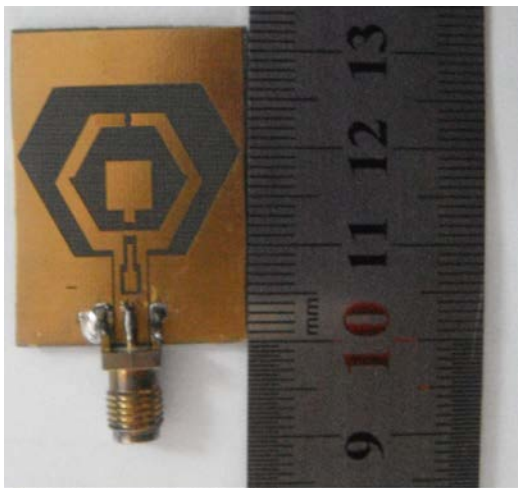


Fig. 11. Effects of the two switches.

To evaluate the performance of optimized UWB antenna 2, the proposed antenna 2 with two switches ON and OFF are fabricated and tested. In this paper, the proposed switchable antennas are manufactured using ideal switches. The presence of a metal bridge represents ON states and the absence of a metal bridge represents OFF states. This is the same as the simulation. The measured return losses of the antennas are obtained by using Anritsu 37347D vector network analyzer. The photographs of the proposed antenna 2 with two switches ON and OFF are shown in Fig.12. Fig.12 (a) is antenna 2 with two switches ON and Fig.12 (b) is antenna 2 with two switches OFF. The return losses of the fabricated switchable antennas are shown in Fig.13.



(a) Antenna 2 with two switches ON.



(b) Antenna 2 with two switches OFF.

Fig. 12. photographs of switchable antennas.

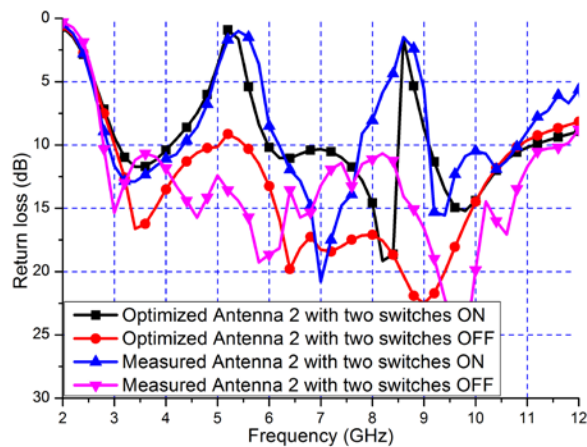


Fig. 13. Return losses of switchable antennas.

From Fig. 13, the measured results agree well with the simulated results which help to verify the accuracy of the simulation. The differences between the simulated and measured values may be due to the errors of the manufactured antenna and the SMA connector to CPW-fed transition, which is included in the measurements but not taken into account in the calculated results. Antenna 2 with two switches ON is a dual notch band UWB antenna. The two notch bands covers C-band (4.4GHz-5GHz), WLAN (5.1GHz-5.9GHz) band and X-band (8.5GHz-9GHz). The two notches can reduce or avoid the potential electromagnetic interference (EMI) between UWB system and narrow band systems, such as WLAN and X-band. Antenna 2 with two switches OFF is a UWB antenna with an impedance bandwidth of 114% according to the center frequency of the proposed UWB antenna. In this paper, antenna 2 is a multi-mode antenna which can be regarded as a UWB antenna, a dual notch UWB antenna/tri-band antenna, a notch band UWB antenna/dual band antenna. It can be seen from Fig.13 that the proposed dual notch bands have better quality factor (notch depth) than most of the previous proposed notch band UWB antennas.

The measured radiation patterns at 4.0GHz, 7.0GHz, 10.0GHz are shown in Fig. 14. The three frequencies are chosen from the frequency under lower notch band, the frequency between lower notch band and higher notch band, and the frequency beyond the higher notch band. In this design, xz plane is H-plane ($\varphi=0^\circ$) and yz-plane is E-plane ($\varphi=90^\circ$) for the proposed switchable antenna. From Fig. 14, we can see that antenna 2 with two switches ON and OFF can give a nearly omni-directional characteristic in H-plane and monopole-like radiation characteristics in E-plane. It was found that the radiation patterns in E-plane deteriorate more or less with the increasing frequency. However, the radiation characteristics are still monopole-like radiation patterns. The radiation patterns of antenna 2 with the two switches ON has a little distorted at upper band. This is caused by the two resonators which leak electromagnetic wave. The leaked electromagnetic wave has some effect on the radiation patterns.

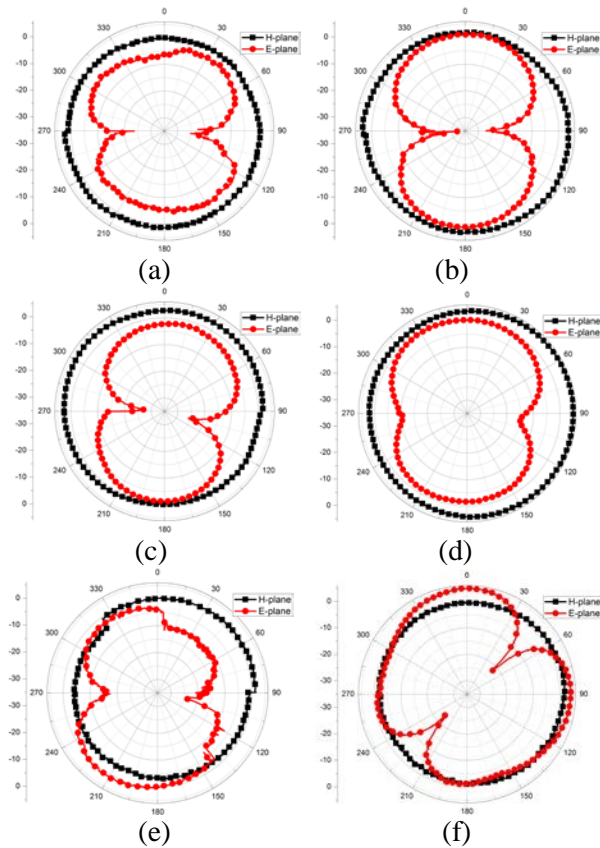


Fig.14. Radiation patterns of proposed switchable antennas (a) 4.0GHz of antenna 2 with two switches ON; (b) 4.0GHz of antenna 2 with two switches OFF; (c) 7.0GHz of antenna 2 with two switches ON; (d) 7.0GHz of antenna 2 with two switches OFF; (e) 10.0GHz of antenna 2 with two switches ON; (f) 10.0GHz of antenna 2 with two switches OFF.

The peak gains of the proposed switchable antennas at these frequencies are achieved by comparing to a double ridged horn antenna. A stable gain can be obtained throughout the operation band except the two notched frequencies. It can be seen from Fig. 15 that the switchable antenna 2 with two switches ON has two notch bands which can reduce the EMI from C-band, WLAN and X-band. The notch band can be adjusted by changing the dimensions of SIS-HSIR and SIS-SIR. The measured gain of the switchable antenna with two switches OFF is increased from 1.7dBi to nearly 5.3dBi which is caused by the deteriorated radiation patterns of the proposed antenna at the high band. In the operation band, the switchable antenna 2 with two switches OFF has stable gains with fluctuation less than 3.6dBi. But the gain of

the switchable antenna with two switches ON dropped quickly from 4.0GHz to 6.0GHz and from 8GHz to 9GHz. As desired, two sharp gains decreased in the vicinity of 5.5GHz and 8.7GHz. The gains drop deeply to -5.2dBi at the lower notch band and -3.6dBi at the higher notch band.

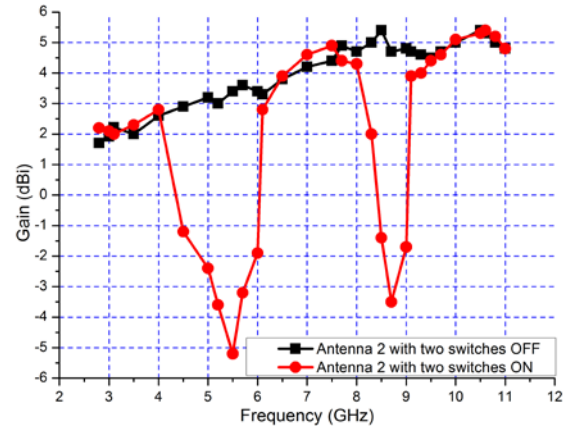


Fig. 15. Gains of antenna 2 with two switches ON and OFF.

V. CONCLUSION

A switchable UWB antenna is presented in this paper numerically and experimentally. The switchable functions are obtained by using two switchable functions are obtained by using two switches on SIS-HSIR and SIS-SIR. By controlling the two switches ON and OFF, the proposed antenna can be used as a UWB antenna, a dual-notch UWB antenna/ tri-band antenna, a notch band antenna/ dual-band antenna. The two notch band characteristics are achieved by using SIS-HSIR and SIS-SIR. The lower notch band is produced by SIS-HSIR and the higher notch band is generated by SIS-SIR. The proposed switchable antenna with two switches ON is a dual notch band antenna which can reduce potential EMI between UWB systems and narrow band systems. While the switchable antenna with one switch ON and the other switch OFF is a notch band UWB antenna or a dual band antenna. The switchable antenna with two switches OFF is a UWB antenna which covers the whole UWB band. The proposed switchable antenna has a small size $32 \times 24 \text{mm}^2$. The ideal switches are used in the simulation and the measurement. The results show that the proposed switchable antenna has a good switchable function, reconfigurable multi-mode characteristic and omni-directional radiation patterns.

ACKNOWLEDGMENT

This work was supported by a grant from the National Defense "973" Basic Research Development Program of China (No.6131380101). This paper is also supported by the National Nature Science Fund of China (No.60902014), Nature Science Fund of Heilongjiang (QC2009C66). The authors are also thankful to Hebei VSTE Science and Technology Co., Ltd. for providing the measuring facility. The authors are indebted to the editor and to the three anonymous reviewers who gave us many useful comments and constructive suggestions to improve this paper.

REFERENCES

- [1] *Federal communications commission, First report and order, Revision of Part 15 of commission's rule regarding UWB transmission system FCC 02-48*, Washington, DC, April 22, 2002.
- [2] T. G. Ma and S. K. Jeng, "A printed dipole antenna with tapered slot feed for ultrawide-band applications," *IEEE Transactions on Antennas and Propagation*, vol. 53, no. 11, pp. 3833-3836, 2005.
- [3] D. S. Javan and O. H. Ghouchani, "Cross Slot Antenna with U-Shaped Tuning Stub for Ultra Wideband Applications," *Applied Computational Electromagnetics Society Journal*, vol. 24, no. 4, pp. 427-432, 2009.
- [4] R. Saleem and A. K. Brown, "Empirical miniaturization analysis of inverse parabolic step sequence based UWB antennas," *Progress In Electromagnetics Research*, vol. 114, pp. 369-381, 2011.
- [5] R. Azim, M. T. Islam, and N. Misran, "Design of a planar UWB antenna with new band enhancement technique," *Applied Computational Electromagnetics Society (ACES) Journal*, vol. 26, no. 10, pp. 856-862, 2011.
- [6] E. Pittella, P. Bernardi, M. Cavagnaro, S. Pisa, and E. Piuzza, "Design of UWB antennas to monitor cardiac activity," *Applied Computational Electromagnetics Society (ACES) Journal*, vol. 26, no. 4, pp. 267-274, 2009.
- [7] Y. S. Li, X. D. Yang, C. Y. Liu, and T. Jiang "Compact CPW-fed ultra-wideband antenna with dual band-notched characteristics," *Electronics letters*, Vol. 46, no. 14, pp. 967-968, 2010.
- [8] L. H. Ye, Q. X. Chu, "3.5/5.5GHz dual band notch ultra-wideband slot antenna with compact size," *Electronics letters*, vol. 46, no. 5, pp. 325-327, 2010.
- [9] S. Barbarino and F. Consoli, "UWB circular slot antenna provided with an inverted-l notch filter for the 5 GHz WLAN band," *Progress In Electromagnetics Research*, vol. 104, 1-13, 2010.
- [10] J. William and R. Nakkeeran, "A New UWB Slot Antenna with Rejection of WiMax and WLAN Bands," *Applied Computational Electromagnetics Society (ACES) Journal*, vol. 25, no. 9, pp.787-793, 2010.
- [11] N. F. Heshmat, J. Nourinia, and C. Ghobadi, "Band-notched ultra-wideband printed open-slot antenna using variable on-ground slits," *Electronics Letters*, vol. 42, no. 6, pp. 315-316, 2006.
- [12] K. Chung, T. Yun, and J. Choi, "Wideband CPW-fed monopole antenna with parasitic elements and slots," *Electronics letters*, vol. 40, no. 17, pp. 1038-1040, 2004.
- [13] Y.S. Li, X. D. Yang, Q. Yang, and C. Y. Liu, "Compact coplanar waveguide fed ultra wideband antenna with a notch band characteristic," *AEU - International Journal of Electronics and Communications*, vol. 65, no.11, pp. 961-966, 2011.
- [14] W. J. Lui, C. H. Cheng, and H. B. Zhu, "Frequency notched printed slot antenna with parasitic open-circuit stub," *Electronics letters*, vol. 41, no. 20, pp.1094-1095, 2005.
- [15] C. Y. Pan, K. Y. Chiu, J. H. Duan, and J. Y. Jan, "Band-notched ultra-wideband planar monopole antenna using shunt open-circuited stub," *Microwave and Optical Technology Letter*, vol. 53, no. 7, pp. 1535-1537, 2011.
- [16] H. W. Liu, C. H. Ku, T. S. Wang, and C. F. Yang. "Compact Monopole Antenna with Band-notched Characteristic for UWB Applications," *IEEE Antenna and Wireless Propagation Letters*, vol. 9, pp. 397-400, 2010.
- [17] M. Ojaroudi, G. Ghanbari, N. Ojaroudi, and C. Ghobadi, "Small Square Monopole Antenna for UWB Applications with Variable Frequency Band-Notch Function," *IEEE Antenna and Wireless Propagation Letters*, vol. 8, pp. 1061-1064, 2009.
- [18] Y. S. Li, X. D. Yang, C. Y. Liu, and T. Jiang, "Analysis and investigation of a cantor set fractal UWB antenna with a notch-band characteristic," *Progress In Electromagnetics Research B*, vol. 33, pp. 99-114, 2011.
- [19] W. X. Liu and Y.-Z. Yin, "Dual band-notched antenna with the parasitic strip for UWB," *Progress In Electromagnetics Research Letters*, vol. 25, pp. 21-30, 2011.
- [20] J. Kim, C. S. Cho, and J.W. Lee, "5.2GHz notched ultra wideband antenna using slot-type

- SRR, " *Electronics Letters*, vol. 42, no. 6, pp. 315-316, 2006.
- [21] Y. Zhang, W. Hong, C. Yu, Z.Q. Kuai, Y.D. Don, and J. Y. Zhou, "Planar Ultrawideband Antennas With Multiple Notched Bands Based on Etched Slots on the Patch and/or Split Ring Resonators on the Feed Line, " *IEEE Transactions on Antennas and Propagation*, vol. 56, no. 9, pp. 3063-3068, 2008.
- [22] J. C. Ding, Z. L. Lin, Z. N. Ying, and S. L. He, "A compact ultra-wideband slot antenna with multiple notch frequency bands," *Microwave and Optical Technology Letter*, vol. 49, no. 12, pp. 3056-3060, 2007.
- [23] S. Sadat, S. D. S. Javan, and M. Houshmand, "Design of a microstrip square-ring slot antenna filled by an H-shape slot for UWB applications," *2007 IEEE AP-S International Symposium on Antennas and Propagation*, pp.705-708, 2007.
- [24] M. Naghshvarian Jahromi and N. Komjani-Barchloui, "Analysis of the behavior of Sierpinski carpet monopole antenna, " *Applied Computational Electromagnetics Society Journal*, vol. 24, no. 1, pp. 32-36, 2009.
- [25] A. Djaiz, M. Nedil, M. A. Habib and T. A. Denidni, "Design of a new UWB integrated antenna filter with a rejected WLAN band at 5.8GHz," *Microwave and optical Technology Letters*, vol. 53, pp. 1298-1302, 2011.
- [26] C. Y. D. Sim, W. T. Chung, and C. H. Lee, "Planar UWB antenna with 5 GHz band rejection switching function at ground plane," *Progress In Electromagnetics Research*, vol. 106, pp. 321-333, 2010.
- [27] S. Nikolaou, N. D. Kingsley, G. E. Ponchak, J. Papapolymerou, and M. M. Tentzeris, "UWB elliptical monopoles with a reconfigurable band notch using MEMS switches actuated without bias lines, " *IEEE Transactions on Antennas and Propagation*, vol. 57, no. 8, pp. 2242-2251, 2009.
- [28] K. H. Kim and S. O. Park, "Analysis of the small band-rejected antenna with the parasitic strip for UWB," *IEEE Transactions on Antennas and Propagation*, vol. 54, no. 6, pp. 1688-1692, 2006.
- [29] M. R. Hamid, P. S. Hall, P. Gardner, and F. Ghanem, "Switched WLAN wideband tapered slot antenna, " *Electronics letters*, vol. 46, no. 1, pp. 23-24, 2010.
- [30] P. Y. Qin, A. R. Weily, Y. J. Guo, T. S. Bird, and C. H. Liang, "Frequency reconfigurable quasi-Yagi folded dipole antenna, " *IEEE Transactions on Antennas and Propagation*, vol. 58, no. 8, pp. 2742-2747, 2010.
- [31] M. Nosrati, M. Daneshmand, and B. S. Virdee, "Novel compact dual narrow/ wideband branch line couplers using T-shaped stepped impedance stub lines, " *International Journal of RF and Microwave Computer-Aided Engineering*, vol. 21, no. 6, pp. 642-649, 2011.
- [32] C. Y. Liu, T. Jiang, and Y. S. Li, "A Novel UWB Filter with Notch-band Characteristic Using Radial-UIR/SIR Loaded Stub Resonators", *Journal of Electromagnetic Waves and Applications*, vol. 25, pp. 233-245, 2011.
- [33] X. Luo, J. G. Ma, and E. P. Li, "Dual-band bandpass filter using stepped-impedance stub-loaded hexagonal stepped impedance resonator (SIR), " *Microwave and Optical Technology Letter*, vol. 53, no. 5, pp. 1147-1150, 2011.
- [34] M. Makimoto and S. Yamashita, *Microwave resonators and filters for wireless communication: theory, design and application*, Springer, 2001.
- [35] S. Kaya and K. Guney, "New and accurate synthesis formulas for asymmetric coplanar waveguides," *Microwave and Optical Technology Letter*, vol. 53, no. 9, pp. 1991-1996, 2011.
- [36] R. Garg, P. Bhartia, I. Bahl, and A. Ittipiboon, *Microstrip antenna design hand book*, 1st ed. Artech House; pp. 794-795. 2001



Yingsong LI received his B.S. degree in electrical and information engineering in 2006, and M.S. degree in Electromagnetic Field and Microwave Technology from Harbin Engineering University, 2006 and 2011, respectively. Now he is a Ph.D. Candidate in Harbin

Engineering University, China. He is a student member of Chinese Institute of Electronics (CIA), IEEE, IEICE and The Applied Computational Electromagnetics Society (ACES). He serves as receivers for the journals IEEE Antennas and Wireless Propagation Letters, International Journal of Electronics, Progress In Electromagnetics Research Series, Journal of Electromagnetic Waves and Applications, COMPEL: The International Journal for Computation and Mathematics in Electrical and Electronic Engineering and Applied Computational Electromagnetics Society Journal. His recent research interests are mainly in microwave theory, small antenna technologies and computational electromagnetic.



Wenxing LI received the B.S. and M.S. degrees from Harbin Engineering University, Harbin, Heilongjiang, China, in 1982, 1985, respectively. He is currently a full professor of College of Information and Communication Engineering, Harbin Engineering University,

China. He is also the head of Research Centre of EM Engineering & RF Technology. He visited the Department of Electrical Engineering, The Pennsylvania State University, USA from June to August 2010. And he visited Oriental Institute of Technology, Taiwan from August to October, 2010. He is also the organizer of the 30th Progress in Electromagnetics Research Symposium (PIERS), IEEE International Workshop on Electromagnetics (iWEM), TPC of 2012 Asia-Pacific Symposium on Electromagnetic Compatibility (APEMC 2012) and 2012 Global Symposium on Millimeter Waves (GSMM 2012). His recent research interests are mainly in computational electromagnetic, microwave engineering, modern antenna design and millimeter wave circuits.



Wenhua Yu joined the Department of Electrical Engineering of the Pennsylvania State University, and has been a group leader of electromagnetic communication lab since 1996. He received his PhD in Electrical Engineering from the Southwest Jiaotong University in 1994. He worked at Beijing Institute of Technology as a Postdoctoral Research Associate from February 1995 to August 1996. He has published one book on CFDTD software and two FDTD books: Conformal Finite-Difference Time-Domain Maxwell's Equations Solver: Software and User's Guide (Artech House, 2003), Parallel Finite-Difference Time-Domain (CUC Press of China, 2005, in Chinese), and Parallel Finite-Difference Time-Domain Method (Artech House, 2006). He has published over 100 technical papers and four book chapters. He developed created the Computer and Communication Unlimited [Http://www.2comu.com](http://www.2comu.com), and serves as its President. He is a Senior Member of the IEEE. He was included in Who' Who in America, Who' Who in Science and Engineering, and Who's Who in Education. He is also a visiting professor and PhD advisor of the Communication University of China. Dr. Yu's research interests include computational electromagnetic, numerical techniques, parallel computational techniques, and the theory and design of parallel computing systems.

A CPW Dual Band Notched UWB Antenna

M. Mighani¹, M. Akbari², and N. Felegari²

¹Faculty of Eng., Department of Electrical Engineering
Aeronautical University, Tehran, Iran
mojtaba.mighani@gmail.com

²Faculty of Eng., Department of Electrical Engineering
Urmia University, Urmia, Iran
akbari.telecom@gmail.com, n.felegari@gmail.com

Abstract — In this paper, a coplanar waveguide (CPW)-fed microstrip antenna for ultra wideband application is presented. By using two branches of microstrip line and two slot lines on the antenna, two notches for interference bands has been created. The antenna has a rather compact structure; with total size of $25 \times 25 \times 1 \text{ mm}^3$. This antenna covers bandwidth of more than 137% from 2.96 GHz to 16 GHz for $S_{11} < -10 \text{ dB}$.

Index Terms — Coplanar waveguide (CPW), microstrip antennas and dual band-notched, ultra wideband (UWB),

I. INTRODUCTION

After allocation of the frequency band of 3.1-10.6 GHz (UWB) for commercial use by the FCC (Federal Communication Commission) in 2002 [1], the requirements and attentions towards the UWB system are due to its inherent merits such as high data rate, small emission power, highly secure environment, low cost for short range access, and remote sensing applications. But there are many narrowband communication systems which severely interfere with the UWB communication system. Most notable among them are the Wireless Local Area Network (WLAN) and Worldwide Interoperability for Microwave Access (WiMAX), which operate with the center frequencies of 5.2 GHz (5150-5350 MHz), 5.8 GHz (5725-5825 MHz) for WLAN and 3.5GHz (3400-3690 MHz), 5.5 GHz (5250-5850 MHz) bands for WiMAX. To mitigate this interference problem, various UWB antennas with band

notched characteristics have been developed [2-7]. CPW monopole antennas have become popular due to wide operation bandwidth, good radiation pattern, simple structure, planar, light weight and easy integration of monolithic microwave integrated circuits (MMIC). In this paper, a CPW-Fed UWB antenna with dual band notched features is presented. The two notched bands minimize the potential interference between the UWB system and WLAN/WiMAX narrow band communication systems.

The proposed antenna can be used in UWB systems which need no filter to suppress dispensable bands. Both Ansoft high frequency simulation structure (HFSS) [8] and computer simulation technology (CST) [9] 3-D electromagnetic EM simulators are used to optimize the presented design. The proposed antenna with the dual-band notch is successfully implemented and the simulation results show reasonable agreement with the measurement results. Section II describes the antenna design, discussions on results is presented in Section III followed by conclusive comments and further scope in Section IV.

II. ANTENNA DESIGN

The geometry of the proposed CPW-fed antenna for UWB applications is depicted in Fig. 1; also the optimized parameter values are listed in Table 1.

Characteristic impedance of CPW feed line is approximately 50 ohm with the center line width $W_f=3\text{mm}$, and gap width $W_{fg}=0.3\text{mm}$. The CPW

antenna has been designed based on the idea presented in [10]. Figure 2 exhibits the fabricated antenna.

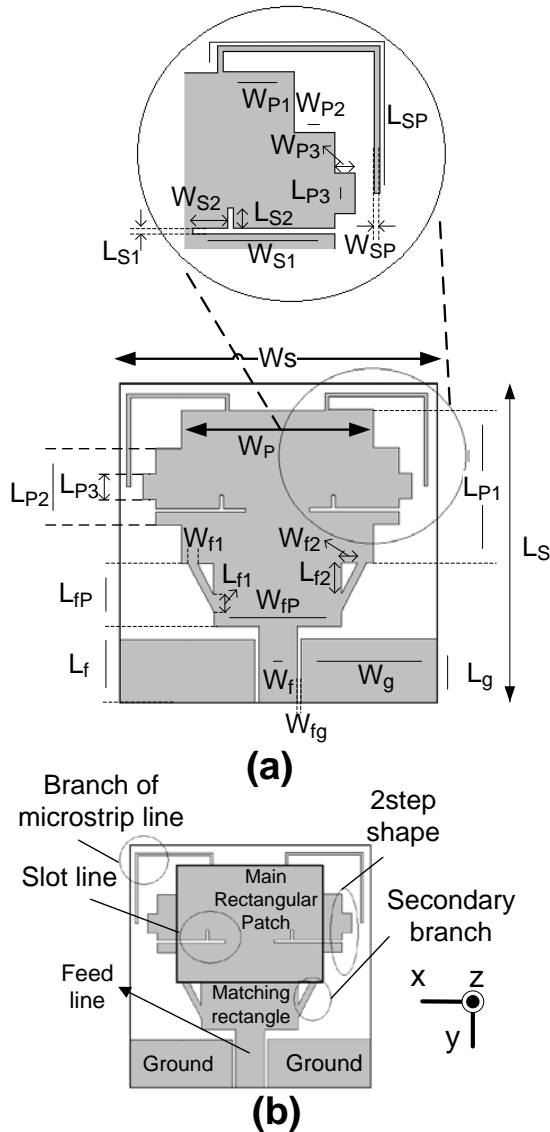


Fig. 1. The antenna geometry and its design parameters.

Table 1: Optimal parameter values of the antenna

L_S	W_S	L_f	W_f	L_g	W_g	W_{fg}
25	25	6	3	5	10.7	0.3
L_{P1}	W_P	W_{P1}	L_{P2}	W_{P2}	L_{P3}	W_{P3}
12	15	3.45	6	2	2	1
L_{fP}	W_{fP}	L_{SP}	W_{SP}	W_{S1}	W_{S2}	L_{S1}
5	10	16.6	0.3	7	1.7	0.3
L_{S2}	L_{f1}	W_{f1}	L_{f2}	W_{f2}	ϵ_r	h
1	1.25	0.75	2.5	1.25	4.4	1

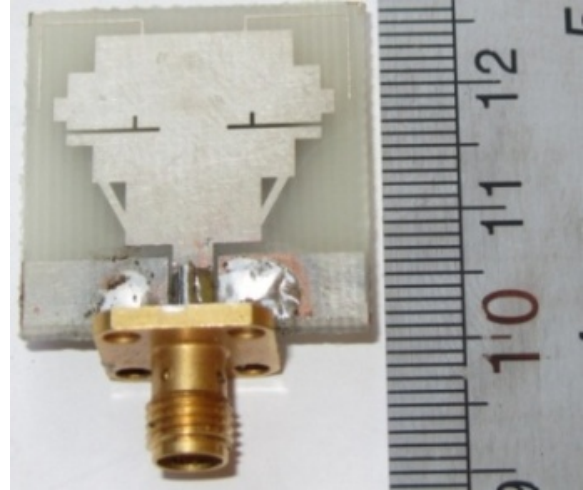


Fig. 2. Photograph of the fabricated antenna.

Total size of the referenced antenna is $30 \times 26 \times 1.6 \text{ mm}^3$, and its bandwidth is from approximately 3 GHz up to 11 GHz (114%), but the size of the proposed antenna in this letter is $25 \times 25 \times 1 \text{ mm}^3$ which its area 20% has been decreased while both of them have been printed on a low cost FR-4 substrate with dielectric constant of 4.4. Meanwhile, bandwidth of the proposed antenna is from 2.96 GHz up to 16 GHz (137%) which 23% has been increased. To increase bandwidth has been used the technique of step shape of [11] and also to create notch has been needed to a resonance, so the authors have designed two branch strip lines which this technique has been inserted from [12]. The modifications have been performed on the rectangular patch to improve its operating bandwidth and also to create two notches for WiMAX and WLAN bands. After obtaining values of W_f and W_{fg} , it is needed to match between the patch and the feed line, there for used a rectangle with length of L_{fP} and width of W_{fP} respectively with values 5, 10mm respectively has been used. In the next stage, to improve the impedance bandwidth has been applied from the two step shapes in the both sides of rectangular patch with lengths and widths respectively L_{P2} , L_{P3} and W_{P2} , W_{P3} and the optimized values are summarized in Table 1. Also, the Trident feed technique has been applied for further improvement of bandwidth, where two branches have been used to connect the matching rectangle

into the main patch. Physical dimensions of the trident as L_{f1} and W_{f1} are illustrated in Fig. 1.

In order to create two resonant frequency centers at 3.4 GHz and 5.5 GHz, there have been used two techniques as follow:

- 1- Using two slot lines on both sides of the patch with lengths of $\lambda/4$.
- 2- Using two branch strip lines over the main patch.

In the next section, the antenna design procedure will be dealt, and the effect of various parameters on reflection coefficient will be discussed.

III. ANTENNA PERFORMANCE AND DISCUSSION

A. Full-band design

In this section, the design procedure of the CPW fed UWB antenna with reflection coefficient curves are demonstrated. Note, that the simulated reflection coefficient results are obtained using the HFSS and CST software. At first, the effect of width variation of the matching rectangle (W_{fp}), which has connected the feed line into the radiated (radiation) patch, on bandwidth was studied. With regard to Fig. 3, it is clear that the best value for W_{fp} is 10mm.

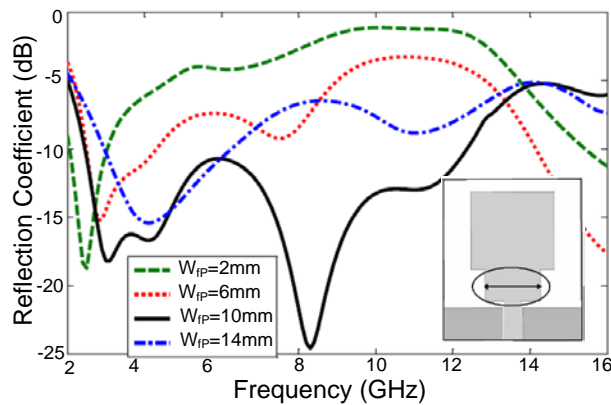


Fig. 3. Reflection coefficients for different values of W_{fp} .

Here, the proposed methods result in bandwidth enhancement of the impedance. The first, secondary branches are added on both sides of the rectangle and effect of them on reflection coefficients is visible in Fig. 4. From

this figure, it can be seen that the secondary branches improve the bandwidth more than 1 GHz on the upper band.

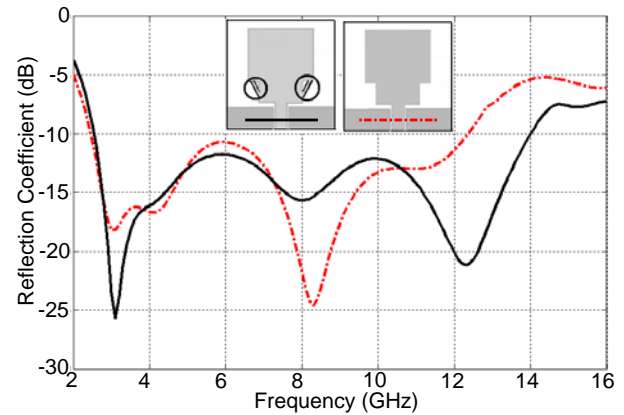


Fig. 4. Reflection coefficients for the antenna with and without the secondary branches.

Figures 5 and 6 show the effects of Step 1 and Step 2 on the reflection coefficient, respectively. Figure 5 exhibits that, the result of Step 1 is an improvement in the middle and upper bands. Likewise, from Fig. 6, it is clear that, effect of Step 2 is the expansion of the lower band of the antenna's bandwidth.

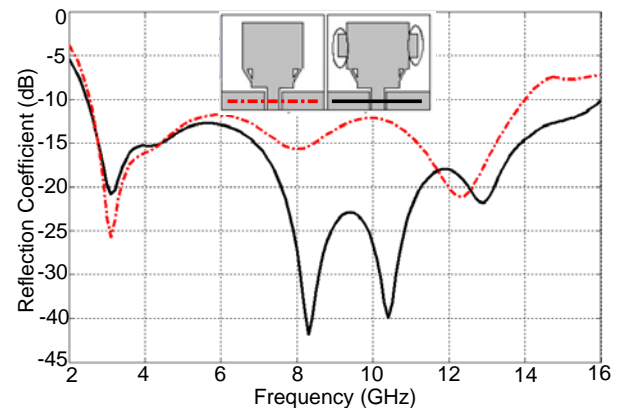


Fig. 5. Simulated reflection coefficients for the antenna with and without Step 1.

Although the bandwidth of the middle band is decreased, but the antenna designer's main goal is to cover the defined UWB bandwidth by FCC, so it can be concluded that being the Step 2 for the proposed antenna is useful. With the accomplished modifications on the antenna, as Fig. 6 depicts, the

simulated bandwidth of the antenna has been enhanced more than FCC defined frequency range and has been obtained from 2.29 to 16 GHz.

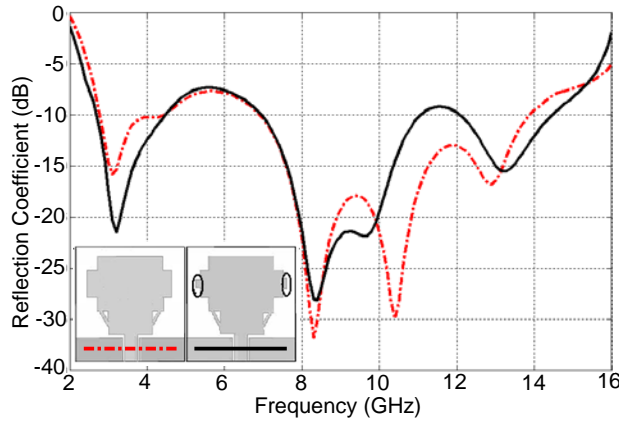


Fig. 6. Simulated reflection coefficients for the antenna with and without Step 2.

B. Single-notch design

In the next stage, the antenna designer's aim is to create the notches on the bandwidth by using various techniques such as slotting in the patch and adding microstrip lines over the patch. For this, it is better to be looked at Fig. 1 once again. For the proposed antenna are used two techniques to create notches at the center frequencies of 3.4 and 5.5 GHz. In other words, the antenna has the capability of filtering the interference bands of WLAN and WiMAX. In general, the length of the slot has the inverse relationship with frequency and type of substrate.

$$\epsilon_{re} = \frac{1+\epsilon_r}{2} \quad (1)$$

$$L = \frac{\lambda_g}{4} = \frac{300}{4f(\text{GHz})\sqrt{\epsilon_{re}}} \quad (\text{mm}) \quad (2)$$

$$L = \frac{\lambda_g}{2} = \frac{300}{2f(\text{GHz})\sqrt{\epsilon_{re}}} \quad (\text{mm}) \quad (3)$$

By simulations, it can be found when slots are inside of the patch, like the U-shaped slot, the length of slots is $\lambda_g/2$, but there is another way to decrease the length of slots down to $\lambda_g/4$ like the used slot in the proposed antenna, on the other hand, the using of slots in which a side of them are not insight of patch. It means that the slot is started from the outer edges of patch. To understand more, the function of the slots in the design, the

characteristics of three designs of without strip lines are compared with each other. The simulated results have been plotted in Fig. 7.

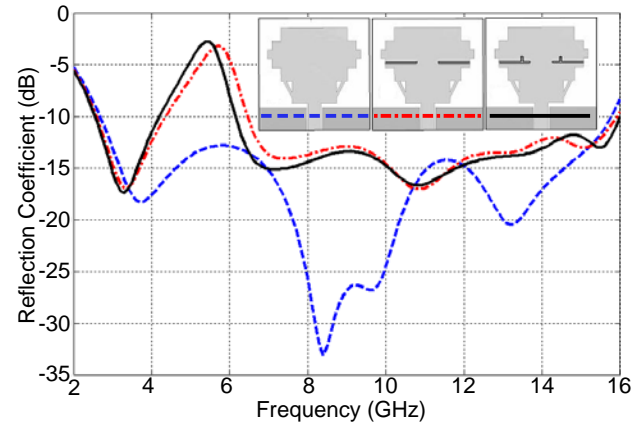


Fig. 7. Simulated reflection coefficients for the antennas with and without slots.

As shown in Fig. 7, it is found that by using slots, the notch can be created in the impedance bandwidth. To adjust the notch bandwidth at the frequency band from 5150 MHz to 5850MHz (WiMAX and WLAN) is used from the two sub slots. With regard to Fig. 7, by the sub slots can be shifted the central frequency of notch and also can be increased the amplitude of notch. There is the other point in a way that to enhance magnitude of notch is applied from the two slots on the both sides of the patch instead of one slot.

C. Another single-notch design

In this antenna to create the other notch at frequency band of 3.3 to 3.69 GHz (WiMAX) has been used the two strip lines over the patch. Figure 8 illustrates simulated reflection coefficient characteristics for the antenna with and without strip lines. To increase the magnitude on the notched band two strip lines has been used instead of one strip line. The proposed antenna has been implemented based on the dimensions presented in Table 1.

The VSWR of the proposed antenna has been measured using an Agilent E8362B network analyzer in its full operational span (10 MHz–20 GHz). The simulated and measured VSWR of the fabricated antenna are depicted in Fig. 9.

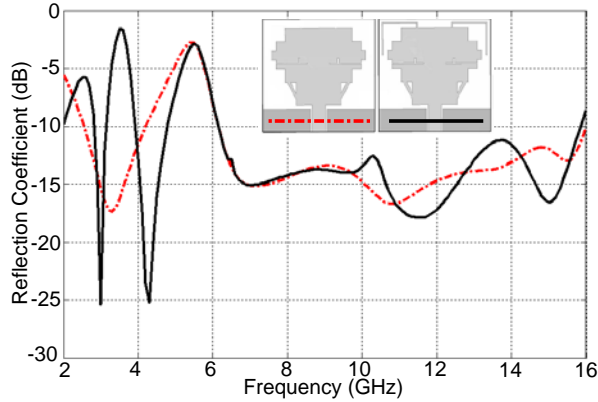


Fig. 8. Simulated reflection coefficients for the antennas with and without the strip lines.

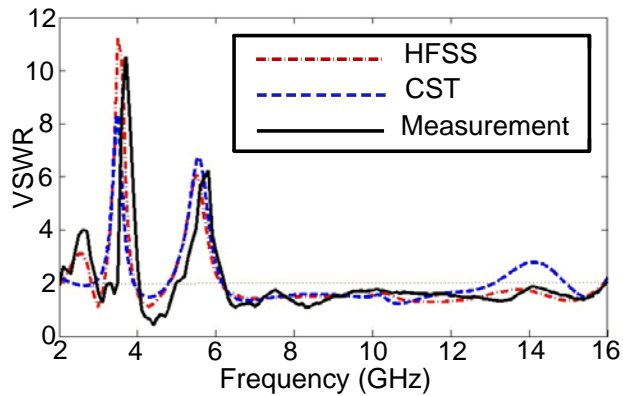


Fig. 9. Simulated and measured VSWR for the proposed antenna.

The results show that the antenna impedance bandwidth extends from 2.96 up to 16 GHz, as high as 137%. It is apparent that the presented antenna can be used for higher frequencies above the FCC band. This behavior almost was predicted from HFSS and CST simulators. Good agreement between simulated and measured results is observed and a bit of difference between them is attributed to factors such as SMA connector effects, fabrication imperfections, and inappropriate quality of the microwave substrate.

D. Time domain analysis

In ultra wideband systems, the information is transmitted using short pulses. Hence, it is important to study the temporal behavior of the transmitted pulse. The communication system for UWB pulse transmission must limit distortion, spreading, and disturbance as much as possible.

Group delay is an important parameter in UWB communication, which represents the degree of distortion of pulse signal. The key in UWB antenna design is to obtain a good linearity of the phase of the radiated field because the antenna should be able to transmit the electrical pulse with minimal distortion. Usually, the group delay is used to evaluate the phase response of the transfer function because it is defined as the rate of change of the total phase shift with respect to angular frequency. Ideally, when the phase response is strictly linear, the group delay is constant.

$$\text{group delay} = -\frac{d\theta(\omega)}{d\omega} \quad (4)$$

As depicted in Fig. 10, the group delay variation is less than 0.8ns over the frequency UWB without notched bands which ensure that the pulse transmitted or received by the antenna will not distort seriously and will retain its shape. As expected before, the groups delay variation at notches from 3.3GHz up to 3.69GHz and 5.15GHz up to 5.85GHz, WiMAX and WLAN, with respect to other frequencies is more. Therefore, the proposed antenna is suitable for modern UWB communication systems.

Transient response of the antenna is studied by modeling the antenna by its transfer function. The transmission coefficient S_{21} was simulated in the frequency domain for the face-to-face orientation. Figure 11 shows the magnitude of measured S_{21} for the face-to-face orientation and plot of S_{21} is almost flat with variation less than 15dB in the operating band. The reason of two intense resonances in plot of S_{21} is because of two notches WiMAX and WLAN at frequencies 3.5 and 5.5 GHz.

Phase of S_{21} for the face to face orientation has been also plotted and is shown in the Fig. 12. As previously expected, the plot shows a linear variation of phase in the total operating band except notched bands.

The transfer function is transformed to time domain by performing the inverse Fourier transform. Fourth derivative of a Rayleigh function is selected as the transmitted pulse. The output waveform at the receiving antenna terminal can therefore be expressed by convoluting the input signal and the transfer function. The input and received wave forms for the face-to-face and

side-by-side orientations of the antenna are shown in Fig. 13. It can be seen that the shape of the pulse is preserved very well in all the cases. Using the reference and received signals, it becomes possible to quantify the level of similarity between signals.

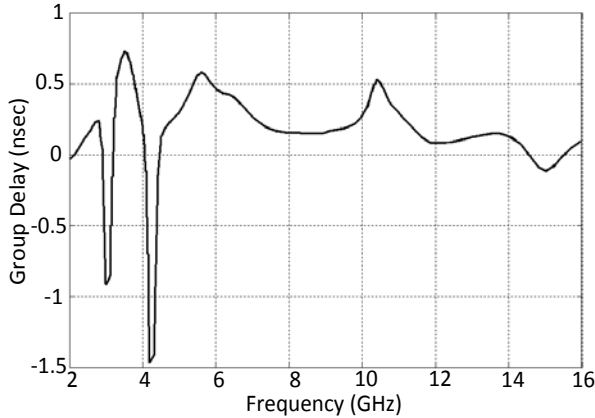


Fig. 10. Simulated group delay versus frequency for the proposed antenna.

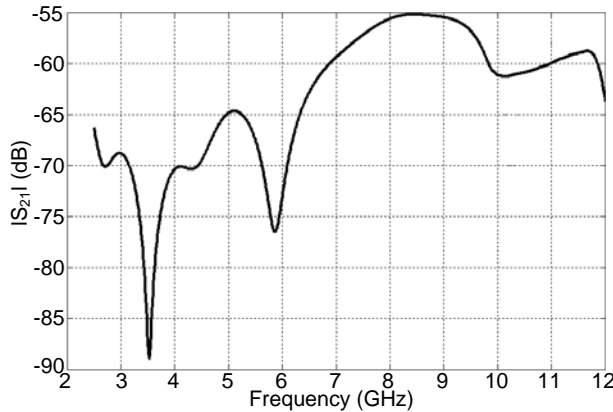


Fig. 11. Simulated S_{21} with a pair of identical UWB antennas for face to face orientation.

In telecommunications systems, the correlation between the transmitted (TX) and received (RX) signals is evaluated using the fidelity factor [21]

$$F = \max_{\tau} \left| \frac{\int_{-\infty}^{+\infty} S(t)r(t-\tau)dt}{\sqrt{\int_{-\infty}^{+\infty} S(t)^2 \cdot \int_{-\infty}^{+\infty} r(t)^2 dt}} \right|, \quad (5)$$

where $S(t)$ and $r(t)$ are the TX and RX signals, respectively. For impulse radio in UWB communications, it is necessary to have a high

degree of correlation between the TX and RX signals to avoid losing the modulated information. However, for most other telecommunication systems, the fidelity parameter is not that relevant. In order to evaluate the pulse transmission characteristics of the proposed double band-notched antenna, two configurations (side by side and face to face orientations) were chosen. The transmitting and receiving antennas were placed in a $d=0.5$ m distance from each other. As shown in Fig. 13, although the received pulses in each of two orientations are broadened, a relatively good similarity exists between the RX and TX pulses. Using (4), the fidelity factor for the face to face and side by side configurations was obtained equal to 0.94 and 0.89, respectively. These values for the fidelity factor show that the antenna imposes negligible effects on the transmitted pulses. The pulse transmission results are obtained using CST.

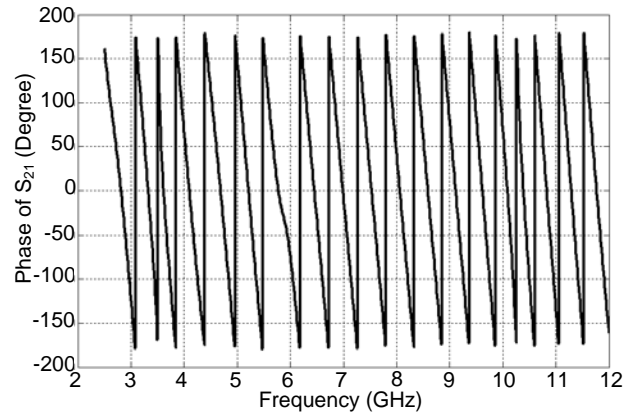


Fig. 12. Simulated Phase of S_{21} for face to face orientation.

E. Radiation characteristics

The $y-z$ plane and the $x-z$ plane are selected to show the antenna radiation patterns referred to as E-plane and H-plane, respectively. Figures 14 and 15 respectively show the antenna normalized radiation pattern at E-plane and H-plane.

According to Fig. 14, it is clear that the proposed antenna has a nearly bidirectional pattern and Fig. 15 also depicts that the antenna has a non directional pattern required to receive information signals from all directions. In addition, the gain curve of the proposed antenna is illustrated in Fig. 16.

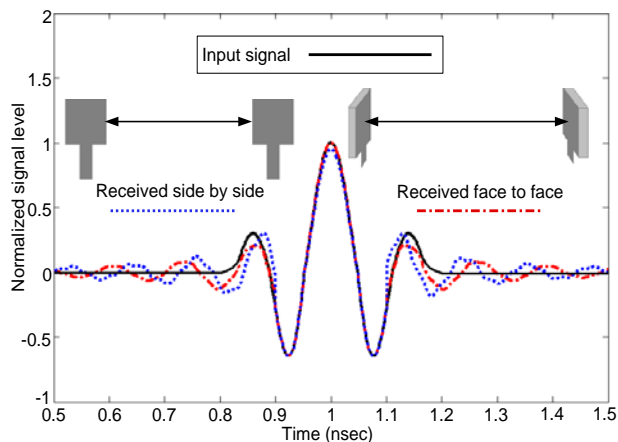


Fig. 13. Transmitted and received pulses.

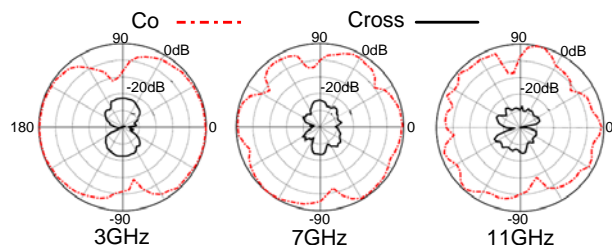


Fig. 14. Measured normalized radiation pattern of the antenna at E-plane.

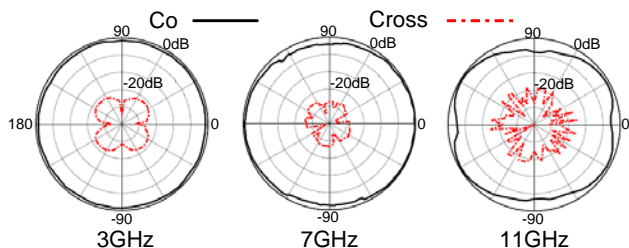


Fig. 15. Measured normalized radiation pattern of the antenna at H-plane.

From these curves it is obvious that the antenna has rather acceptable gain and on the frequency bands of 3.3 to 3.69 GHz and 5.15 to 5.825 GHz, in spite of having compact size of $25 \times 25 \text{ mm}^2$. Using two techniques of strip lines and slots, the antenna has filtered the interference bands of WiMAX and WLAN. The last point from Fig. 16 is that the maximum values of gain for the antenna has been earned at the higher frequencies with values of 5.5 to 6 dB, and also the minimum values of gain is for a dual band notch with values of -4 to -5 dB.

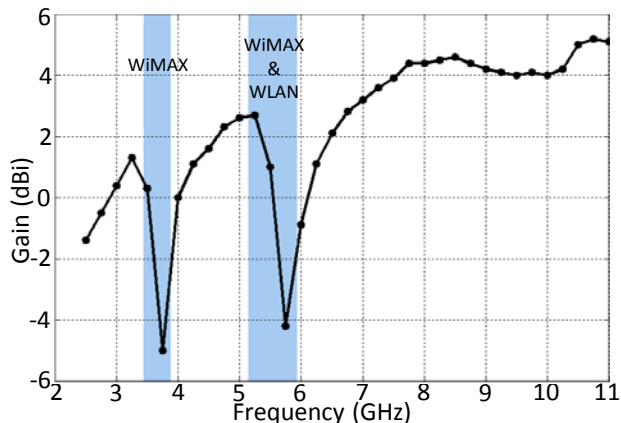


Fig. 16. Measured gain versus frequency for the proposed antenna.

IV. CONCLUSION

A CPW antenna to cover UWB band and to reject interference bands has been presented. The measured bandwidth of the antenna is from 2.96 to 16 GHz. The simulation and measurement results of the proposed antenna show a good agreement in term of the reflection coefficient, and radiation patterns.

REFERENCES

- [1] Federal Communications Commission, First report and order on ultra-wideband technology, FCC 02-48, compact UWB planar antenna with band-notch characterization, Washington, DC, 22nd April, 2002.
- [2] T. D. Nguyen, D. H. Lee, and H. C. Park, "Design and Analysis of Compact Printed Triple Band-Notched UWB Antenna," *Antennas and Wireless Propagation Letters, IEEE*, vol. 10, pp. 403-406, 2011.
- [3] H.-W. Liu, C.-H. Ku, T.-S. Wang, and C.-F. Yang, "Compact Monopole Antenna with Band-Notched Characteristic for UWB Applications," *Antennas and Wireless Propagation Letters, IEEE*, vol. 9, pp. 397-400, 2010.
- [4] R. Azim, M. T. Islam, and N. Misran, "Design of a Planar UWB Antenna with New Band Enhancement Technique," *Applied Computational Electromagnetics Society (ACES) Journal*, vol. 26, no. 10, pp. 856-862, October 2011.
- [5] J. William and R. Nakkeeran, "A New UWB Slot Antenna with Rejection of WiMax and WLAN Bands," *Applied Computational Electromagnetics Society (ACES) Journal*, vol. 25, no. 9, pp. 787-793, September 2010.

- [6] D. S. Javan and O. H. Ghouchani, "Cross Slot Antenna with U-Shaped Tuning Stub for Ultra Wideband Applications," *Applied Computational Electromagnetics Society (ACES) Journal*, vol. 24, no. 4, pp. 427-432, August 2009.
- [7] M. Naghshvarian-Jahromi and N. Komjani-Barchloui, "Analysis of the Behavior of Sierpinski Carpet Monopole Antenna," *Applied Computational Electromagnetics Society (ACES) Journal*, vol. 24, no. 1, pp. 32-36, February 2009.
- [8] Ansoft HFSS User's manual, Ansoft Corporation, Beta Release 11.0, April 2007.
- [9] CST Microwave studio, ver. 2008. Computer Simulation Technology, Framingham, MA, 2008.
- [10] Q.-X. Chu and Y.-Y. Yang, "A Compact Ultra wideband Antenna With 3.4/5.5 GHz Dual Band-Notched Characteristics," *Antennas and Propagation, IEEE Transactions*, vol. 56, no. 12, pp. 3637-3644, 2008.
- [11] M. Akbari, M. Koohestani, C. H. Ghobadi, and J. Nourinia, "A New Compact Planar UWB Monopole Antenna," *International Journal of RF and Microwave Computer-Aided Engineering*, vol. 21, no. 2, pp. 216-220, March 2011.
- [12] M. Akbari, C. H. Ghobadi, and J. Nourinia, "Internal Multiband PIFA Antenna for GPS/DCS/PCS/UMTS/WLAN Operation in the Mobile Device," *IEICE Electronics Express*, vol. 6, no. 24, pp. 1752-1756, 2010.



Mojtaba Mighani was born in Mashhad, Iran, in September 23, 1983. He received B.Sc. degree in Electrical and Electronic Engineering from Aeronautical University, Tehran, Iran, in 2005 and M.Sc. degrees in Electrical and Telecommunication Engineering from K. N. Toosi University, Tehran, Iran. He is currently working toward the Ph.D. degree in Communication Engineering. Since 2007, he has taught courses in communication circuits, microwave engineering, antenna theory, RADAR, and Fields & Waves in Aeronautical University, Tehran, Iran. His research interests include antenna theory, microwave active circuits, and RF communication links.



Mohammad Akbari was born on February 3, 1983 in Tehran, Iran. He received his B.Sc. degree in Engineering-Telecommunication from University of Bahonar, Kerman, Iran, in 2007 and M.Sc. degrees in Electrical Engineering-Telecommunication from University of Urmia, Urmia, Iran, in 2011. His primary research interests are in antenna design, filters, and microwave components. Since 2011, he has taught courses in microwave engineering, antenna theory, and Fields & Waves, and electromagnetic in Aeronautical University, Tehran, Iran.



Nader Felegari was born in Songhor, Iran 1984. He received his B.S. degree of Electrical Engineering and his M.S. degree of Communication Engineering from the Urmia University, Iran. His primary research interests are in antenna design.

Scattering from Large-Scale Stratified Rough Surfaces using Improved BMIA/CAG

Linfeng He, Liang Lang, Qingxia Li, and Wenchao Zheng

Science and Technology on Multi-Spectral Information Processing Laboratory
Huazhong University of Science and Technology, Wuhan, 430074, China
linfeng_he@mail.hust.edu.cn, l_lang@mail.hust.edu.cn,
qingxia_li@mail.hust.edu.cn, wenchaozheng10@gmail.com

Abstract — A numerical method is presented to analyze the scattering behavior of large-scale stratified rough surfaces. The method improves the banded matrix iterative approach / canonical grid (BMIA/CAG) by adopting some simple formulas to calculate the coupling interactions between different surfaces. Such treatment reduces the complexity of the method at expense of little accuracy when the roughness of surfaces can be ignored compared to the distance between surfaces, and also reduces the computation time by parallel implementation technique. Based on emissivity calculation, the one-dimensional method is proven to be effective for the analysis of some scattering properties. Then the proposed method is compared with the method of moments (MoM) by example of multilayered lunar regolith. Details of numerical results are given and discussed, which provide a guide in the application of the improved method.

Index Terms — Banded matrix iterative approach / canonical grid method (BMIA/CAG), method of moments (MoM), remote sensing, rough surface scattering, stratified rough surfaces.

I. INTRODUCTION

Electromagnetic characteristics of stratified rough surfaces have been studied for many applications in remote sensing, such as lunar exploration [1, 2], buried objects detection [3, 4], ocean observation [5], etc. With the advent of modern computers, it is attractive to study scattering from rough surfaces with fast numerical methods [6].

Based on the method of moments (MoM), the Maxwell equations are converted into matrix equations which can be solved by linear iterative solvers [7]. For the case of stratified rough surfaces, main numerical methods include extended boundary condition method (EBCM) with truncated singular value decomposition (TSVD) [8], forward-backward spectral acceleration (FBSA) [9], the steepest descent fast multipole method (SDFMM) [10] and propagation-inside-layer expansion (PILE) [11] approach. The hybrids of these methods [12] and the parallel implementation technique [13] have been used in some methods to speed up computations. Nevertheless, the computational complexity of SVD in [8] increases rapidly with the size of the matrix; FBSA may fail to converge in lossless cases or for media with large permittivity [9]; the SDFMM requires a depth less than one free-space wavelength to satisfy the quasiplanar structure constraint [10]; the derivation of characteristic matrix of the layer [11] becomes prohibitively challenging when too many interfaces are involved. Besides, there are also some researches on scattering problem from stratified media with a perfect electric conductor (PEC) layer [14]. Their constraints limit the use of the methods for lunar regolith.

The banded matrix iterative approach on a canonical grid (BMIA/CAG) [15, 16] is an efficient method for one-dimensional (1-D) single surface because it requires low dynamic memory and computation time. A multilevel expansion method [16] has been used to improve the BMIA/CAG for surfaces with root mean square (rms) heights up to several wavelengths [17].

However, for stratified rough surfaces, the expanding of coupling interactions between different surfaces is much more complicated than similar operations for a single surface case. The complexity of programming and calculations makes the BMIA/CAG inefficient.

To overcome this limitation, the BMIA/CAG method is improved and generalized to calculate the scattering from 1-D stratified rough surfaces in this paper. For convenience, the improved method is named as generalized BMIA (GBMIA) throughout the paper. In Section II, the principle of the BMIA/CAG is first investigated, and then simplified formulas for the GBMIA are introduced. With these simplifications, the solving of the linear matrix equation in the iterative approach is parallelizable and the computation can be accelerated by the parallel implementation technique, which is shown in Section III. More numerical results and discussion on different models are presented to prove the validity of the GBMIA in Section IV. Remarks are given in Section V.

II. FORMULATION

A. Integral equations

The geometry of 1-D stratified rough surfaces is illustrated in Fig. 1, with N rough surfaces, dividing the space into $N + 1$ layers. The j -th surface S_j is described by the profile $z = f_j(x)$, where $x \in [-L/2, L/2]$, L is the length of the surface. For the j -th layer V_j , the properties are expressed by the complex permittivity ϵ_j and the complex permeability μ_j , and the total field is denoted by ψ_j . Besides, for the j -th layer ($j = 1, \dots, N-1$), let H_j denote the average thickness of the layer.

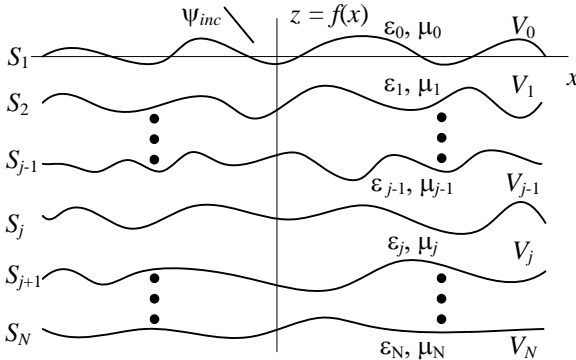


Fig. 1. Schematic diagram of 1-D stratified rough surfaces.

With an incident field ψ_{inc} impinging on S_0 , the double integral equations for the j -th surface S_j can be written as

$$\begin{aligned} & \frac{1}{2} \psi_j(\bar{\mathbf{r}}') - P.V. \int_{S_j} ds \psi_j(\bar{\mathbf{r}}) \hat{\mathbf{n}}_j \cdot \nabla G_j(\bar{\mathbf{r}}, \bar{\mathbf{r}}') \\ & + \int_{S_j} ds G_j(\bar{\mathbf{r}}, \bar{\mathbf{r}}') \hat{\mathbf{n}}_j \cdot \nabla \psi_j(\bar{\mathbf{r}}) \\ & + \int_{S_{j-1}} ds \psi_{j-1}(\bar{\mathbf{r}}) \hat{\mathbf{n}}_{j-1} \cdot \nabla G_j(\bar{\mathbf{r}}, \bar{\mathbf{r}}') \\ & - \int_{S_{j-1}} ds G_j(\bar{\mathbf{r}}, \bar{\mathbf{r}}') \rho_{j,j-1} \hat{\mathbf{n}}_{j-1} \cdot \nabla \psi_{j-1}(\bar{\mathbf{r}}) = 0 \quad \bar{\mathbf{r}}' \in S_j \end{aligned} \quad (1)$$

$$\begin{aligned} & -\frac{1}{2} \psi_j(\bar{\mathbf{r}}') - P.V. \int_{S_j} ds \psi_j(\bar{\mathbf{r}}) \hat{\mathbf{n}}_j \cdot \nabla G_{j+1}(\bar{\mathbf{r}}, \bar{\mathbf{r}}') \\ & + \int_{S_j} ds G_{j+1}(\bar{\mathbf{r}}, \bar{\mathbf{r}}') \rho_{j+1,j} \hat{\mathbf{n}}_j \cdot \nabla \psi_j(\bar{\mathbf{r}}) \\ & + \int_{S_{j+1}} ds \psi_{j+1}(\bar{\mathbf{r}}) \hat{\mathbf{n}}_{j+1} \cdot \nabla G_{j+1}(\bar{\mathbf{r}}, \bar{\mathbf{r}}') \\ & - \int_{S_{j+1}} ds G_{j+1}(\bar{\mathbf{r}}, \bar{\mathbf{r}}') \hat{\mathbf{n}}_{j+1} \cdot \nabla \psi_{j+1}(\bar{\mathbf{r}}) = 0 \quad \bar{\mathbf{r}}' \in S_j \end{aligned} \quad (2)$$

where $\bar{\mathbf{r}}'$ is the position vector of the observation point on S_j and $\bar{\mathbf{r}}$ is that of the source point on the corresponding integral surface. G_j denotes the Green's function in V_j . $P.V.$ represents the principal value integral. $\hat{\mathbf{n}}_j = (-f'_j(x)\hat{\mathbf{x}} + \hat{\mathbf{z}}) / \sqrt{1+(f'_j(x))^2}$, is the normal vector at $(x, f_j(x))$. $\rho_{j+1,j} = \mu_{j+1}/\mu_j$ for transverse electric (TE) wave and $\rho_{j+1,j} = \epsilon_{j+1}/\epsilon_j$ for transverse magnetic (TM) wave.

Specially, for the top surface S_1 , i.e., $j = 1$, integrations on surface S_{j-1} in (1) become the incident field ψ_{inc} . For the bottom surface S_N , i.e., $j = N$, integrations on surface S_{j+1} in (2) go to zero. Thus, the scattering problem from stratified rough surfaces can be described by (1) and (2).

B. MoM implementation

According to the principle of MoM [18], each surface is divided equally into M segments of width $\Delta x = L/M$. Then the integral equations (1) and (2) can be discretized and converted to a linear matrix equation with the form $\bar{\mathbf{Z}} \cdot \bar{\mathbf{X}} = \bar{\mathbf{b}}$, where $\bar{\mathbf{Z}}$ is the coefficient matrix with $2MN \times 2MN$ elements, representing coupling interactions between observation and source points on surfaces; $\bar{\mathbf{b}}$ is a $2MN \times 1$ vector, representing incident fields on surfaces; and $\bar{\mathbf{X}}$ is a $2MN \times 1$ vector, denoting the surface unknowns to be solved.

For a scattering model with N rough surfaces, the coefficient matrix has the form of

$$\bar{\bar{\mathbf{Z}}} = \begin{bmatrix} \bar{\bar{\mathbf{Z}}}_1 & \bar{\bar{\mathbf{Z}}}_{21} & \bar{\mathbf{0}} & \cdots & \bar{\mathbf{0}} \\ \bar{\bar{\mathbf{Z}}}_{12} & \bar{\bar{\mathbf{Z}}}_2 & \bar{\mathbf{Z}}_{32} & \ddots & \vdots \\ \bar{\mathbf{0}} & \bar{\mathbf{Z}}_{23} & \bar{\mathbf{Z}}_3 & \ddots & \bar{\mathbf{0}} \\ \vdots & \ddots & \ddots & \ddots & \bar{\mathbf{Z}}_{N,N-1} \\ \bar{\mathbf{0}} & \cdots & \bar{\mathbf{0}} & \bar{\mathbf{Z}}_{N-1,N} & \bar{\mathbf{Z}}_N \end{bmatrix}_{2MN \times 2MN}, \quad (3)$$

where block matrices are

$$\bar{\bar{\mathbf{Z}}}_i = \begin{bmatrix} \bar{\bar{\mathbf{A}}}_{i-1,i} & \bar{\bar{\mathbf{B}}}_{i-1,i} \\ \rho_{i,i-1} \bar{\bar{\mathbf{A}}}_{i,i} & \bar{\bar{\mathbf{B}}}_{i,i} \end{bmatrix}_{2M \times 2M}, \quad i = 1, 2, \dots, N,$$

$$\bar{\bar{\mathbf{Z}}}_{i+1,i} = \begin{bmatrix} \bar{\mathbf{0}} & \bar{\mathbf{0}} \\ \bar{\mathbf{C}}_{i+1,i} & \bar{\mathbf{D}}_{i+1,i} \end{bmatrix}_{2M \times 2M},$$

$$\bar{\bar{\mathbf{Z}}}_{i,i+1} = \begin{bmatrix} \rho_{i,i-1} \bar{\bar{\mathbf{C}}}_{i,i+1} & \bar{\bar{\mathbf{D}}}_{i,i+1} \\ \bar{\mathbf{0}} & \bar{\mathbf{0}} \end{bmatrix}_{2M \times 2M}, \quad i = 1, 2, \dots, N-1.$$

$\bar{\bar{\mathbf{A}}}_{i,j}$, $\bar{\bar{\mathbf{B}}}_{i,j}$, $\bar{\bar{\mathbf{C}}}_{i,j}$, $\bar{\bar{\mathbf{D}}}_{i,j}$ are $M \times M$ block matrices.

Elements in $\bar{\bar{\mathbf{A}}}_{i,j}$ and $\bar{\bar{\mathbf{C}}}_{i,j}$ have the similar form of (4), while those in $\bar{\bar{\mathbf{B}}}_{i,j}$ and $\bar{\bar{\mathbf{D}}}_{i,j}$ are in the form of (5). The details of expressions for these block matrices can be found in [11].

$$AC(m,n) = \Delta x \cdot H_0^{(1)}(k|\bar{\mathbf{r}}'_m - \bar{\mathbf{r}}_n|), \quad (4)$$

$$BD(m,n) = \Delta x \cdot \frac{ik}{4} \frac{H_1^{(1)}(k|\bar{\mathbf{r}}'_m - \bar{\mathbf{r}}_n|)}{|\bar{\mathbf{r}}'_m - \bar{\mathbf{r}}_n|}, \quad (5)$$

$$\times [f'_n(x_n)(x_n - x_m) - (f_n(x_n) - f_m(x_m))]$$

where k is the wave number in the corresponding layer. $H_0^{(1)}$ and $H_1^{(1)}$ are the zero-order and first-order Hankel functions of the first kind, respectively. An essential difference should be noticed that observation and source points are on the same surface for $\bar{\bar{\mathbf{A}}}_{i,j}$ and $\bar{\bar{\mathbf{B}}}_{i,j}$ while they are on different surfaces for $\bar{\bar{\mathbf{C}}}_{i,j}$ and $\bar{\bar{\mathbf{D}}}_{i,j}$.

C. BMIA/CAG method

The MoM solution is rigorous [19]. However, the memory requirements and computational complexity increase rapidly with the size of $\bar{\bar{\mathbf{Z}}}$. To this problem, the BMIA/CAG solves the matrix equation in an iterative approach, by decomposing each block matrix into two parts. For example, the matrix $\bar{\bar{\mathbf{A}}}$ is decomposed into

$$A^{(s)}(m,n) = \begin{cases} A(m,n) & |m-n| \leq b_w, \\ 0 & |m-n| > b_w \end{cases}, \quad (6)$$

$$\text{and } A^{(w)}(m,n) = \begin{cases} 0 & |m-n| \leq b_w, \\ A(m,n) & |m-n| > b_w \end{cases}, \quad (7)$$

where $1 \leq m, n \leq M$, and b_w is an adjustable parameter and set to be $M/10$ in most cases [15].

Then $\bar{\bar{\mathbf{A}}}^{(s)}$ is a banded matrix which represents strong interaction and the remainder $\bar{\bar{\mathbf{A}}}^{(w)}$ represents the weak interaction part. $\bar{\bar{\mathbf{B}}}$, $\bar{\bar{\mathbf{C}}}$, $\bar{\bar{\mathbf{D}}}$ are decomposed in the same way. Then $\bar{\bar{\mathbf{A}}}^{(s)}$, $\bar{\bar{\mathbf{B}}}^{(s)}$, $\bar{\bar{\mathbf{C}}}^{(s)}$, $\bar{\bar{\mathbf{D}}}^{(s)}$ are grouped to be $\bar{\bar{\mathbf{Z}}}^{(s)}$, and others are separated into $\bar{\bar{\mathbf{Z}}}^{(w)}$.

The matrix equation becomes $\left[\bar{\bar{\mathbf{Z}}}^{(s)} + \bar{\bar{\mathbf{Z}}}^{(w)} \right] \bar{\bar{\mathbf{X}}} = \bar{\mathbf{b}}$

which can be solved by the following iteration [18]

$$\bar{\bar{\mathbf{Z}}}^{(s)} \bar{\bar{\mathbf{X}}}^{(p+1)} = \bar{\mathbf{b}}^{(p)}, \quad (8)$$

where $\bar{\mathbf{b}}^{(p)}$ represents the updated right-hand side with

$$\bar{\mathbf{b}}^{(0)} = \bar{\mathbf{b}}, \quad (9)$$

$$\bar{\mathbf{b}}^{(p)} = \bar{\mathbf{b}} - \bar{\bar{\mathbf{Z}}}^{(w)} \bar{\bar{\mathbf{X}}}^{(p)}. \quad (10)$$

The stopping criterion for the iterative procedure is defined as $\sqrt{\frac{\|\bar{\mathbf{b}}^{(p+1)} - \bar{\mathbf{b}}^{(p)}\|}{\|\bar{\mathbf{b}}^{(0)}\|}} \times 100\%$.

In the BMIA/CAG, the solution to (8) can be solved by taking advantage of the sparsity of $\bar{\bar{\mathbf{Z}}}^{(s)}$, without inverting the full matrix $\bar{\bar{\mathbf{Z}}}$. $\bar{\bar{\mathbf{Z}}}^{(w)}$ is decomposed so that $\bar{\bar{\mathbf{Z}}}^{(w)} \bar{\bar{\mathbf{X}}}^{(p)}$ product can be computed by the fast Fourier transform (FFT), which can avoid the storage of $\bar{\bar{\mathbf{Z}}}^{(w)}$, besides saving the CPU time [18].

D. Decomposition of $\bar{\bar{\mathbf{Z}}}^{(w)}$

To apply the FFT to $\bar{\bar{\mathbf{Z}}}^{(w)} \bar{\bar{\mathbf{X}}}^{(p)}$ product, the $\bar{\bar{\mathbf{Z}}}^{(w)}$ needs to be decomposed in further into a sum of

$$\bar{\bar{\mathbf{Z}}}^{(w)} = \sum_i^{N_Z} \bar{\bar{\mathbf{Z}}}_i^{(w)}, \quad (11)$$

where $\bar{\bar{\mathbf{Z}}}_i^{(w)}$ has the form of $\bar{\bar{\mathbf{T}}}_m \bar{\bar{\mathbf{Z}}}_d \bar{\bar{\mathbf{T}}}_n$. $\bar{\bar{\mathbf{T}}}_m$ is a function of m , and $\bar{\bar{\mathbf{T}}}_n$ is a function of n . $\bar{\bar{\mathbf{Z}}}_d$ is a translationally invariant matrix [18]. N_Z is the number of such matrix.

The decomposition in (11) is equivalent to expand the Hankel functions in (4) and (5) in Taylor series at $z_d = z_0$. For elements in $\bar{\bar{\mathbf{A}}}^{(s)}$,

$$H_0^{(1)}(k\sqrt{x_d^2 + z_d^2}) = \sum_{t=0}^{N_T} a_t(x_d) \cdot \left(\frac{z_d^2 - z_0^2}{x_d^2} \right)^t, \quad (12)$$

where $x_d = |m-n|\Delta x$ is the horizontal distance between the observation and source points, and z_d is the vertical component. N_T is the number of Taylor terms truncated in numerical calculations.

For $\bar{\mathbf{A}}$, all the observation and source points are on the same surface, and z_d is only affected by roughness of the surface. In this case, $z_0 = 0$. By substituting z_d with $f_m(x) - f_n(x)$, the second Taylor term ($t = 1$) in (12), for example, can be written as

$$a_1(x_d) \cdot \left(\frac{z_d}{x_d} \right)^2 = f_m^2(x) \frac{a_1(x_d)}{x_d^2} + 2f_m(x) \frac{a_1(x_d)}{x_d} f_n(x) + \frac{a_1(x_d)}{x_d^2} f_n^2(x) \quad (13)$$

Now, each item on the right side of (13) has the form of $T_m Z_d T_n$, where T_m and T_n are functions of m and n , respectively, and Z_d is only related to $|m-n|$. Let $N(t)$ denote the number of items with the form of $F_m Z_d F_n$ from the t -th Taylor term, then

$$N_Z = \sum_{t=0}^{N_r} N(t) \quad (14)$$

The decomposition of $\bar{\mathbf{B}}^{(w)}$ is similar to that of $\bar{\mathbf{A}}^{(w)}$. However, in case of stratified rough surfaces, The decompositions of $\bar{\mathbf{C}}^{(w)}$ and $\bar{\mathbf{D}}^{(w)}$ are quite more complex for that the observation and source points are on different surfaces and the Hankel functions should be expanded at $z_0 = H_i$ which is the distance between two surfaces. If the first three Taylor terms are used in numerical calculation, N_Z for $\bar{\mathbf{A}}^{(w)}$, $\bar{\mathbf{B}}^{(w)}$, $\bar{\mathbf{C}}^{(w)}$ and $\bar{\mathbf{D}}^{(w)}$ is 9, 27, 21, and 63, respectively. In single surface case, the total number N_Z in BMIA/CAG is 36, while the number will reach to 120 for stratified rough surfaces; and the complexity will grow with more Taylor terms.

E. Generalized BMIA

To reduce the complexity in decomposition of $\bar{\mathbf{C}}^{(w)}$ and $\bar{\mathbf{D}}^{(w)}$, some simpler formulas for $\bar{\mathbf{C}}^{(w)}$ and $\bar{\mathbf{D}}^{(w)}$ are introduced for special applications, which generalizes the BMIA/CAG method so as to study the scattering behavior of stratified rough surfaces.

The vertical component z_d for $\bar{\mathbf{C}}$ and $\bar{\mathbf{D}}$ can be written as

$$z_d = H_i + \delta f(x_m) + \delta f(x_n) = H_i \left(1 + \frac{\delta f(x_m) + \delta f(x_n)}{H_i} \right) \quad (15)$$

where $\delta f(x_m)$ and $\delta f(x_n)$ represent the distances of the observation point and source point to their mean surfaces, respectively.

In many applications, values of $\delta f(x_m)$ and $\delta f(x_n)$ can be ignored compared to H_i . For example, at

the Mare Serenitatis on the Moon, the depth of lunar subsurface can reach several kilometers, while the rms height of the surface is only about one meter [20]. Let $z_d \approx H_i$, then

$$H^{(1)}\left(k\sqrt{x_d^2 + z_d^2}\right) \approx H^{(1)}\left(k\sqrt{x_d^2 + H_i^2}\right) \quad (16)$$

Now, the Hankel function in (16) only depends on x_d , so elements in the matrix on the same diagonal are the same. Then $\bar{\mathbf{C}}$ and $\bar{\mathbf{D}}$ are known as Toeplitz matrices.

In the GBMIA, the decomposing to $\bar{\mathbf{A}}$ and $\bar{\mathbf{B}}$ is the same as that done in the BMIA/CAG. For $\bar{\mathbf{C}}$ and $\bar{\mathbf{D}}$, observation and source points are on different surfaces. Taking the thickness of layers into account, the whole matrices $\bar{\mathbf{C}}$ and $\bar{\mathbf{D}}$ are considered as weak part, i.e. $\bar{\mathbf{C}}^{(w)} = \bar{\mathbf{C}}$ and $\bar{\mathbf{D}}^{(w)} = \bar{\mathbf{D}}$, the product of which and vector can be computed by the FFT directly. Now the number N_Z for $\bar{\mathbf{C}}^{(w)}$ or $\bar{\mathbf{D}}^{(w)}$ is only one, which is greatly reduced.

In GBMIA, the strong part $\bar{\mathbf{Z}}^{(s)}$ for stratified rough surfaces is now reduced to

$$\bar{\mathbf{Z}}^{(s)} = \begin{bmatrix} \bar{\mathbf{Z}}_1^{(s)} & \bar{\mathbf{0}} & \dots & \bar{\mathbf{0}} \\ \bar{\mathbf{0}} & \bar{\mathbf{Z}}_2^{(s)} & \ddots & \vdots \\ \vdots & \ddots & \ddots & \bar{\mathbf{0}} \\ \bar{\mathbf{0}} & \dots & \bar{\mathbf{0}} & \bar{\mathbf{Z}}_N^{(s)} \end{bmatrix} \quad (17)$$

From the form of $\bar{\mathbf{Z}}^{(s)}$ in (17), the solving to (8) can be divided into N linear equations with coefficient matrices $\bar{\mathbf{Z}}_i^{(s)}$, which are sparse banded matrices with small scale. What's more, these equations are independent with each other, so solving to them can be implemented in parallel, which is helpful to save the computation time.

Let $\bar{\mathbf{X}} = [\bar{\mathbf{X}}_1^T, \bar{\mathbf{X}}_2^T, \dots, \bar{\mathbf{X}}_{2N}^T]^T$, and $\bar{\mathbf{b}} = [\bar{\mathbf{b}}_1^T, \bar{\mathbf{b}}_2^T, \dots, \bar{\mathbf{b}}_{2N}^T]^T$, the updating equations to (8) are

$$\bar{\mathbf{b}}_1^{(p+1)} = \bar{\boldsymbol{\psi}}_{inc} - \bar{\mathbf{A}}_{0,1} \bar{\mathbf{X}}_1^{(p)} - \bar{\mathbf{B}}_{0,1} \bar{\mathbf{X}}_2^{(p)} \quad (18)$$

$$\bar{\mathbf{b}}_{2n}^{(p+1)} = \bar{\mathbf{0}} - \rho_{n,n-1} \bar{\mathbf{A}}_{n,n} \bar{\mathbf{X}}_{2n-1}^{(p)} - \bar{\mathbf{B}}_{n,n} \bar{\mathbf{X}}_{2n}^{(p)} - \bar{\mathbf{C}}_{n+1,n} \bar{\mathbf{X}}_{2n+1}^{(p)} - \bar{\mathbf{D}}_{n+1,n} \bar{\mathbf{X}}_{2n+2}^{(p)} \quad n = 1, 2, \dots, N-1, \quad (19)$$

$$\bar{\mathbf{b}}_{2n+1}^{(p+1)} = \bar{\mathbf{0}} - \rho_{n,n-1} \bar{\mathbf{C}}_{n,n+1} \bar{\mathbf{X}}_{2n-1}^{(p)} - \bar{\mathbf{D}}_{n,n+1} \bar{\mathbf{X}}_{2n}^{(p)} - \bar{\mathbf{A}}_{n,n+1} \bar{\mathbf{X}}_{2n+1}^{(p)} - \bar{\mathbf{B}}_{n,n+1} \bar{\mathbf{X}}_{2n+2}^{(p)} \quad n = 1, 2, \dots, N-1, \quad (20)$$

$$\bar{\mathbf{b}}_{2N}^{(p+1)} = \bar{\mathbf{0}} - \rho_{N,N-1} \bar{\mathbf{A}}_{N,N} \bar{\mathbf{X}}_{2N-1}^{(p)} - \bar{\mathbf{B}}_{N,N} \bar{\mathbf{X}}_{2N}^{(p)} \quad (21)$$

III. EFFICIENCY EVALUATION

Memory requirement and computation time are two important criteria to assess a numerical method. The memory requirement depends on the number of non-zero elements in $\bar{\mathbf{Z}}$. For the MoM, $\bar{\mathbf{Z}}$ is a full matrix containing $4(2N-1)M^2$ elements, which will all be calculated and stored. In the BMIA/CAG, only non-zero elements in $\bar{\mathbf{Z}}^{(s)}$ is necessary, the number of which is equal to $4(2N-1)[M+(b_w-1)(2M-b_w)]$. In the GBMIA, the number of non-zero elements in $\bar{\mathbf{Z}}^{(s)}$ decreases to $4N[M+(b_w-1)(2M-b_w)]$. For the sake of illustration, the comparison of these three methods for different surface number N is listed in Table 1, with $M = 1000$, $b_w = M/10$.

Table 1: Number of non-zero elements (in million)

N	MoM	BMIA/CAG	GBMIA
1	4	0.7564	0.7564
2	12	2.2692	1.5128
3	20	3.782	2.2692
4	28	5.2948	3.0256
5	36	6.8076	3.782
6	44	8.3204	4.5384
7	52	9.8332	5.2948
8	60	11.346	6.0512
9	68	12.8588	6.8076
10	76	14.3716	7.564

From Table 1, the number of non-zero elements in GBMIA need to be calculated and stored is the least. When $N = 3$, the number to be stored in the GBMIA is only about 11% of that in the MoM, and 60% of that in the BMIA/CAG, which is a considerable saving in memory requirement and matrix filling time. This advantage becomes more obvious as N increases. The same conclusion can be obtained for different values of M .

To avoid the complexity of implementing BMIA/CAG for stratified rough surfaces, we evaluate the computation time of GBMIA and BMIA/CAG by two parameters: asymptotic convergence rate (R) [21] and time per iteration (T). For $\left[\bar{\mathbf{Z}}^{(s)} + \bar{\mathbf{Z}}^{(w)} \right] \cdot \bar{\mathbf{X}} = \bar{\mathbf{b}}$, the iteration matrix is defined as

$$\bar{\mathbf{Q}} = \left(\bar{\mathbf{Z}}^{(s)} \right)^{-1} \cdot \bar{\mathbf{Z}}^{(w)}. \quad (22)$$

For the iterative approach to converge, the spectral radius of $\bar{\mathbf{Q}}$ must be less than 1, i.e. $\rho(\bar{\mathbf{Q}}) < 1$. Then the asymptotic convergence rate is $R = -\log_{10}(\rho(\bar{\mathbf{Q}}))$, and the speedup (G) in computation time is evaluated by the ratio of the product of $1/R$ and T in BMIA/CAG over that in GBMIA. For several pairs of N and M , GBMIA and BMIA/CAG are compared on a standard personal computer with MATLAB, and values of R and T are shown in Table 2.

Table 2: Computation time evaluation

N	M	BMIA/CAG		GBMIA		G
		R	T (sec.)	R	T (sec.)	
2	600	0.35	0.7430	0.34	0.3958	1.82
	900	0.51	3.9665	0.47	0.7310	5.00
	1200	0.57	6.3811	0.47	1.2227	4.30
3	600	0.34	1.5818	0.31	0.5051	2.86
	900	0.49	5.4874	0.33	0.8420	4.39
	1200	0.50	17.055	0.30	1.5145	6.76
4	600	0.37	2.5300	0.31	0.6739	3.15
	900	0.33	10.488	0.30	1.1253	8.47
	1200	--	93.196	--	1.7155	--

From Table 2, due to the simplifications in $\bar{\mathbf{Z}}^{(s)}$, the convergence rate decreases a little in GBMIA. However, there is a significant reduce in the time per iteration. As a result, the computation time in GBMIA is improved, and the overall speedup increases with N and M . When $N = 4$ and $M = 900$, the speedup reaches about 8.47.

For the case of $N = 4$ and $M = 1200$, although the convergence rate cannot be calculated with our computer, there is a surprising improvement on the time per iteration. Besides the utility of the parallel calculation in GBMIA, immoderate memory consuming in BMIA/CAG is also an important factor affecting the computation time.

These results show that GBMIA is more efficient and suitable for studying scattering problem of large-scale stratified surfaces.

IV. NUMERICAL RESULTS

The solution of surface integral equations obtained by using the MoM has been the standard for checking the validity of other numerical approaches [22]. In this section, the multilayered lunar regolith is taken as an example of stratified

rough surfaces. Before the verification of the GBMIA with MoM, it is necessary to verify that surface emissivity calculated by MoM with 1-D surface model is reliable.

A. Validation of MoM

In [1], the reflectivity for Monte Carlo (MC) realized two-dimensional (2-D) lunar surface is calculated with the observation direction of 0° , and the average reflectivity of ten MC realizations in total is 0.0619 in TE case. To validate the MoM solutions, a simple two-layer model composed of free space and lunar soil, with $\mu_1 = \mu_0$, and $\varepsilon_1 = 2.7+0.01i$ in [1] is used here.

In this simulation, $L = 200\lambda$, where λ is the wavelength. A Thorsos tapered wave [23] is chosen as the incident wave, with $g = L/8$. The interface between free space and lunar soil is a Gaussian rough surface, with a small rms height of $h = 0.04\lambda$ and the correlation length of $l = 0.4\lambda$, in order that the surface emissivity obtained by the MoM can also be compared with the analytical small perturbation method (SPM) solution. Emissivities of the 1-D lunar model obtained at different incident angles are plotted in Fig. 2. The MoM has a good agreement with SPM solutions on a wide range of incident angles, in both TE and TM case.

As indicated in Fig. 2, the emissivity at the direction of 0° in TE case is 0.9331, which is corresponding to the reflectivity of 0.0669, very close to 0.0619 in [1]. Although some phenomena, such as depolarization are inherently for 2-D rough surface and cannot be observed using 1-D methods [19], the comparison indicates that 1-D method is still efficient to analyze scattering behavior, such as emissivity.

B. GBMIA comparison with MoM

Different models are now considered to compare the GBMIA method with the MoM. The emissivity calculated by GBMIA is denoted by e_{GBMIA} , and that obtained from the MoM is e_{MoM} . The relative error $|e_{\text{GBMIA}} - e_{\text{MoM}}|/e_{\text{MoM}}$ is used to assess the accuracy of the proposed method. In this paper, attentions are given to the efficiency of

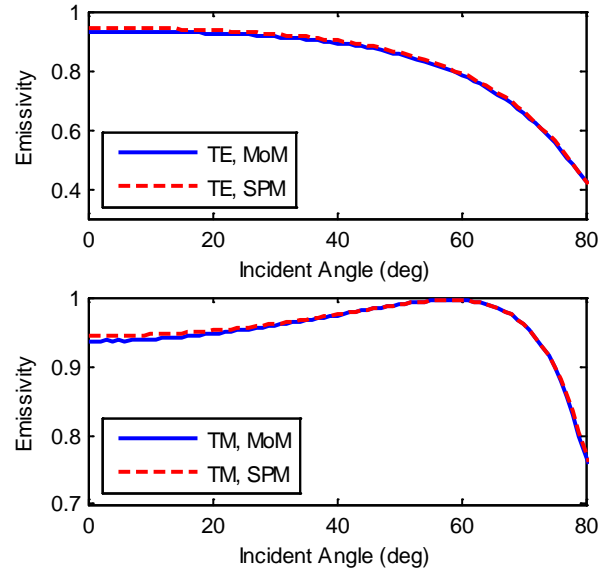


Fig. 2. Comparison of emissivity between MoM and SPM.

the GBMIA on multilayered medium, and the improvement by the multilevel expansion method for large rms heights will not be addressed here.

In this example, a three-layer model is used, composed of free space, lunar soil, and lunar rock, with $\mu_1 = \mu_2 = \mu_0$, and $\varepsilon_1 = 2.42*(1+0.00486i)$, $\varepsilon_2 = 7.8*(1+0.056i)$ [24]. $L = 40\lambda$, and the incident angle is 30° . Two interfaces are both Gaussian rough surfaces with the same roughness parameters. The correlation length $l = \lambda$, and different rms heights h ($0, 0.1\lambda, 0.2\lambda, 0.3\lambda$) are considered. The layer thickness H varies from λ to 30λ , and 20 realizations are generated for each thickness. The first three Taylor expansion terms are used and the residual error is set at 0.01.

The emissivity errors of GBMIA are shown in Fig. 3 for the TM case. From these curves, the emissivities of GBMIA are exactly the same as that of MoM for flat surfaces. For rough surfaces, the error diminishes as a whole, with H increasing, despite some small undulations; and the error decreases more quickly for surfaces with smaller rms height. For this three-layer model, the relative emissivity error by the GBMIA can be controlled below 1% when the thickness of lunar soil reaches 12λ .

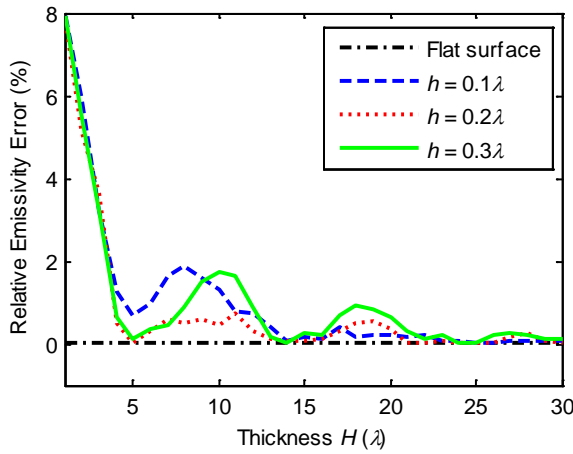


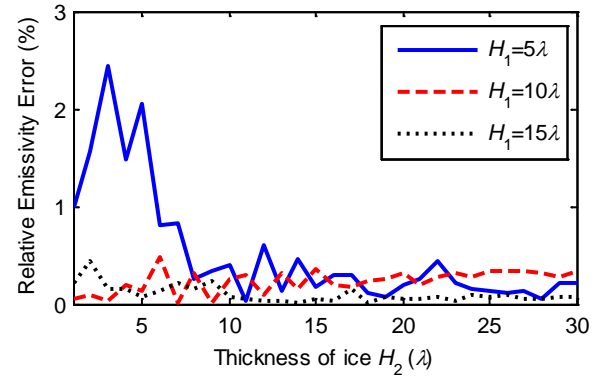
Fig. 3. Relative emissivity error between GBMIA and MoM for three-layer model versus the thickness of layer.

Ice deposits at the Lunar South Pole is an issue of diversity [2]. To estimate effects of possible ice deposit on scattering from lunar regolith, a lunar model containing ice is necessary. As an example to validate the GBMIA for a four-layer model, a layer of ice, with the permittivity of $3.2*(1+0.0035i)$ [24], is added between the lunar soil and rock layers. For different thicknesses of lunar soil ($H_1 = 5\lambda, 10\lambda, 15\lambda, 20\lambda, 25\lambda, 30\lambda$), the thickness of ice (H_2) changes from λ to 30λ . The rms height of surfaces is chosen as 0.1λ , and other parameters are the same as before. The errors for TM case are plotted in Fig. 4. In general, the error decreases with the increasing of H_1 and H_2 , and the thickness of upper layer are more important on accuracy than that of lower layer. When the thickness of lunar soil is larger than 10λ , the error will not exceed 1% even with a thin ice layer.

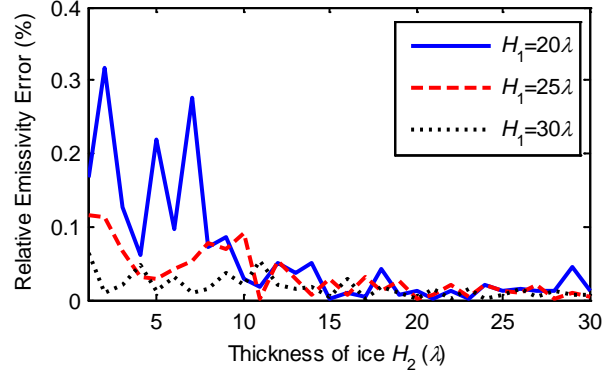
V. CONCLUSION

The BMIA/CAG method is improved and generalized to investigate the electromagnetic scattering from large-scale stratified rough surfaces in case that the distance between two surfaces is very large compared to the roughness.

Comparing to the original BMIA/CAG, the GBMIA method reduces the complexity of decomposing coupling interactions between points on different surfaces. With the reduction, there is a good memory saving in the GBMIA. What's more important, the coefficient matrix in the GBMIA is a block diagonal matrix, and the solving to the matrix equation can be parallelizable. With the parallel implementation technique, the GBMIA has a significant speedup in computation time.



(a)



(b)

Fig. 4. Relative emissivity error between GBMIA and MoM for four-layer model versus different layer thickness: (a) $H_1 = 5\lambda, 10\lambda, 15\lambda$; (b) $H_1 = 20\lambda, 25\lambda, 30\lambda$.

These advantages make the GBMIA be suitable for applications in large-scale problems of stratified rough surfaces scattering.

With simplified formulas, the computational error is unavoidable. In numerical simulations, the MoM solution is first shown to be reliable on emissivity calculation. Then, the accuracy of the GBMIA is estimated by comparisons with the MoM, taking the multilayered lunar regolith as an example. The calculated relative emissivity error is below 1%, when the thickness of lunar soil is larger than about twelve free-space wavelengths.

Although only lunar models are used in numerical simulations, the proposed method can be used for other applications with similar structures.

ACKNOWLEDGMENT

This work was supported in part by the National High Technology Research and Development Program of China (863 Program) under Grant 2010AA122204, and in part by the National Natural Science Foundation of China under Grant 41001195.

REFERENCES

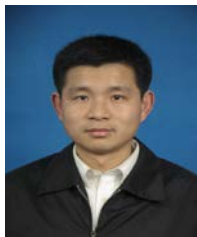
- [1] Y. Q. Jin, and W. Z. Fa, "The Modeling Analysis of Microwave Emission from Stratified Media of Nonuniform Lunar Cratered Terrain Surface for Chinese Chang-E 1 Observation," *IEEE Geosci. Remote Sens. Lett.*, vol. 7, no. 3, pp. 530-534, Jul. 2010.
- [2] W. G. Zhang, J. S. Jiang, H. G. Liu, X. H. Zhang, D. H. Zhang, D. H. Li, and C. D. Xu, "Distribution and Anomaly of Microwave Emission at Lunar South Pole," *Sci. China Earth Sci.*, vol. 53, no. 3, pp. 465-474, Mar. 2010.
- [3] F. Delbary, K. Erhard, R. Kress, R. Potthast, and J. Schulz, "Inverse Electromagnetic Scattering in a Two-Layered Medium with an Application to Mine Detection," *Inverse Probl.*, vol. 24, no. 1, pp. 015002-1, Feb. 2008.
- [4] K. P. Prokopydis and T. D. Tsiboukis, "Modeling of Ground-Penetrating Radar for Detecting Buried Objects in Dispersive Soils," *Appl. Comput. Electromagn. Soc. J.*, vol. 22, no. 2, pp. 287-294, Jul. 2007.
- [5] O. Kilic, "A Discrete Random Medium Model for Electromagnetic Wave Interactions with Sea Spray," *Appl. Comput. Electromagn. Soc. J.*, vol. 23, no. 3, pp. 286-291, Sep. 2008.
- [6] L. Zhou, L. Tsang, V. Jandhyala, Q. Li, and C. H. Chan, "Emissivity Simulations in Passive Microwave Remote Sensing with 3-D Numerical Solutions of Maxwell Equations," *IEEE Trans. Geosci. Remote Sens.*, vol. 42, no. 8, pp. 1739-1748, Aug. 2004.
- [7] N. Nakashima, S. Fujino, and M. Tateiba, "Performance Evaluation of State-of-the-Art Linear Iterative Solvers Based on IDR Theorem for Large Scale Electromagnetic Multiple Scattering Simulations," *Appl. Comput. Electromagn. Soc. J.*, vol. 26, no. 1, pp. 37-44, Jan. 2011.
- [8] C.-H. Kuo and M. Moghaddam, "Scattering from Multilayer Rough Surfaces Based on the Extended Boundary Condition Method and Truncated Singular Value Decomposition," *IEEE Trans. Antennas Propag.*, vol. 54, no. 10, pp. 2917-2929, Oct. 2006.
- [9] C. D. Moss, T. M. Grzegorzcyk, H. C. Han, and J. A. Kong, "Forward-Backward Method with Spectral Acceleration for Scattering from Layered Rough Surfaces," *IEEE Trans. Antennas Propag.*, vol. 54, no. 3, pp. 1006-1016, Mar. 2006.
- [10] M. El-Shenawee, "Polarimetric Scattering from Two-Layered Two-Dimensional Random Rough Surfaces With and Without Buried Objects," *IEEE Trans. Geosci. Remote Sens.*, vol. 42, no. 1, pp. 67-76, Jan. 2004.
- [11] N. Déchamps, N. De Beaucoudrey, C. Bourlier, and S. Toutain, "Fast Numerical Method for Electromagnetic Scattering By Rough Layered Interfaces: Propagation-Inside-Layer Expansion Method," *J. Opt. Soc. Am. A*, vol. 23, no. 2, pp. 359-369, Feb. 2006.
- [12] Z. N. Jiang, Z. H. Fan, D. Z. Ding, R. S. Chen, and K. W. Leung, "Preconditioned MDA-SVD-MLFMA for Analysis of Multi-Scale Problems," *Appl. Comput. Electromagn. Soc. J.*, vol. 25, no. 11, pp. 914-925, Nov. 2010.
- [13] M. El-Shenawee, C. Rappaport, D. Jiang, W. Meleis, and D. Kaeli, "Electromagnetics Computations using the MPI Parallel Implementation of the Steepest Descent Fast Multipole Method (SDFMM)," *Appl. Comput. Electromagn. Soc. J.*, vol. 17, no. 2, pp. 112-122, Jul. 2002.
- [14] S. Tian, Z. Li, C. Q. Gu, and D. P. Ding, "Equivalent Electromagnetic Currents on Infinite Stratified Homogeneous Bi-Anisotropic Media Backed by a PEC Layer," *Appl. Comput. Electromagn. Soc. J.*, vol. 26, no. 3, pp. 206-216, Mar. 2011.
- [15] L. Tsang, C. H. Chan, K. Park, and H. Sangani, "Monte-Carlo Simulations of Large-Scale Problems of Random Rough Surface Scattering and Applications to Grazing Incidence with the BMIA/Canonical Grid Method," *IEEE Trans. Antennas Propag.*, vol. 43, no. 8, pp. 851-859, Aug. 1995.
- [16] C. H. Chan, L. Tsang, and Q. Li, "Monte Carlo Simulation of Large-Scale One-Dimensional Random Rough-Surface Scattering at Near-Grazing Incidence: Penetrable Case," *IEEE Trans. Antennas Propag.*, vol. 46, no. 1, pp. 142-149, Jan. 1998.
- [17] N. Déchamps, and C. Bourlier, "Electromagnetic Scattering from a Rough Layer: Propagation-Inside-Layer Expansion Method Combined to an Updated BMIA/CAG Approach," *IEEE Trans. Antennas Propag.*, vol. 55, no. 10, pp. 2790-2802, Oct. 2007.
- [18] L. Tsang, J. A. Kong, K.-H. Ding, and C. O. Ao, *Scattering of Electromagnetic Waves: Numerical Simulations*, Wiley, New York, 2001.
- [19] K. F. Warnick and W. C. Chew, "Numerical Simulation Methods for Rough Surface Scattering," *Waves Random Media*, vol. 11, no. 1, pp. R1-R30, Jan. 2001.
- [20] T. Kobayashi, H. Oya, and T. Ono, "A-Scope Analysis of Subsurface Radar Sounding of Lunar Mare Region," *Earth Planets Space*, vol. 54, no. 10, pp. 973-982, Oct. 2002.
- [21] Y. Du and J. A. Kong, "Application of Stochastic Second-Degree Method to Electromagnetic Scattering from Randomly Rough Surfaces,"

Electron. Lett., vol. 43, no. 23, pp. 1244-1246, Nov. 2007.

- [22] K. Pak, L. Tsang, and J. Johnson, "Numerical Simulations and Backscattering Enhancement of Electromagnetic Waves from Two-Dimensional Dielectric Random Rough Surfaces with the Sparse-Matrix Canonical Grid Method," *J. Opt. Soc. Am. A*, vol. 14, no. 7, pp. 1515-1529, Jul. 1997.
- [23] E. I. Thorsos, "The Validity of the Kirchhoff Approximation for Rough Surface Scattering using a Gaussian Roughness Spectrum," *J. Acous. Soc. Am.*, vol. 83, no. 1, pp. 78-92, Jan. 1988.
- [24] Z. G. Meng, S. B. Chen, E. Osei, Z. J. Wang, and T. F. Cui, "Research on Water Ice Content in Cabeus Crater using the Data from the Microwave Radiometer OnBoard Chang'e-1 Satellite," *Sci. China Phys. Mech. Astron.*, vol. 53, no. 12, pp: 2172-2178, Dec. 2010.



Linfeng He received the B.S., and M.S. in Department of Electronics and Information, Huazhong University of Science and Technology, Wuhan, China, in 2006, 2008, respectively. He is presently a Ph.D. candidate in the Department of Electronics and Information, Huazhong University of Science and Technology, Wuhan, China. His research interests include microwave remote sensing, and computational electromagnetics.



Liang Lang received the Ph.D. degree in the Electromagnetic Field and Microwave Technology from Huazhong University of Science and Technology, Wuhan, China, in 2009. He is presently an associate professor in the Department of Electronics and Information Engineering, Huazhong University of Science and Technology. The focus of his research was electromagnetic simulations and microwave remote sensing.



Qingxia Li received the B.S., M.S., and Ph.D. degree in Department of Electronics and Information, Huazhong University of Science and Technology, Wuhan, China, in 1987, 1990, 1999, respectively. He is presently a professor in the Department of Electronics and Information, Huazhong University of Science and Technology, Wuhan, China. His research interests include microwave remote sensing, electromagnetics, and antenna array.



Wenchao Zheng received the B.S. from Xi'an institute of Posts and Telecommunications, Xi'an, China, in 2008 and the M.S. from Wuhan Research institute of Posts and Telecommunications, Wuhan, China in 2011. He is currently working toward the Ph.D. degree in Huazhong University of Science and Technology, Wuhan, China. His research interests include microwave remote sensing and scattering of electromagnetic waves.

Impact of Composite Materials on the Shielding Effectiveness of Enclosures

W. Abdelli^{1,2}, X. Mininger¹, L. Pichon¹, and H. Trabelsi²

¹Laboratoire de Génie Electrique de Paris, UMR 8507 CNRS, SUPELEC, Université Paris-Sud
Université Pierre et Marie Curie, 11 rue Joliot-Curie, 91192 Gif-sur-Yvette, France
wassim.abdelli@lgep.supelec.fr, xavier.mininger@lgep.supelec.fr, lionel.pichon@lgep.supelec.fr

²Laboratoire des Circuits et Systèmes Electroniques à Hautes Fréquences, Faculté des Sciences de Tunis
Université Tunis El Manar, Campus universitaire El Manar, 2092 Tunis, Tunisie
hichem.trabelsi@fst.rnu.tn

Abstract — This paper investigates and compares the electromagnetic behavior of different shielding enclosures built with composite panels (dielectric materials with conducting inclusions, carbon-fiber, fiberglass, conductive materials). The numerical model is based on a full wave finite element method taking into account the geometrical details of the walls and avoiding the use of the classical equivalent layer approach. A 2D composite enclosure with two wall structures is modeled: fiber rods shielding and metal screen shielding. Impacts of conductivity and rod diameter on the shielding effect are investigated. Concerning metal screen, the shielding effectiveness is studied for different metals with the same mass, leading to identify the most effective metal. The influence of the angle of incidence and the number of apertures is also studied. Finally, a comparison is performed considering the same mass of the two composite wall structures, each composed of fiberglass and carbon fiber.

Index Terms — Composite materials, finite element analysis, shielding effectiveness.

I. INTRODUCTION

Advanced composite materials become widespread in the aerospace, aircraft industries [1] and wireless communications [2]. They are typically composed by a resin matrix reinforced by high strength fibers, such as graphite, boron, glass, or carbon. With respect to metals, these materials

offer lower weight, higher stiffness and strength, lower corrosion etc. Despite these advantages, composite materials are not as electrically conductive as traditional metallic ones. The shielding effectiveness of composite structures is strongly affected by the fiber-composition fraction or percentage. So these composite materials may have a significant impact on the electromagnetic compatibility constraints.

Generally, electromagnetic modeling studies of composites materials have been carried out concerning the characterization of the reflection, transmission, and shielding properties of such materials, with reference to canonical configurations having either planar or cylindrical symmetries [3-6]. In these analyses, the composite is replaced by an equivalent layer model where the composite is an effective medium. This makes easier the electromagnetic modeling with analytical or numerical methods.

For the packaging of practical structures, the performance of a shielding enclosure is quantified by its shielding effectiveness (SE), defined as the ratio of field strength in the presence and absence of the enclosure. The value of SE is closely related to the dimensions of the enclosure and the possible resonance effect for specific frequency ranges. The variation of SE versus frequency can be efficiently evaluated with a convenient modeling technique like the method of moments (MoM) [7-9], the Fourier transform and the mode-matching technique (MMT) [10], the finite-difference time-domain method (FDTD) [11-15], the transmission-

line modeling method (TLM) [16, 17] or the finite element method (FEM) [18-20]. Most of these studies are devoted to metallic enclosures. They do not investigate the impact of new composite materials on the frequency response of the structure.

The aim of this paper is to emphasize the impact of composite materials used for shielding effectiveness of enclosures. It shows with an adequate finite element modeling that composite materials modify the wide band frequency response of the structure when compared to a metallic one. The analysis is performed for a 2D enclosure made of the carbon fiber composite material described in [4]. In order to avoid the classical assumption relevant to the use of an equivalent layer model, the finite element approach takes into account the fine features of the composite. The computational model clearly underlines the influence of the diameter and the electrical conductivity of the rods on the resonances of the SE. Another composite screen constituted with a metal sheet embedded in dielectric materials is also studied for comparison.

Shielding Effectiveness is defined as the ratio (in decibel unit) of the total field existing in the presence of the enclosure to the incident field:

$$SE_{dB} = -10 \log_{10} \left(\frac{P^t}{P^i} \right) = -20 \log_{10} \left(\frac{E^t}{E^i} \right), \quad (1)$$

where P^i and P^t are respectively the incident and transmitted electromagnetic power, also for the electric field E .

II. ELECTROMAGNETIC PROBLEM AND VALIDATION OF THE MODEL

The transverse magnetic (TM) case is considered where the incident electric field and scattered electric field have only one component in the z direction denoted E^i and E^s , respectively.

The total electric field E^t ($E^t = E^i + E^s$) satisfies:

$$\operatorname{div} \left(\frac{1}{\mu} \operatorname{grad} E^t \right) + (\epsilon \omega^2 - i \sigma \omega) E^t = 0. \quad (2)$$

Consider the 2D scattering of a plane wave by a 2D enclosure. The shape of the studied enclosure is described in [10-18] (Fig. 1).

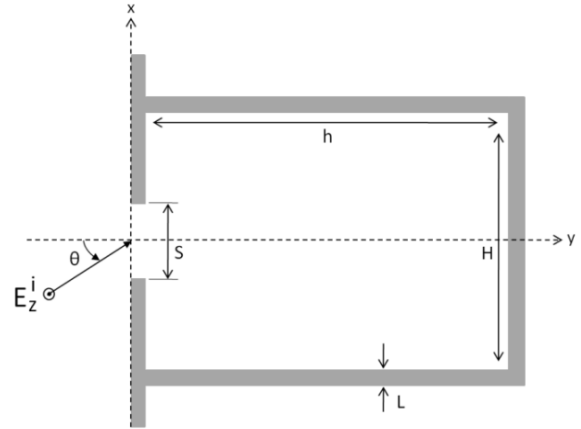


Fig. 1. 2D enclosure with $h=50$ cm, $H=40$ cm, $S=10$ cm, $L=0.4$ cm, $\theta=0^\circ$.

Figure 2 illustrates a shielding composite wall where a thin copper screen ($\mu_r = 1$; $\epsilon_r = 1$; $\sigma = 58 \cdot 10^6$ S/m; $e = 1$ mm) is inserted in a dielectric resin with fiberglass reinforcements ($\mu_r = 1$; $\epsilon_r = 4.3$; $\sigma = 10^{-11}$ S/m; $L_1 = L_2 = 1.5$ mm).

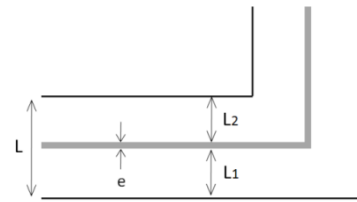


Fig. 2. Composite walls with copper screen shield and fiberglass reinforcements; $L = 4$ mm, $L_1 = L_2 = 1.5$ mm, $e = 1$ mm of copper.

The composite enclosure is illuminated by a plane wave in a frequency range between 100 MHz and 1.1 GHz. The shielding effectiveness is computed inside the enclosure on a line normal to the aperture, at the center, when the incident plane wave is x -directed. The computational domain is truncated by perfectly matched layers (PMLs). The results from the finite element method are compared to analytical formulae from [10] and experimental measurements [10, 18], obtained in the same conditions (geometry, plane wave...), but with a perfect electric conductor (PEC). The experimental process consists in placing a monopolar probe into the shielded enclosure to measure the inner field strength. The measurements were performed inside an anechoic chamber [18]. Results are shown in Fig. 3.

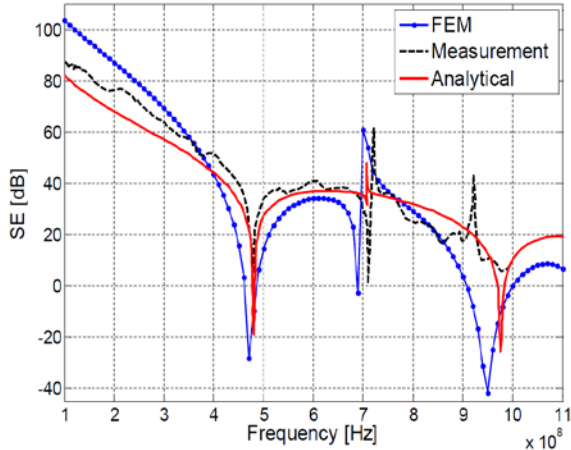


Fig. 3. Comparison of SE for different walls.

FEM results are in good concordance with the available analytical solution for 2D composite enclosure. Moreover, comparison of these results with those of experiments also shows good agreement, despite small shifts in inverted peaks (dips), which are due to the fact that the inner surface surrounded by the metal is a bit greater in the composite enclosure, considering the transparency of the fiberglass relative to the fields. This comparison justifies the use of FEM to simulate composite behavior in the following study. Two kinds of composite structure are next considered.

III. COMPOSITE WALL WITH FIBER RODS SHIELD

The walls include fiber rods ($\mu_f = 1$, $\sigma_f, \varepsilon_f = 4$) embedded in a dielectric resin which is fiberglass ($\mu_d = 1$, $\sigma_d = 10^{-11}$ S/m, $\varepsilon_d = 5.5$) (Fig. 4).

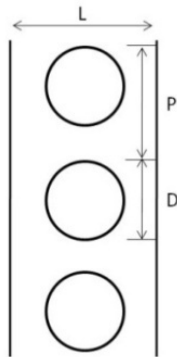


Fig. 4. Composite wall with fiber rods shield and fiberglass reinforcements; $L = 10$ mm, $D = 4$ mm, $P = 8$ mm.

Figure 5 shows the variation of SE versus the rod conductivity up to 1.1 GHz. For high values of conductivities the resonance peaks correspond to the theoretical values obtained in the case of a closed cavity. It can be pointed out that for conductivity lower than 10 S/m, the negative shielding near the resonances disappears, but SE is significantly reduced for those values. This can be explained by the fact that a low value of the conductivity leads to a low value of reflection loss inside the enclosure, thus minimizing the effect of resonances.

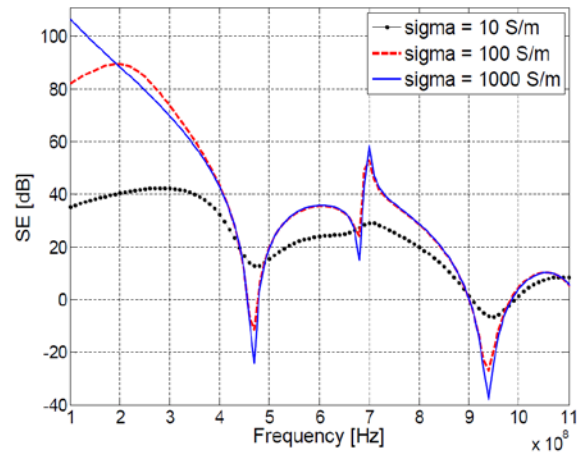


Fig. 5. Shielding effectiveness considering different conductivities of the rods.

One of the main advantages of composite materials is their low weight. The impact of the rod diameter D on the SE, directly related to the weight of the enclosure, is now investigated. Here, we consider that $P = 20$ mm and $\sigma = 1000$ S/m.

Figure 6 clearly shows that SE is significantly reduced when using rods with small diameter. In this case, the shielding effect is mainly governed by the ratio between the period of the rods and the wavelength.

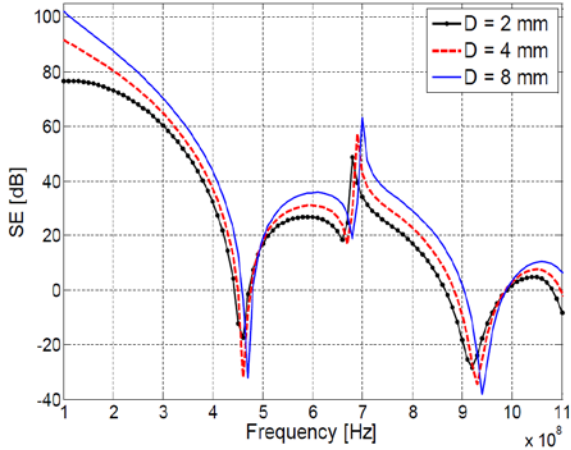


Fig. 6. Shielding effectiveness for different diameters of the rods.

IV. COMPOSITE WALL WITH METAL SCREEN SHIELD

The second structure is composed of walls, where a thin metal screen is inserted in resin dielectric fiberglass reinforcements.

A. Impact of the composite material

Figure 7 shows the variation of SE for several kinds of metallic screens with a same mass for the whole wall. In order to identify the most effective metal in term of electromagnetic shielding, the mass criterion seems to be suitable.

- Aluminum screen structure :

$$\mu_r = 1 ; \epsilon_r = 1 ; \sigma = 38 \cdot 10^6 \text{ S/m} ; \rho = 2700 \text{ kg/m}^3 .$$

- Copper screen structure :

$$\mu_r = 1 ; \epsilon_r = 1 ; \sigma = 58 \cdot 10^6 \text{ S/m} ; \rho = 8920 \text{ kg/m}^3$$

- Iron screen structure :

$$\mu_r = 400 ; \epsilon_r = 1 ; \sigma = 10.3 \cdot 10^6 \text{ S/m} ; \rho = 7860 \text{ kg/m}^3$$

The aluminum presents an efficiency slightly greater than other metals, in spite of its lower conductivity ($38 \cdot 10^6 \text{ S/m}$) comparing with that of copper ($58 \cdot 10^6 \text{ S/m}$). This can be explained by the fact that from a certain very high value of the conductivity, the thickness of the material will mainly influence the increase of the shielding effectiveness.

B. Impact of angle of incidence

The variation in the angle of incidence (θ on Figure 1) also changes the shielding effectiveness (Fig. 8). In the previous simulations, the wave propagates initially to the shielding enclosure with an angle of incidence $\theta = 0^\circ$. It is shown that it corresponds to the worst case, because the incident wave penetrates directly into the aperture.

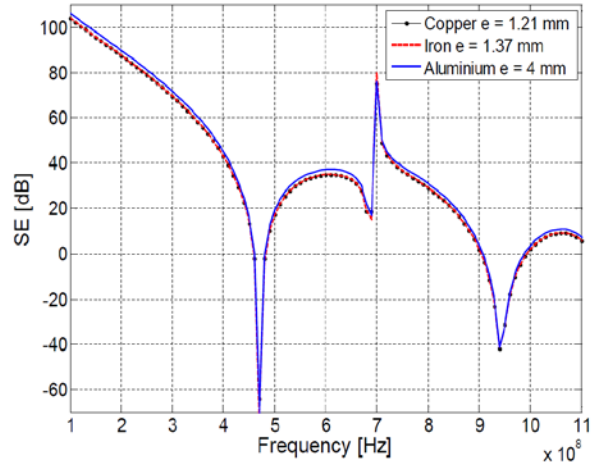


Fig. 7. Shielding effectiveness for various kinds of composite walls metal screen with equal mass; $L_1 = L_2 = 3 \text{ mm}$.

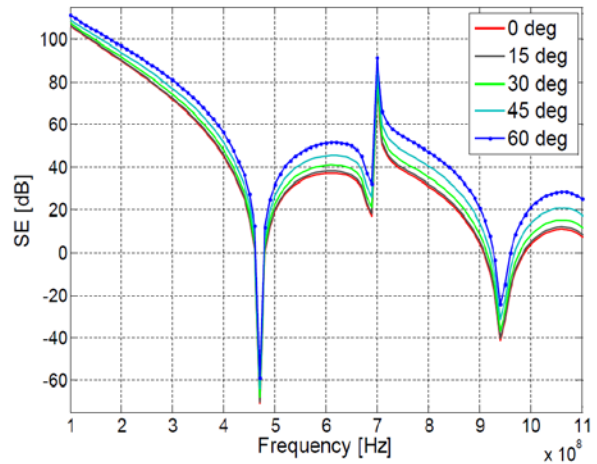


Fig. 8. Shielding effectiveness for various angles of incidence; $S = 100 \text{ mm}$, $L = 10 \text{ mm}$, $L_1 = L_2 = 3 \text{ mm}$, $e = 4 \text{ mm}$ of aluminum.

C. Impact of multiple apertures

Initially, the structure of shield has an aperture of $S = 100 \text{ mm}$ to serve as an input for ventilation and cabling. Even with the best composite material, an opening of this size will weaken the shielding effectiveness, because it will allow the passage of an important flow of electromagnetic fields.

Two cases are now considered. In the first one, the size of an aperture is taken as 20 mm , and the impact of an increase of the aperture number is evaluated (Fig. 9). It is obviously shown that it reduces the shielding effectiveness, because the larger the total area of the apertures is, the higher the fields penetrate inside the enclosure. Figure 10

shows concordance between FEM simulations and analytical results proposed by [10].

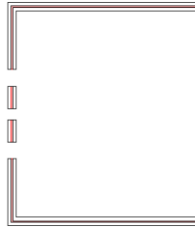


Fig. 9. Composite enclosure with three apertures.

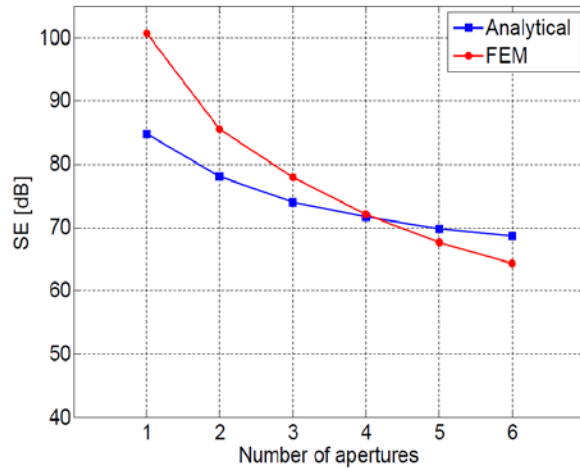


Fig. 10. Shielding effectiveness at 600 MHz vs. aperture number; $S = 20$ mm, $L = 4$ mm, $L_1 = L_2 = 1.5$ mm, $e = 1$ mm of aluminum, compared with analytical results.

For the second case, the initial 100 mm-opening is divided into several sub-apertures, so as to keep the same open area.

Figure 11 shows formally that this division of the opening increases the efficiency of shielding in a very striking way. Comparing a composite shielding with 6 sub-apertures to one with a single opening, the effectiveness increases with an average of 40 dB (this value is calculated over the frequency band of this study).

V. COMPARISON OF STRUCTURES

The comparison of the two structures, one with rods (Fig. 4) and the other with screen (Fig. 2), is now proposed considering the same mass and the same kind of conducting material, which is the carbon fiber ($\mu_r = 1$; $\epsilon_r = 4$; $\sigma = 21200$ S/m) (Fig. 12). In both structures, carbon fibers are incorporated into glass fibers.

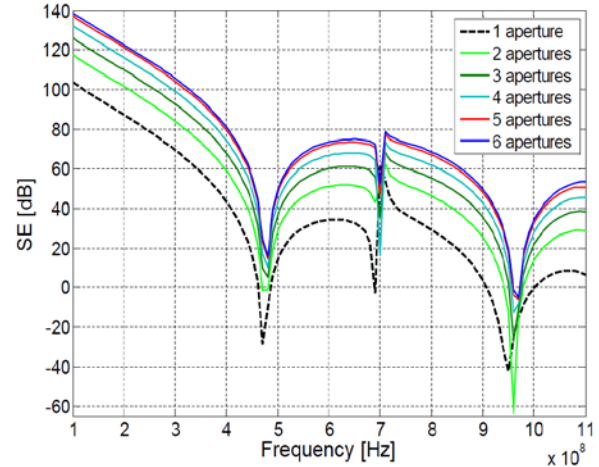


Fig. 11. Shielding effectiveness for various sub-aperture numbers with same open area.

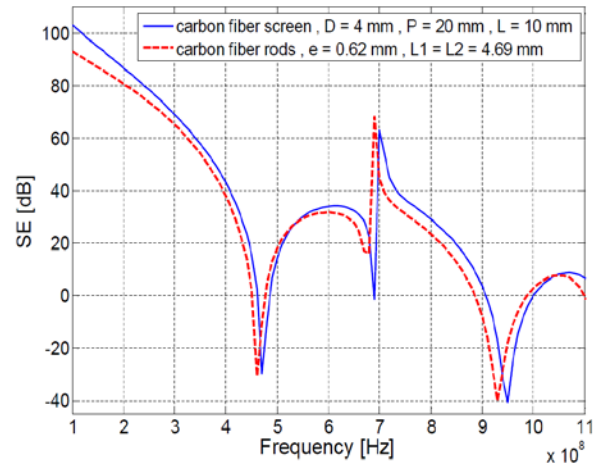


Fig. 12. Shielding effectiveness for composite walls with carbon-fiber rods and with carbon fiber screen.

Figure 12 illustrates that the shielding with screen composite walls is a little bit more effective than with rods. In fact, in the same conditions (equal masses for fiberglass and carbon fibers), over the entire frequency band, the screen structure displays an increase of effectiveness with an average about 2 dB compared to the rods. This can be explained by the fact that the structure with rods behaves like a screen structure since the distance between two rods is small compared to the wavelength. It is noted that the resonance inverted peaks are only slightly modified. However this result is highly dependent on the geometry, and particularly on the distance P .

VI. CONCLUSION

The shielding effectiveness of an enclosure with two different structures of composite walls was evaluated. Numerical results for the fiber rods show that the behavior of the wide band response is affected by their conductivity and their diameter. For the structure with a metal screen shield, comparison of the influence for different kinds of metals considering equal mass, has allowed equitably identifying the most effective metal in term of electromagnetic shielding. The influence of the incidence angle of the exciting wave has been illustrated. Moreover, higher SE was obtained using a composite enclosure with a subdivision of the aperture. Also, the comparison between fiber rod shield and fiber screen shield, with the same mass and with the same kind of conductive material, has shown that the second structure is less efficient than the first one.

The different simulations in this paper show that from the shielding point of view composite materials can be an excellent alternative to the conventional use of metal in enclosures. In addition, these materials have generally good mechanical and thermal characteristics. Ongoing works address practical 3D enclosures involving new conductive polymers.

REFERENCES

- [1] I. M. De Rosa, F. Sarasini, M. S. Sarto, Senior Member, IEEE, and A. Tamburrano, Member, IEEE, "EMC Impact of Advanced Carbon Fiber/Carbon Nanotube Reinforced Composites for Next-Generation Aerospace Applications," *IEEE Trans. Electromagn. Compat.*, vol. 50, no. 3, pp. 556-563, Aug. 2008.
- [2] A. Mehdipour, I. D. Rosca, A. Sebak, C. W. Trueman, S. V. Hoa, "Advanced Carbon-Fiber Composite Materials for RFID Tag Antenna Applications," *Applied Computational Electromagnetics Society (ACES) Journal*, vol. 25, no. 3, pp. 218-229, March 2010.
- [3] H-C. Chu and C.H. Chen, "Shielding and Reflection Properties of Periodic Fiber-Matrix Composite Structures", *IEEE Trans. on Electromagn. Compat.*, vol. 38, no. 1, pp. 1-6, 1996.
- [4] C. L. Holloway, M. S. Sarto, and M. Johansson, "Analyzing Carbon-Fiber Composite Materials with Equivalent-Layer Models", *IEEE Trans. on Electromagn. Compat.*, vol. 47, no. 4, pp. 833-844, 2005.
- [5] I. M. De Rosa, R. Mancinelli, F. Sarasini, M. S. Sarto, and A. Tamburrano, "Electromagnetic Design and Realization of Innovative Fiber-Reinforced Broad-Band Absorbing Screens", *IEEE Trans. on Electromagn. Compat.*, vol. 51, no. 3, pp. 700-707, 2009.
- [6] M. Koledintseva, J. Drewniak, Y. Zhang, J. Lenn, and M. Thoms, "Modeling of Ferrite-Based Materials for Shielding Enclosures", *Journal of Magnetism and Magnetic Materials*, 321, pp. 730-733, 2009.
- [7] Z. B. Zhao, X. Cui, L. Li, and B. Zhang, "Analysis of the Shielding Effectiveness of Rectangular Enclosure of Metal Structures with Apertures Above Ground Plane", *IEEE Trans. on Magn.*, vol. 41, no. 5, pp. 1892-1895, 2005.
- [8] M. A. Khorrami, P. Dehkoda, R. M. Mazandaran, and S. H. H. Sadeghi, "Fast Shielding Effectiveness Calculation of Metallic Enclosures with Apertures using a Multiresolution Method of Moments Technique", *IEEE Trans. on Electromagn. Compat.*, vol. 52, no. 1, pp. 230-235, 2010.
- [9] R. Araneo and G. Lovat, "Analysis of the Shielding Effectiveness of Metallic Enclosures Excited by Internal Sources Through an Efficient Method-of-Moment Approach," *Applied Computational Electromagnetics Society (ACES) Journal*, vol. 25, pp. 600-611, Jul. 2010.
- [10] H. H. Park and H. J. Eom, "Electromagnetic Penetration into 2-D Multiple Slotted Rectangular Cavity: TM-Wave," *IEEE Trans. Antennas Propagat.*, vol. 48, no. 2, pp. 331-333, Feb 2000.
- [11] K. P. Ma, M. Li, J. L. Drewniak, T. H. Hubing, and T. P. Van Doren, "Comparison of FDTD Algorithms for Subcellular Modeling of Slots in Shielding Enclosures," *IEEE Trans. Electromagn. Compat.*, vol. 39, no. 2, pp. 147-155, May 1997.
- [12] R. L. Macpherson and N. J. Ryan, "Reducing Electromagnetic Coupling in Shielded Enclosures using a Genetic Algorithm - Finite-Difference Time-Domain Solver", *Applied Computational Electromagnetics Society (ACES) Journal*, vol. 17, no. 3, pp. 218-224, Nov. 2002.
- [13] C. Jiao, L. Li, X. Cui, and H. Li, "Subcell FDTD Analysis of Shielding Effectiveness of a Thin-Walled Enclosure with an Aperture," *IEEE Trans. Magn.*, vol. 42, no. 4, pp. 1075-1078, Apr. 2006.
- [14] J. Chen and A. Zhang, "A Subgridding Scheme Based on the FDTD Method and HIE-FDTD Method," *Applied Computational Electromagnetics Society (ACES) Journal*, vol. 26, no. 1, pp. 1-7, Jan. 2011.
- [15] X. Li, J.-H. Yu, Q.-D. Wang, and Y.-M. Li, "Extension of the 2-D CP-FDTD Thin Slot Algorithm to 3-D for Shielding Analysis," *Applied*

Computational Electromagnetics Society (ACES) Journal, vol. 24, no. 1, pp. 16–20, Feb. 2009.

- [16] W. P. Carpes, Jr., G. S. Ferreira, A. Raizer, L. Pichon, and A. Razek, "TLM and FEM Methods Applied in the Analysis of Electromagnetic Coupling", *IEEE Trans. on Magn.*, vol. 36., no. 4, pp. 982-985, 2000.
- [17] B.-L. Nie, P.-A. Du, Y.-T. Yu, and Z. Shi, "Study of the Shielding Properties of Enclosures with Apertures at Higher Frequencies using the Transmission-Line Modeling Method", *IEEE Trans. on Electromagn. Compat.*, vol. 53, no. 1, pp. 73-81, 2011.
- [18] B. W. Kim, Y. C. Chung, and T. W. Kang, "Analysis of Electromagnetic Penetration through Apertures of Shielded Enclosure using Finite Element Method," in *14th Annu. Rev. Progress Appl. Computat. Electromagn.*, vol. II, pp. 795-798, Mar. 1998.
- [19] S. Celozzi and M. S. Sarto, "Equivalent Source Method for the Evaluation of the Electromagnetic Field Penetration inside Enclosures", *IEEE Trans. on Magn.*, vol. 32, no. 3, pp. 1497-1500, 1996.
- [20] X. Ojeda and L. Pichon, "Combining the Finite Element Method and Pade Approximation for Scattering Analysis Application to Radiated Electromagnetic Compatibility Problems," *Journal of Electromagnetic Waves and Applications*, vol. 19, no. 10, pp. 1375-1390, 2005.

Wassim Abdelli was born in Tunisia. He received the B.S. and Research M.S. degrees in Electronic Systems Engineering from the University Tunis El Manar, Tunisia, in 2006 and 2008, respectively. He is currently in PhD studies with the Laboratoire de Génie Electrique de Paris and the Laboratoire de Circuits et Systèmes Electroniques à Hautes Fréquences in the Faculté des Sciences of Tunis, where he is an assistant lecturer.



His current research interests include electromagnetic compatibility shielding, characterization of fiber reinforced composites, absorbing materials, advanced composite materials for electromagnetic applications.



Xavier Mininger was born in Strasbourg, France, in 1978. He received the B.S. and M.S. degrees in Electrical Engineering from Paris Sud 11 University. He received his Ph.D. degree in Electrical Engineering from ENS de Cachan (SATIE) in 2005. In 2006, he got a position of assistant professor at Université Paris-Sud and joined the Laboratoire de Génie Electrique de Paris (LGEP). His main research topics consist in the numerical modeling of multiphysic problems, involving models of active materials. He also studies vibrations and acoustic emission of electrical machines.



Lionel Pichon is an engineer from Ecole Supérieure d'Ingénieurs en Electronique et Electrotechnique (ESIEE) in 1984. In 1985, he joined the Laboratoire de Génie Electrique de Paris (LGEP) where he earned a Ph.D. in Electrical Engineering in 1989. He got a position at the CNRS (Centre National de la Recherche Scientifique) in 1989. He is now Directeur de Recherche at the CNRS (Senior Scientist). Since 2002, he is one of the animators of the Groupement de Recherche CNRS, known as GDR Ondes, where is involved a large network of laboratories and researchers related to the modeling of wave propagation from mathematical theory to numerical solutions for particular applications.

Since 2005, he is the head of the team ICHAMS of the LGEP dedicated to the modeling of interactions between electromagnetic fields and complex structures. His research interests include computational electromagnetics for wave propagation and scattering, electromagnetic compatibility and non-destructive testing. He is the author or co-author of more than 70 papers in international journals.



Hichem Trabelsi was born in Tunisia in 1962. He received the Ph.D. degree in Electronics from the Université Pierre et Marie Curie, Paris VI, France, in 1991. He joined the department of Physics at the Faculté des Sciences de Tunis, in 1992, where he is working on microwave active and passive circuits and electromagnetic theory for solving field problems in microwave domain.

He is currently co-director of the Laboratoire de Circuits et Systèmes Electroniques à Hautes Fréquences and Full Professor in the Ecole Supérieure de Technologie et d'Informatique.

2012 INSTITUTIONAL MEMBERS

DTIC-OCP LIBRARY
8725 John J. Kingman Rd, Ste 0944
Fort Belvoir, VA 22060-6218

AUSTRALIAN DEFENCE LIBRARY
Northcott Drive
Canberra, A.C.T. 2600 Australia

BEIJING BOOK CO, INC
701 E Linden Avenue
Linden, NJ 07036-2495

DARTMOUTH COLLEGE
6025 Baker/Berry Library
Hanover, NH 03755-3560

DSTO EDINBURGH
AU/33851-AP, PO Box 830470
Birmingham, AL 35283

SIMEON J. EARL – BAE SYSTEMS
W432A, Warton Aerodome
Preston, Lancs., UK PR4 1AX

ENGINEERING INFORMATION, INC
PO Box 543
Amsterdam, Netherlands 1000 Am

ETSE TELECOMUNICACION
Biblioteca, Campus Lagoas
Vigo, 36200 Spain

GA INSTITUTE OF TECHNOLOGY
EBS-Lib Mail code 0900
74 Cherry Street
Atlanta, GA 30332

TIMOTHY HOLZHEIMER
Raytheon
PO Box 1044
Rockwall, TX 75087

HRL LABS, RESEARCH LIBRARY
3011 Malibu Canyon
Malibu, CA 90265

IEE INSPEC
Michael Faraday House
6 Hills Way
Stevenage, Herts UK SG1 2AY

INSTITUTE FOR SCIENTIFIC INFO.
Publication Processing Dept.
3501 Market St.
Philadelphia, PA 19104-3302

LIBRARY – DRDC OTTAWA
3701 Carling Avenue
Ottawa, Ontario, Canada K1A OZ4

LIBRARY of CONGRESS
Reg. Of Copyrights
Attn: 407 Deposits
Washington DC, 20559

LINDA HALL LIBRARY
5109 Cherry Street
Kansas City, MO 64110-2498

MISSOURI S&T
400 W 14th Street
Rolla, MO 56409

MIT LINCOLN LABORATORY
Periodicals Library
244 Wood Street
Lexington, MA 02420

NATIONAL CHI NAN UNIVERSITY
Lily Journal & Book Co, Ltd
20920 Glenbrook Drive
Walnut, CA 91789-3809

JOHN NORGARD
UCCS
20340 Pine Shadow Drive
Colorado Springs, CO 80908

OSAMA MOHAMMED
Florida International University
10555 W Flagler Street
Miami, FL 33174

NAVAL POSTGRADUATE SCHOOL
Attn:J. Rozdal/411 Dyer Rd./ Rm 111
Monterey, CA 93943-5101

NDL KAGAKU
C/O KWE-ACCESS
PO Box 300613 (JFK A/P)
Jamaica, NY 11430-0613

OVIEDO LIBRARY
PO BOX 830679
Birmingham, AL 35283

DAVID PAULSEN
E3Compliance
1523 North Joe Wilson Road
Cedr Hill, TX 75104-1437

PENN STATE UNIVERSITY
126 Paterno Library
University Park, PA 16802-1808

DAVID J. PINION
1122 E Pike Street #1217
SEATTLE, WA 98122

KATHERINE SIAKAVARA
Gymnasiou 8
Thessaloniki, Greece 55236

SWETS INFORMATION SERVICES
160 Ninth Avenue, Suite A
Runnemedede, NJ 08078

YUTAKA TANGE
Maizuru Natl College of Technology
234 Shiroya
Maizuru, Kyoto, Japan 625-8511

TIB & UNIV. BIB. HANNOVER
DE/5100/G1/0001
Welfengarten 1B
Hannover, Germany 30167

UEKAE
PO Box 830470
Birmingham, AL 35283

UNIV OF CENTRAL FLORIDA
4000 Central Florida Boulevard
Orlando, FL 32816-8005

UNIVERSITY OF COLORADO
1720 Pleasant Street, 184 UCB
Boulder, CO 80309-0184

UNIVERSITY OF KANSAS –
WATSON
1425 Jayhawk Blvd 210S
Lawrence, KS 66045-7594

UNIVERSITY OF MISSISSIPPI
JD Williams Library
University, MS 38677-1848

UNIVERSITY LIBRARY/HKUST
Clear Water Bay Road
Kowloon, Honk Kong

CHUAN CHENG WANG
8F, No. 31, Lane 546
MingCheng 2nd Road, Zuoying Dist
Kaoshiung City, Taiwan 813

THOMAS WEILAND
TU Darmstadt
Schlossgartenstrasse 8
Darmstadt, Hessen, Germany 64289

STEVEN WEISS
US Army Research Lab
2800 Powder Mill Road
Adelphi, MD 20783

YOSHIHIDE YAMADA
NATIONAL DEFENSE ACADEMY
1-10-20 Hashirimizu
Yokosuka, Kanagawa,
Japan 239-8686

INFORMATION FOR AUTHORS

PUBLICATION CRITERIA

Each paper is required to manifest some relation to applied computational electromagnetics. **Papers may address general issues in applied computational electromagnetics, or they may focus on specific applications, techniques, codes, or computational issues.** While the following list is not exhaustive, each paper will generally relate to at least one of these areas:

- 1. Code validation.** This is done using internal checks or experimental, analytical or other computational data. Measured data of potential utility to code validation efforts will also be considered for publication.
- 2. Code performance analysis.** This usually involves identification of numerical accuracy or other limitations, solution convergence, numerical and physical modeling error, and parameter tradeoffs. However, it is also permissible to address issues such as ease-of-use, set-up time, run time, special outputs, or other special features.
- 3. Computational studies of basic physics.** This involves using a code, algorithm, or computational technique to simulate reality in such a way that better, or new physical insight or understanding, is achieved.
- 4. New computational techniques** or new applications for existing computational techniques or codes.
- 5. “Tricks of the trade”** in selecting and applying codes and techniques.
- 6. New codes, algorithms, code enhancement, and code fixes.** This category is self-explanatory, but includes significant changes to existing codes, such as applicability extensions, algorithm optimization, problem correction, limitation removal, or other performance improvement. **Note: Code (or algorithm) capability descriptions are not acceptable, unless they contain sufficient technical material to justify consideration.**
- 7. Code input/output issues.** This normally involves innovations in input (such as input geometry standardization, automatic mesh generation, or computer-aided design) or in output (whether it be tabular, graphical, statistical, Fourier-transformed, or otherwise signal-processed). Material dealing with input/output database management, output interpretation, or other input/output issues will also be considered for publication.
- 8. Computer hardware issues.** This is the category for analysis of hardware capabilities and limitations of various types of electromagnetics computational requirements. Vector and parallel computational techniques and implementation are of particular interest. Applications of interest include, but are not limited to,

antennas (and their electromagnetic environments), networks, static fields, radar cross section, inverse scattering, shielding, radiation hazards, biological effects, biomedical applications, electromagnetic pulse (EMP), electromagnetic interference (EMI), electromagnetic compatibility (EMC), power transmission, charge transport, dielectric, magnetic and nonlinear materials, microwave components, MEMS, RFID, and MMIC technologies, remote sensing and geometrical and physical optics, radar and communications systems, sensors, fiber optics, plasmas, particle accelerators, generators and motors, electromagnetic wave propagation, non-destructive evaluation, eddy currents, and inverse scattering.

Techniques of interest include but not limited to frequency-domain and time-domain techniques, integral equation and differential equation techniques, diffraction theories, physical and geometrical optics, method of moments, finite differences and finite element techniques, transmission line method, modal expansions, perturbation methods, and hybrid methods.

Where possible and appropriate, authors are required to provide statements of quantitative accuracy for measured and/or computed data. This issue is discussed in “Accuracy & Publication: Requiring, quantitative accuracy statements to accompany data,” by E. K. Miller, *ACES Newsletter*, Vol. 9, No. 3, pp. 23-29, 1994, ISBN 1056-9170.

SUBMITTAL PROCEDURE

All submissions should be uploaded to ACES server through ACES web site (<http://aces.ee.olemiss.edu>) by using the upload button, journal section. Only pdf files are accepted for submission. The file size should not be larger than 5MB, otherwise permission from the Editor-in-Chief should be obtained first. Automated acknowledgment of the electronic submission, after the upload process is successfully completed, will be sent to the corresponding author only. It is the responsibility of the corresponding author to keep the remaining authors, if applicable, informed. Email submission is not accepted and will not be processed.

EDITORIAL REVIEW

In order to ensure an appropriate level of quality control, papers are peer reviewed. They are reviewed both for technical correctness and for adherence to the listed guidelines regarding information content and format.

PAPER FORMAT

Only camera-ready electronic files are accepted for publication. The term **“camera-ready”** means that the material is neat, legible, reproducible, and in accordance with the final version format listed below.

The following requirements are in effect for the final version of an ACES Journal paper:

1. The paper title should not be placed on a separate page.

The title, author(s), abstract, and (space permitting) beginning of the paper itself should all be on the first page. The title, author(s), and author affiliations should be centered (center-justified) on the first page. The title should be of font size 16 and bolded, the author names should be of font size 12 and bolded, and the author affiliation should be of font size 12 (regular font, neither italic nor bolded).

2. An abstract is required. The abstract should be a brief summary of the work described in the paper. It should state the computer codes, computational techniques, and applications discussed in the paper (as applicable) and should otherwise be usable by technical abstracting and indexing services. The word "Abstract" has to be placed at the left margin of the paper, and should be bolded and italic. It also should be followed by a hyphen (–) with the main text of the abstract starting on the same line.
3. All section titles have to be centered and all the title letters should be written in caps. The section titles need to be numbered using roman numbering (I. II.)
4. Either British English or American English spellings may be used, provided that each word is spelled consistently throughout the paper.
5. Internal consistency of references format should be maintained. As a guideline for authors, we recommend that references be given using numerical numbering in the body of the paper (with numerical listing of all references at the end of the paper). The first letter of the authors' first name should be listed followed by a period, which in turn, followed by the authors' complete last name. Use a coma (,) to separate between the authors' names. Titles of papers or articles should be in quotation marks (" "), followed by the title of journal, which should be in italic font. The journal volume (vol.), issue number (no.), page numbering (pp.), month and year of publication should come after the journal title in the sequence listed here.
6. Internal consistency shall also be maintained for other elements of style, such as equation numbering. Equation numbers should be placed in parentheses at the right column margin. All symbols in any equation have to be defined before the equation appears or right immediately following the equation.
7. The use of SI units is strongly encouraged. English units may be used as secondary units (in parentheses).
8. Figures and tables should be formatted appropriately (centered within the column, side-by-side, etc.) on the page such that the presented data appears close to and after it is being referenced in the text. When including figures and tables, all care should be taken so that they will appear appropriately when printed in black and white. For better visibility of paper on computer screen, it is good to make color figures with different line styles for figures with multiple curves. Colors should also be tested to insure their ability to be distinguished after

black and white printing. Avoid the use of large symbols with curves in a figure. It is always better to use different line styles such as solid, dotted, dashed, etc.

9. A figure caption should be located directly beneath the corresponding figure, and should be fully justified.
10. The intent and meaning of all text must be clear. For authors who are not masters of the English language, the ACES Editorial Staff will provide assistance with grammar (subject to clarity of intent and meaning). However, this may delay the scheduled publication date.
11. Unused space should be minimized. Sections and subsections should not normally begin on a new page.

ACES reserves the right to edit any uploaded material, however, this is not generally done. It is the author(s) responsibility to provide acceptable camera-ready files in pdf and MSWord formats. Incompatible or incomplete files will not be processed for publication, and authors will be requested to re-upload a revised acceptable version.

COPYRIGHTS AND RELEASES

Each primary author must execute the online copyright form and obtain a release from his/her organization vesting the copyright with ACES. Both the author(s) and affiliated organization(s) are allowed to use the copyrighted material freely for their own private purposes.

Permission is granted to quote short passages and reproduce figures and tables from and ACES Journal issue provided the source is cited. Copies of ACES Journal articles may be made in accordance with usage permitted by Sections 107 or 108 of the U.S. Copyright Law. This consent does not extend to other kinds of copying, such as for general distribution, for advertising or promotional purposes, for creating new collective works, or for resale. The reproduction of multiple copies and the use of articles or extracts for commercial purposes require the consent of the author and specific permission from ACES. Institutional members are allowed to copy any ACES Journal issue for their internal distribution only.

PUBLICATION CHARGES

All authors are allowed for 8 printed pages per paper without charge. Mandatory page charges of \$75 a page apply to all pages in excess of 8 printed pages. Authors are entitled to one, free of charge, copy of the printed journal issue in which their paper was published. Additional reprints are available for \$ 50. Requests for additional re-prints should be submitted to the managing editor or ACES Secretary.

Corresponding author is required to complete the online form for the over page charge payment right after the initial acceptance of the paper is conveyed to the corresponding author by email.

ACES Journal is abstracted in INSPEC, in Engineering Index, DTIC, Science Citation Index Expanded, the Research Alert, and to Current Contents/Engineering, Computing & Technology.